Statistical Mechanics of Superparamagnetic Colloidal Dispersions Under Magnetic Fields

by

Jordi Andreu Segura

PhD Thesis in Materials Science

Departament de Física
Universitat Autònoma de Barcelona

14th January 2013

under the supervision of:

Dr. Jordi Faraudo Gener
Departament de Teoria i Simulació de Materials
Institut de Ciència de Materials de Barcelona

Dr. Juan Camacho Castro
Departament de Física, Grup de Física Estadística
Universitat Autònoma de Barcelona

Chapter 5

Articles

Compilation of articles accepted by the PhD commission

5.1 Article 1

"Aggregation of superparamagnetic colloids in magnetic elds: the quest for the equilibrium state."
Jordi S. Andreu, Juan Camacho and Jordi Faraudo
Soft Matter **7**, 2336 (2011)

Soft Matter

Dynamic Article Links

Cite this: *Soft Matter*, 2011, **7**, 2336

www.rsc.org/softmatter

COMMUNICATION

Aggregation of superparamagnetic colloids in magnetic fields: the quest for the equilibrium state†

Jordi S. Andreu,[ab] Juan Camacho[b] and Jordi Faraudo*[a]

Received 6th December 2010, Accepted 20th January 2011
DOI: 10.1039/c0sm01424a

Previous experimental and simulation studies of superparamagnetic colloids in a strong external field have systematically shown a nonequilibrium aggregation process in which chains of particles steadily grow in the direction of the applied external field with the average length increasing as a power law over time. Here we show, by employing Langevin dynamics simulations, the existence of a different behavior under the effects of an external magnetic field: after a transient period of chain formation, the system attains an equilibrium state. Furthermore, a thermodynamic self-assembly theory supports the simulation results and it also predicts that the average chain length in the equilibrium state depends only on a dimensionless parameter combining the volume fraction of colloids ϕ_0 and the magnetic coupling parameter Γ. The conditions under which this new behavior can be observed are discussed here.

Colloidal aggregation is a subject of active research for both practical (*e.g.* stability of many industrial products) and fundamental reasons (as a test field for statistical–mechanical theories, for example). Our interest is in the new physics arising in the aggregation behavior of superparamagnetic colloids. These systems are a successful example of implementation of a new behavior typical of the nanoscale (superparamagnetism) and these new materials with many exciting practical applications, ranging from environmental waste capture[1] to biomedicine.[2] Superparamagnetic colloids are composite particulate materials made by embedding nanocrystals with superparamagnetic response in a non-magnetic matrix (such as polystyrene, nanoporous silica or others).[3] The resulting colloids show a very large magnetic dipole in presence of external fields but no coercitivity nor remanence at the working temperature.

Interestingly, dispersions of superparamagnetic colloids require the application of an external field in order to induce structuration (aggregation or chain formation) as the colloids have no magnetic dipole in the absence of external fields. For example, using superpositions of ac magnetic fields in different directions is possible to induce nanostructures made of aggregates of particles such as gels[4] or membranes.[5] In the simplest case of a constant external field, superparamagnetic colloids acquire large dipoles and arrange (head-to-tail) forming linear aggregates (chains). These chains are aligned with the external magnetic field both in the case of homogeneous[6–8] and inhomogeneous external fields.[9–11] After removal of the external magnetic field, it is observed that, the chains rapidly disaggregate and the initial dispersion (no aggregation) is recovered.[6–8,10]

In these systems, theoretical investigations have focused on the study of the kinetics of chain growth under an external uniform and constant field. In particular, simulations predict a power-law increase of the chain length with time,[12] a behavior compatible with experimental observations.[6,7,12] Our objective in this communication is to show a different aggregation behavior for this case, which has not previously been reported in either experimental or simulation studies. We will present evidences from computer simulations and thermodynamic self-assembly theory supporting the existence of an equilibrium state under certain realistic combinations of size and saturation magnetization of the colloids. In this state, the average length of the chains attains an equilibrium value which depends on the volume fraction of colloids, their size and their saturation magnetization. This equilibrium state, obtained for superparamagnetic colloids under an external field, has some formal similarities (but also important differences) with the equilibrium state observed for dipolar particles in the absence of external fields. At this point, we should stress that understanding the aggregation process of superparamagnetic colloids under external fields is not only relevant from a fundamental perspective, but it also has practical importance. A paradigmatic example is the *fast* magnetophoretic separation process employed in biotechnological applications,[10,13,14] which requires the formation of chains of superparamagnetic colloids.

As in previous simulations[11,12] we would like to consider here the minimal model describing superparamagnetic colloids: spheres of diameter d with a magnetic dipole diffusing in a fluid with viscosity η. For the sake of simplicity, we assume here (as in ref. 12) that the magnetization of the colloids has reached saturation. This means that each colloid has a constant dipole m_s (corresponding to saturation magnetization) parallel to the external applied field. This situation is also commonly found in experiments (typically at applied fields > 0.1 T, see ref. 10,12–14). In this situation, the magnetic effects can be described by the magnetic coupling parameter Γ, defined as the ratio between the maximum of the magnetic dipole–dipole attraction and the thermal energy:

[a]*Institut de Ciència de Materials de Barcelona (ICMAB-CSIC), Campus de la UAB, E-08193 Bellaterra, Spain. E-mail: jfaraudo@icmab.es*
[b]*Dept. de Física, Universitat Autònoma de Barcelona, Campus UAB, E-08193 Bellaterra, Spain*

† Electronic Supplementary Information (ESI) available: Detailed description of simulation procedures, snapshots and movies. See DOI: 10.1039/c0sm01424a/

$$\Gamma = \frac{\mu_0 m_s^2}{2\pi d^3 k_B T}. \quad (1)$$

Hence, our model is characterized by two dimensionless parameters, the coupling constant Γ and the volume fraction of colloids ϕ_0.

The three-dimensional simulations reported here are based on a numerical integration of the Langevin stochastic equation of motion for each colloid, as in previous work.[11,12] In this framework, the force acting on each particle is given by the sum of a particle–particle interaction force, the viscous drag acting against each colloid and a stochastic force corresponding to the thermal noise. The particle–particle interaction potential is given by the sum of the magnetic dipole–dipole interaction and a steric, short range strong repulsion, which prevents overlap between particles. We have assumed that water is the solvent and we have neglected the effect of sedimentation by considering that our colloids have a density of 1 g cm^{-3} (which is similar to that of many commercial superparamagnetic particles since it helps to avoid storage problems). All simulations were performed using the Langevin dynamics option as implemented in the 21 May 2008 version of the LAMMPS simulation software.[15] The equation of motion was solved using a time step of 1 ns. Due to the long-range behavior of magnetic particle–particle interactions, our accurate simulations were extremely time consuming and difficult to parallelize. Each second of simulation time requires (depending on the specific simulation) between 300–1100 h of computer time employing 16 Itanium Montvale processors. All technical details and movies illustrating the simulations are available in the electronic supporting information (ESI, †). In all simulations, we had $N_0 = 8000$ colloids in the simulation box, and different concentrations were obtained by employing different system volumes V. The diameter of the colloids was fixed to $d = 100$ nm, a value typical for small superparamagetic colloids (although this value is not essential in the sense that simulations with the same value of Γ are expected to give equivalent results). We have considered two different simulation sets. In the first set (Fig. 1 and 2) we considered a volume fraction of colloids $\phi_0 = 5.23 \times 10^{-4}$ and different values of Γ. In the second simulation set (Fig. 3) we have considered $\Gamma = 10$ and volume fractions $\phi_0 = 5.23 \times 10^{-4}$, 1.05×10^{-3}, 2.62×10^{-3} and 5.23×10^{-3} (which corresponds to concentrations between $\sim$0.5 g l^{-1} and $\sim$5 g l^{-1}, typical of experiments).

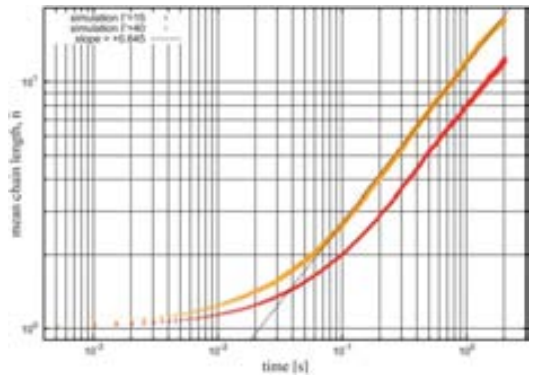

Fig. 1 Time evolution of the average length of chains in simulations with concentration $\sim$ 0.5 g l^{-1} ($\phi_0 = 5.23 \times 10^{-4}$) and magnetic coupling constants $\Gamma = 15$ and 40. The dashed line is a power-law fit $\bar{n} \sim t^z$ to the case $\Gamma = 40$.

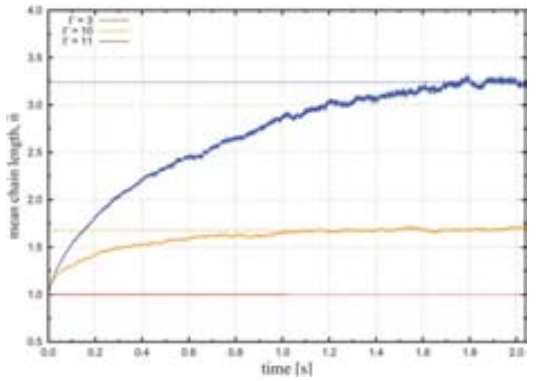

Fig. 2 Time evolution of the average length of chains in simulations with 0.5 g l^{-1} concentration ($\phi_0 = 5.23 \times 10^{-4}$) and different magnetic coupling constants ($\Gamma = 3$, 10 and 11). Dashed lines indicate the mean chain length value at equilibrium.

As a check for the validity of our simulations, we looked for the typical power-law kinetic behavior observed in previous works, which consider large values of Γ (for example in the simulations of ref. 12 Γ is between 100 and 3000). We have found (see Fig. 1) that from Γ as small as $\Gamma = 15$ (and $\phi_0 = 5.23 \times 10^{-4}$) the mean number of colloids per chain follows $\bar{n} \sim t^z$ with kinetic exponent $z \approx 0.63$. Simulations with $\Gamma = 40$ and $\phi_0 = 5.23 \times 10^{-4}$ give a slightly larger kinetic exponent, $z \simeq 0.645$. Our findings are consistent with other previous work,[6,7,12] which typically report kinetic exponents in the range 0.6–0.7.

At the same volume fraction of colloids ($\phi_0 = 5.23 \times 10^{-4}$), lower values of Γ produce results with a qualitatively different behavior (see Fig. 2). After a transient process of chain growth, we reach a time independent value of $\bar{n}$ which strongly depends on Γ. Also, the other physical quantities characterizing the system (such as the potential energy) reach a saturation value (see ESI, †). At $\phi_0 = 5.23 \times 10^{-4}$, we found $\bar{n} \sim 3.2$ for $\Gamma = 11$ and $\bar{n} \sim 1.7$ for $\Gamma = 10$ (see Fig. 2). For $\Gamma = 3$ we found no significant aggregation. For a given value of Γ, the length of the chains strongly depends on ϕ_0 (see Fig. 3). The

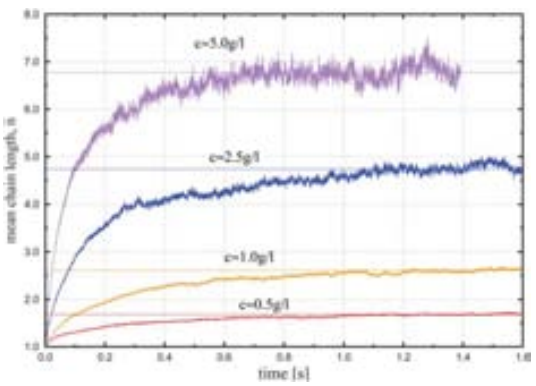

Fig. 3 Time evolution of the average chain length obtained in simulations with $\Gamma = 10$ and four different concentrations ($c \approx 0.5$, 1, 2.5 and 5 g l^{-1}). Dashed lines indicate the mean chain length value at equilibrium.

equilibrium value for $\bar{n}$ increases from $\simeq 1.7$ at $\phi_0 = 5.23 \times 10^{-4}$ to $\simeq 6.8$ at $\phi_0 = 5.23 \times 10^{-3}$ (see Fig. 3).

Fig. 4 displays the distribution of chain length in the equilibrium state (where N_s is the number of chains of size s and $n_s = N_s/V$). The main figure shows that the fraction of chains of length s, $n_s/\sum_s n_s$ decays exponentially for large s. The inset shows that, after an appropriate normalization, the fraction of chains of length s for different concentrations approximately collapses into a single curve.

The obtained simulation results can be understood by considering a simple thermodynamic calculation based on the self-assembly theory of magnetic particles.[16] This theory was originally developed to describe the formation of chains in dispersions of particles with permanent dipolar moment in absence of external field. Here, we modify this theory to consider the particular case of super-paramagnetic colloids in a strong external field. Let us start by considering that the magnetic energy of a chain made of s dipoles is given by $\approx -(s-1)\varepsilon_m$, *i.e.* the energy arises from $s-1$ bonds each one with magnetic energy $-\varepsilon_m$. Although this approximation may seems rather crude, the resulting formalism captures the main features of our simulation results, as we will see. The chemical potential μ_s of a colloid which forms part of a chain of s colloids is given by the ideal (entropic) term plus the interaction energy term:[16]

$$\mu_s = \mu^0 + \frac{1}{s}\left[k_B T \ln\frac{\phi_s}{s} - (s-1)\varepsilon_m\right]. \quad (2)$$

where ϕ_s is the volume fraction of chains containing s colloids, and it is related to the number of chains per unit volume through $n_s \propto \phi_s/s$. In the equilibrium state, the chemical potential μ_1 of a colloid in dispersion in a non-aggregated state is equal to the chemical potential of a colloid in any of the possible chains of length s, so we have $\mu_1 = \mu_s$. Using eqn(2) we obtain ($\beta = 1/k_B T$):

$$\phi_s = s[\phi_1 e^{\beta\varepsilon_m}]^s\, e^{-\beta\varepsilon_m}, \quad (3)$$

with the constraint:

$$\phi_0 = \sum_{s=1}^{\infty} \phi_s. \quad (4)$$

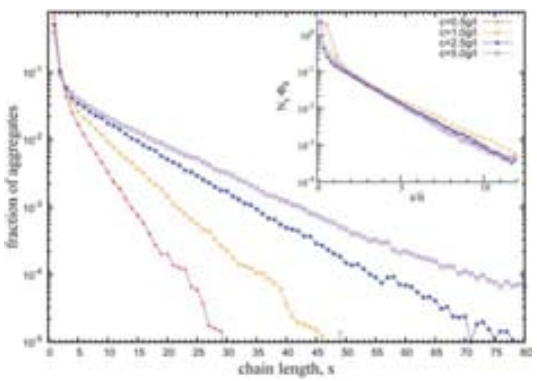

Fig. 4 Fraction of chains of length s, $n_s/\sum_s n_s$ in the equilibrium state from simulations with $\Gamma = 10$ and four different concentrations ($c = 0.5$, 1, 2.5 and 5 g l^{-1}). Inset: Rescaled distribution of chains, $N_s\phi_0$ as a function of $s/\bar{n}$.

Using eqn(3) in (4) we obtain the following relation between the (total) volume fraction of colloids ϕ_0 and the volume fraction of non-aggregated colloids ϕ_1:

$$\phi_0 e^{\beta\varepsilon_m} = \frac{\phi_1 e^{\beta\varepsilon_m}}{(1-\phi_1 e^{\beta\varepsilon_m})^2}. \quad (5)$$

Note also that we assume $\phi_1 e^{\beta\varepsilon_m} < 1$ in order to ensure convergence of eqn(4)–(5). Eqn(5) can be easily solved to obtain $\phi_1 e^{\beta\varepsilon_m}$ in terms of the parameter N^* defined as:

$$N^* = \sqrt{\phi_0 e^{\beta\varepsilon_m}}. \quad (6)$$

For small $N^* \ll 1$ (very diluted system or low magnetic coupling parameter) eqn(5) supplies no significant aggregation, $\phi_1 \approx \phi_0$. On the opposite case, $N^* \gg 1$, eqn(5) gives $\phi_1 \approx e^{-\beta\varepsilon_m}(1 - 1/N^*)$. In this approximation, the number of chains of length s per unit volume is given by:

$$n_s \propto \phi_s/s \simeq (1 - 1/N^*)^s \approx e^{-s/N^*}. \quad (7)$$

The average length of chains is thus $\bar{n} \approx N^*$. Also, note that an exponential decay is observed in our simulation results for large s (see Fig. 4), thereby supporting the plausibility of the simplifications introduced in the thermodynamic calculation. It is also interesting to note that such an exponential distribution has also been obtained in the case of aggregation of patchy particles.[17]

In order to make more explicit predictions, we need to relate ε_m (and hence N^*) with known magnetic properties of the colloids. To this end, consider a chain of two colloids in contact, each one with dipole m_s (corresponding to saturation magnetization) parallel to the external applied field. Their magnetic interaction energy is given by $U_m = -k_B T\Gamma(1 - (3/2)\sin^2\theta)$ where θ is the angle between the magnetic field and the line joining the centers of the two colloids. This interaction is attractive for $|\theta| < \theta_0 = 54.7°$, being maximum at $\theta = 0$ ($\beta U_m(0) = -\Gamma$). The thermal average of this interaction over all orientations corresponding to the bonding between two colloids is given by $\beta\langle U_m(\theta)\rangle = -\Gamma\left[1 - \frac{3}{2}\langle\sin^2\theta\rangle\right]$ where:

$$\sin^2\theta = \frac{\int_{\theta=-\theta_0}^{\theta=\theta_0} d(\cos\theta)\sin^2\theta e^{-\beta U_m(\theta)}}{\int_{\theta=-\theta_0}^{\theta=\theta_0} d(\cos\theta) e^{-\beta U_m(\theta)}} = \frac{2}{3\Gamma} + \mathcal{O}\left(\frac{1}{\Gamma^2}\right). \quad (8)$$

Hence,we have $\beta\langle U_m(\theta)\rangle \simeq 1 - \Gamma$. The last equality in eqn(8) comes from the stationary phase approximation, which in this case is extremely good. For example, for $\Gamma = 10$ we obtain $\beta\langle U_m\rangle = -8.96 \simeq -9$ from a numerical evaluation of eqn(8). Even for smaller values of Γ the approximation is quite good, for example for $\Gamma = 3$ we have $\beta\langle U_m\rangle = -2.071 \approx -2$. Therefore, as an estimation for ε_m we take this thermal averaged dipole–dipole interaction, which gives $\beta\varepsilon_m \approx \Gamma - 1$ and then we obtain:

$$\bar{n} \approx N^* \approx \sqrt{\phi_0 e^{(\Gamma-1)}}. \quad (9)$$

The comparison shown in Fig. 5 demonstrates that eqn(9) provides a fairly good approximation to the actual average length of chains observed in simulations. Although the number of simulation data points is small and more statistics should be desirable, it is remarkable that our simulation results are consistent with a universal behavior of the form $\bar{n} = f(\phi_0 e^{(\Gamma-1)})$, as expected from the simple thermodynamic

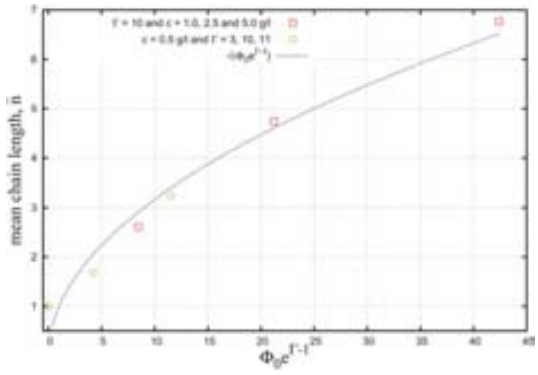

Fig. 5 Average number of colloids per chain as a function of a single parameter combining the volume fraction ϕ_0 and the magnetic coupling Γ. The symbols correspond to simulation results for different combinations of ϕ_0 and Γ and the dashed line corresponds to the theoretical approximation discussed in the text.

calculation. The good performance of the model is quite remarkable, given its simplicity. The result given by eqn(9) could be very useful in practical situations since it can be easily evaluated from characterization data (particle size, saturation magnetization and concentration) measurable in real colloidal dispersions. However, in applying eqn(9) in a real situation, we should keep in mind that our theoretical analysis is valid only provided that N^* is much smaller than the number of colloids in the sample, $N^* \ll N_0$.

In view of these analytical results, it is interesting to discuss again our results for the simulations in Fig. 1, which are not observed to reach an equilibrium state, at least during our simulation times. In the case of $\Gamma = 40$ and $\phi_0 = 5.23 \times 10^{-4}$, eqn(6) gives $N^* \sim 6.7 \times 10^6$ and an estimation from Fig. 1 suggests an equilibration time of the order of $\sim$10 years. Clearly, in this case, the reason that the equilibrium state is not observed is that in fact, it is unphysical and it would never be observed in a real experiment. This argument also justifies why the equilibrium state is not observed in previous simulation and experimental works, as in reality one is typically interested in large values of Γ in order to obtain strong magnetic effects (for example, in our previous work[10] we had $\Gamma \sim 10^3$).

The other situation following a power law in Fig. 1 ($\Gamma = 15$and $\phi_0 = 5.23 \times 10^{-4}$) corresponds to a very different case. Eqn(6) gives $N^* = 25$ and the extrapolation of the kinetics of Fig. 1 suggests an equilibration time in the order of 10 s. This calculation indicates that, in this case, we do not observe the equilibrium state due to the limitations in the computational time of the simulations. However, in a real experimental situation it should be possible to observe: initial kinetics obeying a power law followed by a slower approach to an equilibrium state, which will contain chains of substantial length. Values for Γ around 10–15 can be easily obtained experimentally by using superparamagnetic colloids with $d = 100$ nm and saturation magnetization of $\sim$30 emu g^{-1} (see for example, ref. 3). Hence, the behavior reported here should be readily accessible in real lab situations.

This work is supported by the Spanish Government (grants FIS2009-13370-C02-02, PET2008-02-81-01/02 and CONSOLIDER-NANOSELECT-CSD2007-00041), the Catalan Government (grant 2009SGR164) and SEPMAG Technologies SL. We acknowledge computer resources and technical assistance provided by the CESGA Supercomputing center (Finisterrae Supercomputer). JF acknowledges comments by Prof. Y. Levin at the International 2nd Soft Matter Conference (Granada, Spain).

References

1 C. T. Yavuz, et al, *Science*, 2006, **314**, 964.
2 J. L. Corchero and A. Villaverde, *Trends Biotechnol.*, 2009, **27**, 468.
3 E. Taboada, et al, *Adv. Funct. Mater.*, 2009, **19**, 2319.
4 J. E. Martin, et al, *Phys. Rev. E: Stat., Nonlinear, Soft Matter Phys.*, 2004, **69**, 021508.
5 N. Osterman, et al, *Phys. Rev. Lett.*, 2009, **103**, 228301.
6 J. H. E. Promislow, A. P. Gast and M. J. Fermigier, *J. Chem. Phys.*, 1995, **102**, 5492.
7 F. Martinez-Pedrero, et al, *Phys. Rev. E: Stat., Nonlinear, Soft Matter Phys.*, 2007, **76**, 011405.
8 G. P. Gajula, M. T. Neves-Petersen and S. B. Petersen, *Appl. Phys. Lett.*, 2010, **97**, 103103.
9 D. Heinrich, A. R. Goni and C. J. Thomsen, *J. Chem. Phys.*, 2007, **126**, 124701.
10 G. De Las Cuevas, J. Faraudo and J. Camacho, *J. Phys. Chem. C*, 2008, **112**, 945.
11 V. Schaller, et al, *J. Appl. Phys.*, 2008, **104**, 093918.
12 P. Domínguez-García, et al, *Phys. Rev. E: Stat., Nonlinear, Soft Matter Phys.*, 2007, **76**, 051403.
13 J. Faraudo and J. Camacho, *Colloid Polym. Sci.*, 2010, **288**, 207.
14 M. Benelmekki *et al.*, *J. Nanoparticle Research*, 2010, DOI: 10.1007/s11051-010-0218-6.
15 S. J. Plimpton, *J. Comput. Phys.*, 1995, **117**, 1.
16 A. O. Ivanov, Z. Wang and C. Holm, *Phys. Rev. E: Stat., Nonlinear, Soft Matter Phys.*, 2004, **69**, 031206.
17 F. Sciortino, *et al.*, *J. Chem. Phys.*, 2007, **126**, 194903.

Supplementary Material (ESI) for Soft Matter

Supporting Information for "Aggregation of superparamagnetic colloids in magnetic fields: the quest for the equilibrium state".

J.S. Andreu,[1,2] J. Camacho,[1] and J. Faraudo[2,*]

[1]*Dept. de Física, Universitat Autònoma de Barcelona, Campus UAB, E-08193 Bellaterra, Spain.*
[2]*Institut de Ciència de Materials de Barcelona (ICMAB-CSIC), Campus UAB, E-08193 Bellaterra, Spain.*

(Dated: January 17, 2011)

SIMULATIONS DESCRIPTION

The algorithm employed in our simulations is based on the Langevin stochastic equation of motion for each colloidal particle, as implemented in the LAMMPS program by the so-called Langevin thermostat `http://lammps.sandia.gov/doc/fix_langevin.html`. This method is based on a mesoscopic description, in which the colloids are simulated explicitly and the solvent molecules are treated implicitly. The force over a colloidal particle is given by the sum of three forces of different origin: (i) the interaction with other colloids and external fields $\vec{F}_c$, (ii) the viscous resistance $\vec{F}_f$ due to the solvent (treated as a continuum media) and (iii) the thermal fluctuations of the colloid due to collisions with individual solvent molecules $\vec{F}_r$. Then, the equation of motion for each colloid within this description is given by:

$$\vec{F}_c + \vec{F}_f + \vec{F}_r = m\vec{a}. \tag{1}$$

The force $\vec{F}_f$ is the viscous resistance experienced by the colloid in the solvent fluid, treated as a continuum medium. In its simplest version, is proportional to the velocity of the colloid $\vec{v}$ as given by the Stokes formula:

$$\vec{F}_f = -3\pi\eta d\vec{v} = -\frac{m}{\tau}\vec{v}. \tag{2}$$

where d is the diameter of the colloid, η is the viscosity of the solvent. The so-called dumping parameter τ is given by:

$$\tau = \frac{m}{3\pi\eta d}, \tag{3}$$

it has units of time and it gives the typical timescale for the relaxation of the colloid to a stationary state with velocity $\vec{v} = (\tau/m)\vec{F}_c$.

The $\vec{F}_r$ contribution in Eq.(1) takes into account the discrete nature of the solvent, i.e. it accounts for the collisions between solvent molecules and the colloid. It is an stochastic or random force corresponding to a white noise with zero average (it does not contribute to the mean velocity or the mean displacement of the colloid, which is purely deterministic). Our simulation algorithm, as implemented in LAMMPS, makes use of the fluctuation-dissipation theorem. The value of each component of $\vec{F}_r$ at a given time is obtained by generating a random number between -1 and 1 and multiplying it by the quantity:

$$\left[\frac{k_B T m}{\tau dt}\right]^{1/2}, \tag{4}$$

as described in [1] (dt is the integration time step employed in the simulation). In this way, the diffusion coefficient generated by the combined action of the random force and the friction is given by the Einstein relation:

$$D = \frac{k_B T}{3\pi\eta d}. \tag{5}$$

The purely diffusive motion is obtained in absence of external forces and colloidal interactions ($\vec{F}_c = 0$). In this case, the average displacement of the particles is zero and the fluctuations in particle positions obey the diffusive relation:

$$< r(t)^2 >= 6Dt. \tag{6}$$

Let us now comment on the $\vec{F}_c$ term in Eq.(1), which is the sum of interaction forces with all other colloids (and external fields if present). In our case, two different contributions have been included and can be written as $F_c = -\nabla U_{\rm LJ} - \nabla U_{\rm dd}$.

In order to avoid particle overlapping, and as a first approximation, we have modeled our colloids as soft dipolar spheres by considering a 6-12 Lennard-Jones potential truncated at $r_c^{\rm LJ} = \sigma_p = d$:

$$U_{\rm LJ} = 4\epsilon_p\left[\left(\frac{\sigma_p}{r}\right)^{12} - \left(\frac{\sigma_p}{r}\right)^{6}\right], \quad r < r_c^{LJ}. \tag{7}$$

which produces an effect quite similar to hard spheres of diameter $\sigma_p = d$.

The second contribution to the external force is due to the magnetic dipole-dipole interaction between colloidal particles. In all the simulations presented in this work, the magnetic dipole of each colloidal particle is fixed along a unique direction with a fixed magnetization corresponding to the saturation magnetization of the superparamagnetic colloids. This mimics the real situation in which the magnetic moment of the superparamagnetic particles align along a strong uniform external magnetic field, with a saturation magnetization $M_{\rm sat}$. Then, a magnetic force between colloids arise from the dipole-dipole interaction with an interaction energy given by:

$$U_{\rm dd} = \frac{1}{r_{ij}^3}\left[(\vec{p}_i\cdot\vec{p}_j) - 3(\vec{p}_i\cdot\hat{r}_{ij})(\vec{p}_j\cdot\hat{r}_{ij})\right]. \tag{8}$$

where $\vec{p}_i$ is the dipole corresponding to the i colloid and $\vec{r}_{ij}$ is the vector joining the two dipole centers. More details about how this dipole-dipole interaction is implemented in LAMMPS can be found at `http://lammps.sandia.gov/doc/pair_dipole.html`.

Supplementary Material (ESI) for Soft Matter
This journal is (c) The Royal Society of Chemistry 2010

Definition of dimensionless units in LAMMPS

In simulation is often convenient to rescale our system magnitudes to reduced dimensionless quantities. In the LAMMPS program the only dimensionless option for units is implemented by the *units lj* directive `http://lammps.sandia.gov/doc/units.html`. The dimensionless quantities are defined as follows. One defines a set of basic quantities which will be used to convert from dimensionless units to real units. These basic quantities are: an energy scale ϵ_0, a length scale σ_0 and a unit mass m_0. This choice also fixes the time scale, which is given by:

$$t_0 = \sigma_0 \sqrt{m_0/\varepsilon_0}. \tag{9}$$

In a completely equivalent way, one may select three of the four basic quantities ϵ_0, σ_0, m_0 and t_0 to construct a complete set and compute the remaining one using Eq.(9). The quantities evaluated in this dimensionless system are denoted here with a * superscript. Once we have selected our basic unit set, any other quantity of interest can be written in this new set of units.

In our case we have selected as the basic scales of our units system those parameters close to a molecule of water (our implicit solvent). Thus , $m_0 = 3.0 \times 10^{-26}$ kg, $\sigma_0 = 3.0$ Å and $\varepsilon_0 = 2.60 \times 10^{-23}$ J. With this election, the resulting time scale is $t_0 = 1.01 \times 10^{-11}$ s.

SIMULATION PARAMETERS

All the simulations performed in this work can be grouped in two different sets. A first set of simulations with the same concentration of magnetic colloids and with different values of the magnetic strength an a second set in which the colloids have the same magnetization but they are present in different concentrations. Tables I and II summarize the values used in defining these simulations. In table I we present the complete set of parameters common in all these simulations and in table II are presented all the parameters involved in the definition of different magnetic regimes and concentrations.

All the simulations consist of 8000 colloidal dipolar particles immersed in (implicit) water as a solvent at a constant temperature of $T = 300K$. The mass of the colloidal particles has been chosen to obtain a density close to the water density at that temperature to avoid any possible sedimentation effect of the colloidal particles in the simulation.

In the numerical integration of Eq.(1) in time steps of value dt, we have to keep in mind that the diffusive motion in a dt should be of a reasonable order of magnitude in order to produce an observable (but not too large) diffusive motion. However, the dipolar interactions between colloids can also cause the particles to overlap in excess. This could produce a too large repulsive force over the colloidal particles, resulting in a large velocity (after integration) due to the repulsive part of the Lennard-Jones potential and leading the system to an unphysical situation, which could make the integration procedure to fail. Then, the time step has to be large enough to reproduce the diffusion of the colloidal particles but small enough to avoid too large forces between particles whenever they overlap. In our case, we selected an integration time step of $\sim 1ns$ for all simulations where the magnetic interactions were present.

Regarding the Lennard-Jones interactions, the selected cutoff have been set to $r_c^{LJ} = d = 100nm$. In this way, the particles only interact through this repulsive force when they do overlap. The Lennard-Jones parameters σ_p, ϵ_p have been set to obtain a relatively hard sphere colloid, in which the distance between colloidal particles in contact is close to the original diameter of the particle (no overlapping).

Since the magnetic dipole-dipole interaction is a relatively long range force ($\sim 1/r^3$) its computation is one of the most time consuming parts in these simulations. Unfortunately, there is no available method in LAMMPS package that could be applied to reduce the computing time when accounting for this interactions (similar to the Ewald summation method used to compute the electrostatic interactions in charged systems). Then, we evaluated this interaction by direct summation of the forces in the real space, but limited to a certain region surrounding the particle defined with a cutoff ($r_{\rm c}^{\rm dd}$). The selected cutoff for all simulations is ten times the particle diameter $r_{\rm c}^{\rm dd} = 10d$ which results, in the worst case, in an error in the magnetic energy per particle smaller than $0.05k_BT$ (see table II).

TABLE I: Common simulation parameters for all simulations. The simulations units have been obtained by rescaling the real values using the basic units set presented in the previous section.

Parameter	real units	sim. units*
T	300 K	159
m_p	5.24^{-19} Kg	1.75×10^7
τ	55.6 ns	54.9
dt	1.01×10^{-9} s	100
$\sigma^{\rm LJ}$	100 nm	333.3
$\epsilon^{\rm LJ}$	1.30×10^{-20} J	500
$r_{\rm c}^{\rm LJ}$	100 nm	333.3
$r_{\rm c}^{\rm dd}$	1 μm	3333.3

SIMULATION ANALYSIS

We started the simulations by placing the 8000 particles following a cubic lattice arrangement inside the simulation box. The lattice constant was set according to the initial volume fraction ϕ_0 desired in each case. Then, the system was equilibrated at $T = 300K$ with the magnetic interactions switched off for a total simulation time of 0.1 s, with an integration time step of 1.01×10^{-10} s. In this situation, the expected diffusion

Supplementary Material (ESI) for Soft Matter
This journal is (c) The Royal Society of Chemistry 2010

TABLE II: Simulation parameters for the two sets of simulations presented in this work.

Sim-ID	Γ	ϕ	M_{sat}	magnetic dipole		axis box length		$-E_{\text{dd}}(r_c^{\text{dd}})$
-	-	-	[emu/g]	[$\times 10^{-17}$J/T]	[*]	[μm]	[*]	[k_BT]
1	3	0.52×10^{-3}	15.1	0.79	94075	20.0	66666.7	0.3×10^{-2}
2	10	0.52×10^{-3}	27.5	1.44	171756	20.0	66666.7	1.0×10^{-2}
3	10	1.05×10^{-3}	27.5	1.44	171756	15.7	52913.4	1.0×10^{-2}
4	10	2.62×10^{-3}	27.5	1.44	171756	11.7	38986.9	1.0×10^{-2}
5	10	5.23×10^{-3}	27.5	1.44	171756	9.3	30943.9	1.0×10^{-2}
6	11	0.52×10^{-3}	28.8	1.51	180139	20.0	66666.7	1.1×10^{-2}
7	12	0.52×10^{-3}	30.1	1.58	188149	20.0	66666.7	1.2×10^{-2}
8	15	0.52×10^{-3}	33.7	1.76	210358	20.0	66666.7	1.5×10^{-2}
9	40	0.52×10^{-3}	55.0	1.58	343512	20.0	66666.7	4.0×10^{-2}

coefficient for the colloids can be evaluated from the expression 5. In the other hand, this diffusion coefficient can be also obtained from simulation by evaluating the mean squared displacement (*msd*) calculated through the expression 6. In the case of $\phi_0 = 5.23 \times 10^{-4}$ the diffusion coefficient obtained from simulation is $D_{\text{sim}} = 4.29 \times 10^{-12} m^2 s^{-1}$ (the fitting is shown in figure 1). As it was expected, this value does agree with the theoretical value $D_{\text{theory}} = 4.39 \times 10^{-12} m^2 s^{-1}$ predicted through relation 5.

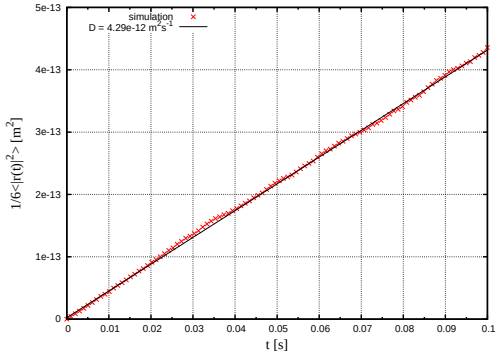

FIG. 1: Mean squared displacement obtained from simulation without magnetic interactions. In this case, the volume fraction was set to $\phi_0 = 5.23 \times 10^{-4}$ and the diffusion coefficient was obtained through the expression 6.

Once the system was equilibrated without the magnetic interactions, we used the last configuration obtained to restart the simulations but with the magnetic interactions switched on. These simulations were run for a total time between 1 and 3 s, depending on the simulation.

Some thermodynamical quantities such the potential energy, kinetic energy, etc. were stored in order to ensure the good performance of the simulation. Moreover, we have stored for each simulation the configuration of the system (positions, velocities, etc...) every 0.51 ms in real time (equivalent to store it every 500000 time steps). These files have been used to calculate any other quantity of interest presented in this work, such as the distribution of aggregates, the mean chain length, etc.

In order to quantify the aggregation phenomena found in the simulations, we had to define a criteria for the aggregation of two colloidal particles. According to typical experimental resolution in image processing techniques used to analyze the aggregating phenomena in such systems [3] we have defined a contact distance between colloids (i.e. the distance at which two colloids are joined together) as $d_c \equiv 1.15d$. With this selection, we got a good compromise between the statistical noise and the computed number of aggregates.

Prior to evaluate any equilibrium quantity from the simulations, we had to identify when our system was reaching equilibrium. By analyzing the time evolution of the potential energy, we could define a time interval in which we can assume that the system has -with reasonable approximation- reached an equilibrium state. In figure 2 the time evolution of the potential energy is shown for different simulations and table III summarizes the different selected ranges corresponding to each simulation.

TABLE III: Different time intervals and number of samples used when calculating the average chain length from simulations. These time intervals have been selected according to the time evolution of the potential energy, shown in figure 2 and the time evolution of $\bar{n}$ shown in Figs. 2-3 in the main paper.

Sim-ID	Γ	t_{min}	t_{max}	samples	$\bar{n}$	error (2σ)
-	-	[s]	[s]	-	[particles]	[particles]
1	3	0.5	1.0	1000	1.00217	0.00005
2	10	1.0	2.0	2000	1.6814	0.0006
3	10	1.2	2.0	1600	2.614	0.001
4	10	1.2	1.7	1000	4.742	0.006
5	10	0.7	1.2	1000	6.77	0.01
6	11	1.8	2.0	400	3.238	0.003

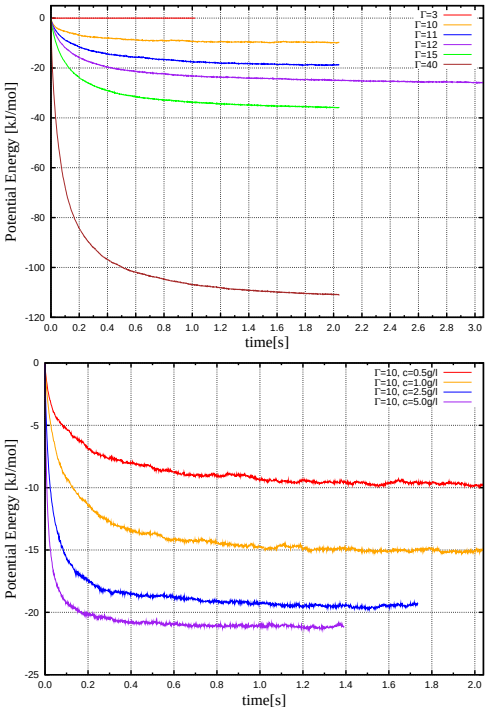

FIG. 2: Potential energy time evolution for all simulations. Different Γ values and $\phi_0 = 5.23 \times 10^{-4}$ (top panel) and $\Gamma = 10$ and different volume fractions (bottom panel).

We have also computed the average particle density function around each colloid (i.e. the colloid-colloid correlation function), Figure 3. In this figure the finite size of the colloids can be clearly appreciated (the density vanishes for separations smaller than the colloid size). Also, it shows how the colloids arrange themselves in chains in the z axis, with small fluctuations around the contact position. These details are also clearly observed in the accompanying movies.

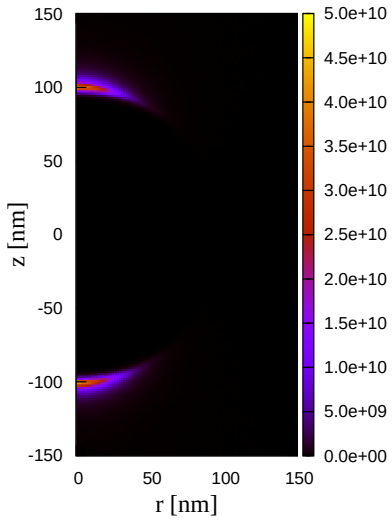

FIG. 3: Average particle density function corresponding to $\Gamma = 10$ and $\phi_0 = 5.23 \times 10^{-4}$. The evaluation has been carried out by averaging the last 1000 configurations corresponding to the last 0.5 s of simulation.

FINITE SIZE EFFECTS AND CUTOFF ANALYSIS

Here let us emphasize that finite size effects, effects of cut-off and in general the effect of long range interactions has been considered in detail prior to perform our production runs. We have considered simulations with 1000, 8000 and 10000 particles as well as cut-off values from 10 to 5 times the diameter of the colloids and different values for the radius of the neighbor list.

As an example, we show here the results form the same simulation employing four different schemes with the parameters indicated in the Table IV. The meaning of the parameters is as follows: cutoff is the cut off of the magnetic interactions as explained before, "every" indicates a build of neighbor list every this many steps, "page" indicates the number of pairs stored in a single neighbor page, "one" the maximum number of neighbors of one atom. The "page" and "one" options affect how memory is allocated for the neighbor lists and, though the default settings are fine for most simulations is recommended to boost them when dealing with large systems and/or large cut-off values. More information about the neighbor list algorithm and parameters optimized here can be found at:
`http://lammps.sandia.gov/doc/neighbor.html`
`http://lammps.sandia.gov/doc/neigh_modify.html`.

scheme	cutoff [σ]	every	one	page	steps/s
A	10	500000	5000	50000	2217
B	5	500000	5000	50000	3384
C	5	50000	500	5000	2598
D	5	10000	500	5000	2872

TABLE IV: Summary of schemes used in different test simulations to check the overall performance of the simulations and the effects of different cutoff and neighbor list parameters. The average computing velocity for each scheme has been calculated as the number of simulation steps over the total elapsed time.

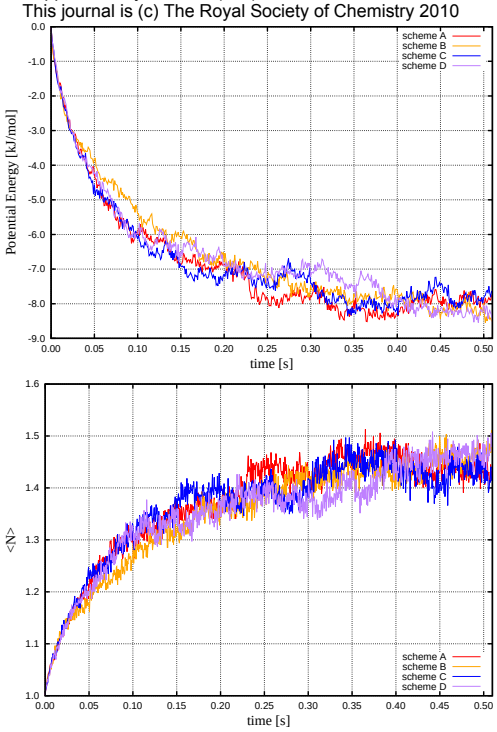

FIG. 4: Potential energy as a function of time (top) and mean number of colloid per aggregate (bottom) obtained considering a contact distance of 108nm.

These test simulations were performed using 1000 colloids, $\Gamma = 10$ and $\phi_0 = 5.23 \times 10^{-4}$ using a 4-processors grid in parallel. The results (Figure 4) show that a reduction of the employed cut off to half the value employed in the production runs does not affect the obtained results. Hence, the choice of this parameter is not as critical as one may think provided that one selects a value giving a truncation error in the magnetic energy much smaller than the thermal energy (as always is in our simulations, see Table II. In spite of this, our choices were highly conservative and we always employed in the production runs large cut off to minimize numerical errors in spite of the extremely high computational time required by these calculations.

The comparisons shown in Figure 4 and Table III also demonstrate that the simulation time depends crucially on the combination of the different parameters controlling the neighbors list, without affecting the precision of the results.

* Electronic address: jfaraudo@icmab.es

[1] B. Dunweg and W. Paul, Int J of Modern Physics C **2**, 817 (1991).
[2] C. Calero and J. Faraudo, Phys. Rev. E **80**, 042601 (2009).
[3] P. Domínguez-García, S. Melle, J. M. Pastor and M. A. Rubio, Phys. Rev. E **76**, 051403 (2007).

5.2 Article 2

"On-the- y coarse-grain methodology for the simulation of chain formation of superparamagnetic colloids in strong magnetic elds."
Jordi S. Andreu, Carles Calero, Juan Camacho and Jordi Faraudo
Physical Review E **85**, 036709 (2012)

On-the-fly coarse-graining methodology for the simulation of chain formation of superparamagnetic colloids in strong magnetic fields

Jordi S. Andreu,[1,*] Carles Calero,[2] Juan Camacho,[2] and Jordi Faraudo[1]
[1]*Institut de Ciència de Materials de Barcelona (ICMAB-CSIC), Campus UAB, E-08193 Bellaterra, Spain*
[2]*Departament de Física, Universitat Autònoma de Barcelona, Campus UAB, E-08193 Bellaterra, Spain*
(Received 20 December 2011; published 26 March 2012)

The aim of this work is the description of the chain formation phenomena observed in colloidal suspensions of superparamagnetic nanoparticles under high magnetic fields. We introduce a methodology based on an *on-the-fly* coarse-grain (CG) model. Within this approach, the coarse-grain objects of the simulation and their dynamic behavior are not fixed *a priori* at the beginning of the simulation but rather redefined *on the fly*. The motion of the CG objects (single particles or aggregates) is described by an anisotropic diffusion model and the magnetic dipole-dipole interaction is replaced by an effective short-range interaction between CG objects. The methodology correctly reproduces previous results from detailed Langevin dynamics simulations of dispersions of superparamagnetic colloids under strong fields while requiring an amount of CPU time orders of magnitude smaller. This substantial improvement in the computational requirements allows the simulation of problems in which the relevant phenomena extend to time scales inaccessible with previous simulation techniques. A relevant example is the waiting time dependence of the relaxation time T_2 of water protons observed in magnetic resonance experiments containing dispersions of superparamagnetic colloids, which is correctly predicted by our simulations. Future applications may include other popular real-world applications of superparamagnetic colloids such as the magnetophoretic separation processes.

DOI: 10.1103/PhysRevE.85.036709 PACS number(s): 05.10.−a, 82.70.Dd, 87.15.nr, 47.65.Cb

I. INTRODUCTION

In recent years, work in coarse-grain models for the description of soft matter and biomolecular systems is experiencing a remarkable outburst [1]. The reason is that the description of these systems at experimentally relevant time and length scales requires inclusion of phenomena occurring at very different scales. The objective of coarse-grain (CG) models is thus to retain sufficient molecular or nanoscale detail and yet remain amenable of simulation up to macroscopic time scales. Many approaches have been developed to construct CG models of different kinds of soft matter systems. For example, in the case of polymers, there is a long tradition of using CG models and the field is sufficiently mature so that there are systematic and rigorous approaches to build up CG models from accurate atomistic descriptions [2]. Also, in the field of biomolecular simulations, there are important developments such as the MARTINI force field [3] which allow the simulation of difficult problems such as the behavior of lipid vesicles or protein folding at millisecond or even larger time scales. New advances include also simulation packages specially designed for CG models of soft matter such as ESPRESSO [4].

Our interest here is the development of an improved CG model for a specific problem which is still difficult to simulate, namely the assembly of superparamagnetic colloids under strong magnetic fields. Superparamagnetic colloids are made of small nanoparticles of magnetic material (typically 5–10-nm iron oxide nanocrystals) embedded in a nonmagnetic matrix (typically polymers or silica) [5]. These particles have no magnetic dipole in absence of magnetic field but they develop very high magnetizations in the presence of a magnetic field, similar to those obtained with ferromagnetic materials. This highly tunable response and the possibility to functionalize their surface make these materials very interesting for applications such as capture and removal of biomolecules and pollutants, NMR contrast agents, and many others [6–8].

Our work is motivated by the difficulties encountered in modeling different kinds of real experimental situations involving superparamagnetic colloids. A relevant example is provided by the experiments by Chen *et al.* [9] of a dispersion containing superparamagnetic colloids designed as contrast agents for magnetic resonance imaging (MRI). In these experiments, a strong uniform magnetic field was applied to the dispersion. It was observed that the transverse relaxation time T_2 of protons in water changed with time, an effect which was attributed to the formation of chains of superparamagnetic colloids. In fact, the kinetics of chain formation was estimated from these experiments, spanning time scales from 10 to 10^3 s or more. Another relevant example is magnetophoresis [10], which is the motion of magnetic particles under an external magnetic gradient. Experimental evidence shows that the formation of chains induced by the external field speeds up the magnetophoresis process [11], which is orders of magnitude faster than that observed in the absence of chain formation [12]. It is worth noting that in these experiments, chains dissolve almost immediately after removal of the external field, as should be expected since superparamagnetic nanoparticles have no dipole in the absence of magnetic field. In this respect, these systems are very different from the widely studied (and simulated) dispersions of dipolar particles, which are able to form structures in the absence of an external magnetic field due to the interaction of their permanent dipoles [13–15].

The standard approach for simulation of chaining processes in magnetic colloids is the use of Langevin Dynamics (LD)

*jandreu@icmab.es

simulations (see, for example, [16,17]). This technique allows the inclusion of particle-particle interactions, thermal noise, and the friction due to the fluid. The resolution of the simulation technique is typically in the nanoseconds scale. Simulation runs up to a few seconds are possible, but they are highly intensive, requiring the use of parallel computing during several weeks [17]. These CPU requirements make this simulation technique unsuitable for the study of the problems mentioned above.

The need to account for microscopic time and length scales but also reach macroscopic time scales at low computational cost has motivated the development of a simulation strategy based on an *on-the-fly* CG procedure. The methodology which will be developed in this paper is a generalization of two procedures proposed in previous works: the method proposed by Miguel and Satorras [18] to study aggregation processes and the method proposed by Schaller *et al.* [19] to study magnetophoresis.

In the methodology proposed here, one starts by simulating the motion and interaction between individual colloids. As the simulation advances, colloids form chains due to the magnetic dipole-dipole attraction induced by the high external magnetic field. The motion of each particle inside a chain is not simulated explicitly. In our methodology, these chains are considered individual coarse-grain (CG) objects which move following certain effective rules and interact (and possibly aggregate) with other CG objects or single individual particles. In this way, the CG objects of the simulation are not fixed *a priori* at the beginning of the simulation but rather redefined *on the fly*. Thus we adjust the resolution of the calculations during the simulation run, allowing for the possibility of much longer simulation runs requiring less computer power. Preliminary simulation results and comparison with experiments, presented in a previous work [9], demonstrated the feasibility and utility of our approach. Here we will discuss in detail the physical basis of the model, the simulation methodology, and detailed comparison with more standard Langevin simulation techniques. All simulations of our model were performed employing the MAGCHAIN program, a C++ application developed in house, which is freely available for use of researchers. The code, its documentation, and usage examples can be found available for download at our web page [20].

The paper is organized as follows. In Sec. II, we describe the modeling of the system under study and the simulation technique. In Sec. III we validate the methodology by (i) comparing our results with those obtained employing standard LD simulations, (ii) discussing the effect of choosing other approximations for the diffusion coefficients and the effective interaction of the CG objects, and (iii) discussing the applicability of our methodology comparing with experimental results. The conclusions are presented in Sec. IV and some technical issues are detailed in the Appendix.

II. FORMULATION OF THE MODEL

The system which we are interested in describing is a colloidal dispersion of N_p superparamagnetic spherical particles of diameter d in a volume V and volume fraction ϕ_0:

$$\phi_0 = \frac{N_p}{V}\frac{\pi}{6}d^3. \tag{1}$$

In the absence of external magnetic field, the particles have no magnetic dipole and there is no formation of chains (no aggregation induced by the magnetic field). In the presence of a magnetic field H, the superparamagnetic particles acquire a certain magnetization $M(H)$. Since we are particularly interested in the case of very strong magnetic fields (as in the experiments of Ref. [9], for example), we consider that the particles have a magnetic dipole moment m_s (corresponding to the saturation magnetization M_s of the particles) pointing in the direction of the applied magnetic field (which we will take as the z axis). The strength of the magnetic interaction between particles as compared with thermal energy can be characterized by the magnetic coupling parameter Γ defined as

$$\Gamma = \frac{\mu_0 m_s^2}{2\pi d^3 k_B T}. \tag{2}$$

The behavior of superparamagnetic colloids under external fields is controlled by the values of these two parameters (ϕ_0 and Γ). In this paper, we are interested in situations (values of ϕ_0 and Γ) in which the external field induces formation of linear chains of colloids which grow irreversibly with time. Irreversible growth of linear chains has been found in simulations and experiments investigating the ranges of Γ between 40 and 3×10^3 and $\phi_0 < 0.15$ [16,17,22]. However, other structures are found at different ranges of ϕ_0 and Γ. For lower values of Γ, an equilibrium state is possible, in which colloids aggregate in linear (nonbranched) chains with an equilibrium length given by $\sqrt{\phi_0 e^{\Gamma-1}}$ [17]. In the opposite situation of larger values of ϕ_0 and Γ, different aggregate structures can be found, including thick chains (obtained from lateral aggregation of linear chains), bundles, and more complex fibrous structures [22]. All these more complex situations, different from irreversible growth of linear chains, will be left for future extensions of the model.

As key ingredients to retain the underlying physics of irreversible chain growth, we consider both the diffusive motion of particles and chains and their respective magnetic and steric interactions. The main approximations of our model will be to ignore the details of the particles forming the chains and to replace the actual magnetic dipole-dipole interaction by an effective short-range interaction, less demanding from the computational point of view.

Our model to study the kinetics of chain formation in these systems consists of CG objects which are chains made of s particles, including the case $s = 1$, which corresponds to a single particle. The first ingredient of the model is the diffusion coefficient of the CG objects. For single, isolated particles ($s = 1$) we have

$$D_1 = \frac{k_B T}{3\pi\eta d}, \tag{3}$$

where η is the viscosity of the fluid. A chain containing $s > 1$ particles exhibits anisotropic diffusion, characterized by a diffusion coefficient $D_s^{\parallel}$ in the direction parallel to the long axis of the chain and $D_s^{\perp}$ in the directions perpendicular to the long

axis. There are several possibilities for the analytical form of these diffusion coefficients, depending on the exact geometry assumed for the chains and the degree of approximation of the calculation. Here, in order to keep the model as simple as possible, we consider the following expressions valid for elongated objects (slender body theory [21]):

$$\frac{D_s^{\parallel}}{D_1} = \frac{3}{2s}\left[\ln(2s) - \frac{1}{2}\right], \tag{4}$$

$$\frac{D_s^{\perp}}{D_1} = \frac{3}{4s}\left[\ln(2s) + \frac{1}{2}\right]. \tag{5}$$

Strictly speaking, Eqs. (4) and (5) are valid only for large s. Therefore we employ Eqs. (4) and (5) for chains with $s > 2$ and use a simple interpolation between the diffusion coefficients corresponding to CG objects with $s = 1$ [Eq. (3)] and $s = 3$ [Eqs. (4) and (5)] for chains with $s = 2$. Such a choice gives results indistinguishable from those provided by more sophisticated and accurate expressions of the diffusion coefficients (see Sec. III B).

The second ingredient of the model is the definition of the effective interaction between CG objects. A CG object of length s interacts with other CG objects through an excluded volume interaction (hard core) corresponding to a cylinder of length $s \times d$ and diameter d. They also interact through dipole-dipole interactions. In order to simplify and speed up the simulations, we have replaced the actual dipole-dipole magnetic interaction between colloids by an effective, short-range interaction between the CG objects. This interaction is defined as follows. For a given CG object, we define two spherical attractive regions of radius $r_a(s)$ (which depend on the length of the chain s) located at the two ends of the chain. As illustrated in Fig. 1, these regions are designed to mimic the region at which the magnetic attraction between a chain of particles (magnetized in the z direction) and an incoming test dipolar particle is equal or stronger than the thermal energy k_BT. The values of $r_a(s)$ are calculated by finding the distance in the z axis at which the magnetic interaction energy E_{mag} between a chain of s particles and a single test particle is equal to $-k_BT$. Therefore $r_a(s)$ is given by the solution of

$$\frac{E_{\mathrm{mag}}}{k_BT} = -\Gamma \sum_{n=0}^{s-1} \frac{1}{[2r_a(s)/d + 1/2 + n]^3} = -1. \tag{6}$$

The results of Eq. (6) for different values of Γ are also shown in Fig. 1. Once we have defined the range of the interaction, we need to define the strength of this interaction. In order to keep our model as simple as possible, we simply assume that all events in which a CG object enters into the interaction region of another CG object will lead to instantaneous aggregation. This rule has been employed previously in the interpretation of experimental results and it has been suggested by direct observations of chain formation under a microscope (see Refs. [23,24]). As we will show in the next section, this rule reproduces correctly the results obtained from LD simulations in which the magnetic interaction is computed accurately. The sensitivity of the results to the choice of r_a will be also discussed in Sec. III B.

Once the basic ingredients for the model (rules for motion and interaction) are defined, it is necessary to specify the algorithm for the numerical solution of the model. In our case, the diffusive motion of the CG objects is simulated using the Brownian dynamics technique [25]. At each time step Δt a random displacement in each direction is generated with a Gaussian distribution with zero mean and variance $2D_s\Delta t$, where D_s is the diffusion coefficient of the object (single particle or chain) in the direction of motion (x, y, or z). Also, at each time step the distances between CG objects are checked in order to detect penetration of a CG

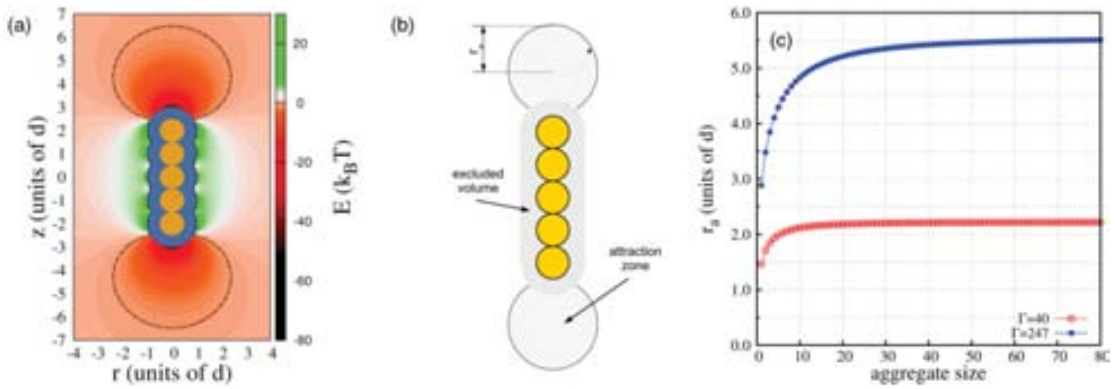

FIG. 1. (Color online) (a) Two-dimensional (2D) map corresponding to the interaction energy between an incoming test dipolar particle and a chainlike aggregate formed by five colloids with a magnetic coupling of $\Gamma = 40$. The black dashed line delimits the region with ($E < -k_BT$). The region excluded by the finite size of the five spheres is shown in blue (the interaction energy map is not evaluated inside this region). (b) Sketch of the attraction model implemented in the MAGCHAIN code. Each CG object has two attraction zones, modeled as a sphere of radius r_a [Eq. (6)] tangent to the edge of the aggregate. Any particle entering into these zones will immediately aggregate forming a longer chain. (c) Dependence of the radius (r_a) of the attraction regions on the aggregate size for two different values of the coupling parameter, $\Gamma = 40$ (open symbols) and $\Gamma = 247$ (solid symbols). The attraction radius increases abruptly for short chains and tends to a constant value for longer chains. All the distances are expressed in terms of the diameter d of the colloid.

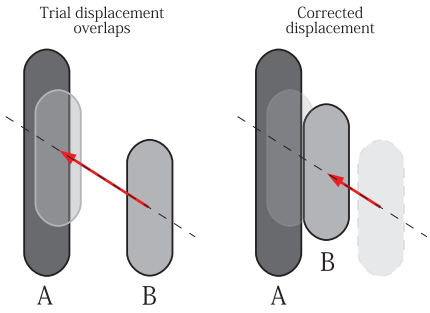

FIG. 2. (Color online) Sketch corresponding to the scheme applied to avoid the overlap between CG objects during simulations. If the random displacement performed on object B produces an overlap between B and another CG object (A), the moving aggregate (B) is placed in contact with the second aggregate (A) according to the trajectory followed during the random displacement.

object inside the region of aggregation of another CG object, as explained above, or to detect possible overlaps between them. In the case of aggregation of two CG objects, a new CG object is created (and the two previous CG objects are erased from the simulation) with length s, obtained from adding the lengths of the two aggregating chains and located at the center of mass of the aggregating CG objects. In the case of overlap between two CG objects without penetration into the aggregation region, we consider that the two chains collide. In this case, the moving CG object is placed in contact with the other one (without overlapping) at the collision coordinates defined by the trajectory previously followed (see Fig. 2). Finally, it should be noted here that the selection of an appropriate time step Δt for the simulation is a crucial issue. A detailed discussion on the selection of Δt is given in the Appendix.

Hence a typical simulation run is as follows. The simulation starts from a pre-equilibrated system containing N_p colloids (CG objects with $s = 1$). As the simulation goes on, colloids aggregate and chains with increasing values of s appear. Consequently, the number of CG objects of the simulation decreases with time and the simulation speeds up as the time advances, as we will discuss in detail in the following section. As a simulation output, we obtain the number of chains containing s colloidal particles at time t, $n_s(t)$. During the simulation, we also monitor the time evolution of the average number of colloidal particles in a chain $\langle N(t)\rangle$ defined as in [16,18]

$$\langle N(t)\rangle = \frac{\sum_s s n_s(t)}{\sum_s n_s(t)} = \frac{N_p}{\sum_s n_s(t)}, \tag{7}$$

and the probability of finding an aggregate of size s at a given time, defined as

$$p(s;t) = \frac{n_s(t)}{\sum_s n_s(t)}. \tag{8}$$

III. VALIDATION AND APPLICATION OF THE MODEL

A. Comparison with Langevin dynamics simulations

Our objective in this section is to compare the performance and results obtained using the model described in Sec. II with standard LD simulations of the same system. Briefly stated, Langevin dynamics simulations consist of solving the Newton equations of motion for each particle taking into account external forces, the interaction forces between particles (magnetic and steric), the viscous drag from the solvent, and a stochastic force arising from the thermal noise due to the fact that the system is at a given temperature T. This comparison between our simplified CG method and more detailed LD simulations will help to clarify the validity of the approximations introduced in our model, as described in the previous section. In order to perform a significant comparison between this procedure and the standard LD simulation technique, we have selected two cases with very different magnetic coupling Γ which were studied in previous works. The details for these systems are summarized in Table I and were denoted as case 1 and case 2.

Let us consider first case 1, which corresponds to a dispersion of 100-nm superparamagnetic colloids at a volume fraction $\phi_0 = 5.23 \times 10^{-4}$ which have a magnetic coupling parameter $\Gamma = 40$ at saturation (i.e., under strong magnetic fields). This system was studied employing LD simulations in Ref. [17] by using the standard LAMMPS simulation package [27] (version 21May2008). Now, we will compare these published results obtained with the standard LD technique with our CG methodology described in the previous section. These simulations will be denoted as LD40 (the Langevin dynamics case) and CG40 (our coarse grain methodology). The parameters employed in the numerical algorithm are given in Table II. For completeness, we also give the parameters employed in the LD simulations. It should be noted that the LD simulations require a small time step (of the order of the ns). This small time step is needed in order to avoid a simulation crash in simulations involving chains of colloids, since the motion of colloids inside a chain involves very small displacements which need to be resolved with high precision. In our CG methodology (which does not consider the structure of chains), we can use much larger time steps as shown in Table II. A detailed discussion on the selection of the time step in our methodology is given in the Appendix.

Typical snapshots of the simulation are shown in Fig. 3 and the results for $\langle N(t)\rangle$ are shown in Fig. 4. The snapshots illustrate the different resolution employed in the CG40 and LD40 simulations. As seen in the snapshots, the LD40 simulation resolves the individual particles making up the chains whereas the chains are structureless in the CG40 simulation. It should be noted that the chains obtained in the LD40 simulation are almost perfectly linear and are not significantly different from the coarse-grain objects of the CG40 simulation. As shown in Fig. 4, the values of $\langle N(t)\rangle$ obtained from both simulations (CG40 and LD40) are in excellent agreement. For example, at $t = 1$ s, the mean aggregate size for the CG40 simulation is $\langle N\rangle_{CG} = 12.10$ and the value calculated from LD simulations is almost identical, $\langle N\rangle_{LD} = 12.14$. Therefore we can conclude that the simplifying approximations included in this methodology (particularly those regarding the calculations

TABLE I. Characteristics of the colloidal dispersions of superparamagnetic particles simulated with CG and LD techniques. ϕ_0 and Γ are defined by Eqs. (1) and (2), ρ_p is the density of a single colloid, d is its diameter, and D_1 is its diffusion coefficient. T is the temperature of the dispersion and η is the viscosity of the solvent (water) at this temperature.

	Γ	ϕ_0	ρ_p (g/cm^3)	d (nm)	T (K)	η (Pa s)	D_1 (m^2/s)
Case 1	40	5.23×10^{-4}	1.0	100	300	1.0×10^{-3}	4.39×10^{-12}
Case 2	247	4.64×10^{-6}	3.1	88	310	0.692×10^{-3}	7.46×10^{-12}

of particle-particle magnetic interaction) do not affect the average size of chains.

We have performed a more detailed comparison between both approaches by comparing the distribution of chains of size s at certain times. In Fig. 5 we compare the corresponding probability distribution [defined in Eq. (8)] at $t = 1$ s obtained from LD40 and CG40 simulations. The agreement between both results after 1 s is remarkable, and only slight differences are observed. As shown in Fig. 5, the distribution of chain sizes is very broad, with significant probabilities of finding chains well above and well below the average length (including isolated particles).

Now, let us consider the case denoted as case 2 in Table I corresponding to one of the samples considered in the experiments in [9]. In this case, the particles have larger saturation magnetization ($\Gamma = 247$) but the dispersion is more diluted ($\phi_0 = 4.64 \times 10^{-6}$). We have performed Langevin dynamics simulations as well as simulations employing our methodology, as in case 1. These simulations will be denoted as LD247 and CG247, respectively. A list of relevant simulation parameters for LD247 and CG247 simulations is given in Table II. The results obtained for $\langle N(t) \rangle$ are also given in Fig. 4. The results for the probability distribution $p(s;t)$ at $t = 5$ s are shown in Fig. 6. Again, we obtain a good agreement between the predictions of both simulation methodologies, both in the average size of chains and in the probability distribution of chain sizes.

As shown in Table II, both for the case with $\Gamma = 40$ and $\Gamma = 247$, the computational cost of the CG simulation technique is much lower than the corresponding LD simulation. For example, we note that a production run of 6 s for the LD247 simulation requires about 4.5 days of calculations, with the program running in parallel in an 8-core AMD Opteron Magny Cours 6136 processor. In contrast, the CG247 simulation requires less than 4 h to simulate the same physical time using a single core of the same processor employed in the LD247 run. In addition, we can reach surprisingly long time scales in our CG247 simulation with a very low computational cost (see Table II). In simulation CG247, we reach simulated times up to 10^3 s in a 1-day calculation, a time scale two orders of magnitude larger than that accessible using Langevin dynamics simulations.

The CPU costs shown in Table II demonstrate that our simulation technique allows us to perform simulations of the two systems considered here with an extremely reduced computational effort as compared to Langevin dynamics simulations. Moreover, it is also important to notice that the required CPU time for the CG approach to simulate a certain time interval is reduced during a simulation, since the number of CG objects decreases as the simulation advances. This effect is clearly shown in Fig. 7 for the CG40 simulation. We also show that the rate between the elapsed CPU time and the corresponding real time simulated depends linearly with the number of CG objects (see the inset Fig. 7). It should be noted that in the LD simulations the opposite effect was observed; the fact that the individual motion of the particles inside the chains are fully resolved makes LD simulations increasingly inefficient as time goes on.

B. Further discussion on the approximations of the model

1. Diffusion model

As it has been already mentioned, one of the two key ingredients of the CG approach is the diffusion model adopted to describe the motion of the coarse-grain objects. In order to check the possible influence of the model selected, we have also performed simulations with a different diffusion model proposed by Tirado *et al.* [28] in which they describe the

TABLE II. Set of parameters used for numerical integration in the coarse grain (CG40 and CG247) and the Langevin dynamics (LD40 and LD247) simulations. N_p is the number of particles in the simulation, L_z and $L_x = L_y$ are the sizes of the simulation box (in units of particle diameters) in the directions parallel and perpendicular to the magnetic field, respectively (periodic boundary conditions were employed in all simulations). Δt is the time step and t_f is the total simulated time. We also indicate the total amount of CPU time employed in the calculation, calculated as the number of cores used times the total elapsed time. In all our calculations we have used an 8-core AMD Opteron Magny Cours 6136 processor.

Label	System	N_p	L_z	$L_x = L_y$	Δt (s)	t_f (s)	No. cores	CPU cost
LD40	case 1	8000	200	200	1.02×10^{-9}	2.04	8	998 h
LD247	case 2	4000	767	767	3.06×10^{-9}	6.12	8	866 h
CG40	case 1	8000	512	128	2.280×10^{-4}	5	1	25 h
CG247	case 2	8000	1534	767	1.038×10^{-4}	1000	1	24 h

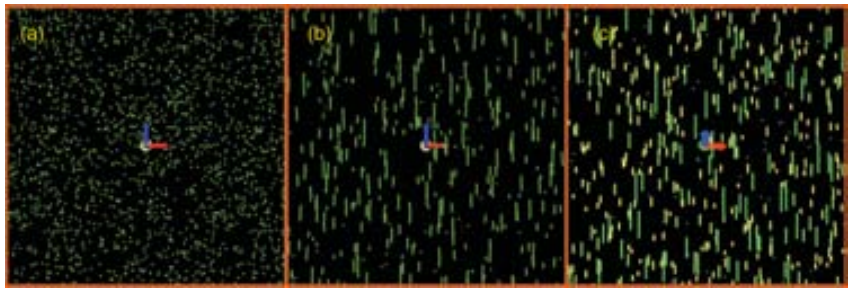

FIG. 3. (Color online) Snapshots from simulations with $\Gamma = 40$ (case 1 of Table I). (a) Initial configuration of a simulation ($t = 0$). (b) Snapshot from Langevin dynamics simulations (LD40) at $t = 0.28$ s. Note that the simulation resolves the individual particles building up the chains. (c) Snapshot from coarse grain simulations at $t = 0.28$ s. Now the chains are the CG objects; individual particles are no longer considered once they form part of a chain. Chains are colored according to their length for an easier visualization. Left and center images were created using VMD [26]. Right image was created using our own visualization software available in the web [20].

translational motion of right circular cylinders also accounting for the so called *end effects*. Following the same approach as in [23], we have used the expressions

$$\frac{D_s^{\parallel}}{D_1} = \frac{3}{2s}[\ln(s) + \gamma^{\parallel}(s)], \tag{9}$$

$$\frac{D_s^{\perp}}{D_1} = \frac{3}{4s}[\ln(s) + \gamma^{\perp}(s)], \tag{10}$$

where $\gamma^{\parallel}$ and $\gamma^{\perp}$ are the *end-effect* functions defined as

$$\gamma^{\parallel}(s) = -0.21 + \frac{0.90}{s}, \tag{11}$$

$$\gamma^{\perp}(s) = 0.84 + \frac{0.18}{s} + \frac{0.24}{s^2}. \tag{12}$$

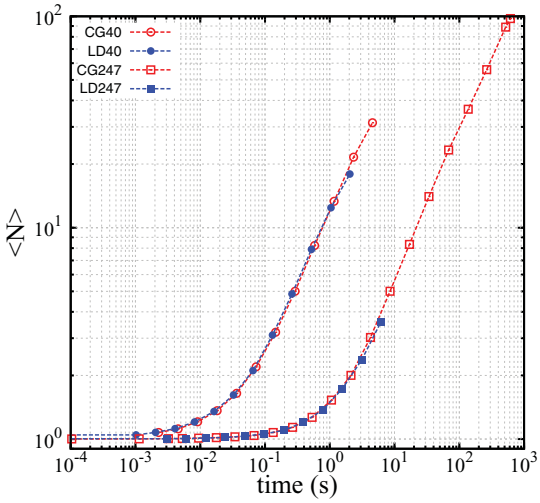

FIG. 4. (Color online) Time evolution of the average number of particles $\langle N(t) \rangle$ in a chain, Eq. (7). Comparison between the results obtained from Langevin dynamics (solid symbols) and coarse grain (open symbols) simulations for the two different systems studied. Circles correspond to case 1 ($\Gamma = 40$, $\phi_0 = 5.23 \times 10^{-4}$) and squares to case 2 ($\Gamma = 247$, $\phi_0 = 4.64 \times 10^{-6}$).

We have computed the mean aggregate size $\langle N(t) \rangle$ using both diffusion models for the CG40 system and the results obtained are plotted in Fig. 8. As it can be seen from these results, no significant differences are found in the average number of particles $\langle N(t) \rangle$ obtained with both diffusion models. For this reason we can conclude that both models are suitable for the description of the diffusive motion of the chainlike aggregates in such systems and our selection of the elongated rod model [Eqs. (4) and (5)] instead of Eqs. (9)–(12) for the simulations was based on its major simplicity.

2. *Effective interaction: Attraction radius*

As explained in detail in Sec. II, we have defined the aggregation regions for each CG object as the surrounding space in which the magnetic interaction energy between the CG object and a dummy single particle is equal to or smaller than $-k_B T$. As shown in Fig. 1, the attraction radius r_a defining this region depends on the size of the considered aggregate and on the magnetic coupling parameter Γ [see Eq. (6)]. It is observed that for small chains the attraction radius increases with their size and tends to a constant value

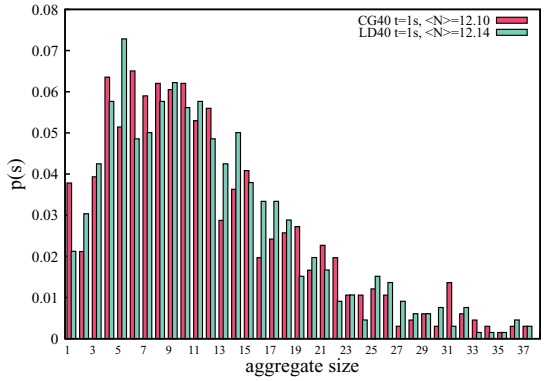

FIG. 5. (Color online) Comparison between the probability distribution to find an aggregate of size s [defined in Eq. (8)] at $t = 1$ s obtained from LD40 and CG40 simulations.

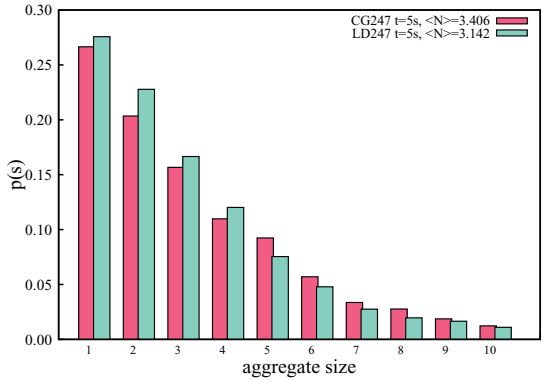

FIG. 6. (Color online) Comparison between the probability distribution to find an aggregate of size s at $t = 5$ s obtained from LD247 and from CG247.

for larger chains (the addition of a new particle into the same aggregate does not significantly contribute to the interaction magnetic energy). Here, we would like to demonstrate the importance of accounting for the s dependence of $r_a(s)$ in the simulations.

To this end, we have performed two additional simulations in which the s dependence of $r_a(s)$ is ignored. A first simulation (denoted as CG40-min) corresponds to a repetition of the simulation CG40 of the previous section (see Table II) but using $r_a = 1.46d$ for all chains. We also performed another simulation (denoted as CG40-max) in which we employed the value $r_a = 2.20d$ for all chains. These values correspond to

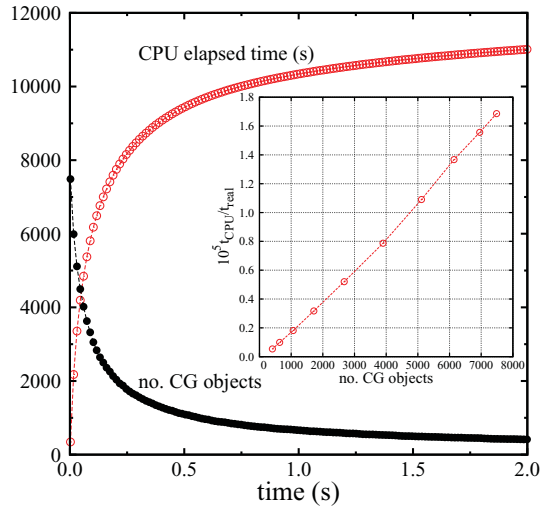

FIG. 7. (Color online) Elapsed CPU time (open circles) and number of CG objects (solid circles) as a function of the real simulated time for the CG40 simulation. Inset: Rate between the elapsed CPU time and the real simulated time as a function of the number of CG objects present in the CG40 simulation.

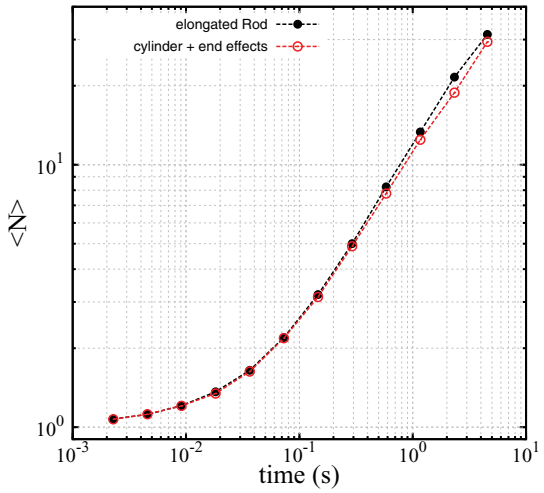

FIG. 8. (Color online) Comparison between the results obtained from the elongated rod approximation [corresponding to Eqs. (4) and (5) and represented by solid circles] and the cylinder approximation with end effects [corresponding to Eqs. (9) and (10) and represented by open circles] when computing the mean chain size of the aggregate $\langle N \rangle$ for the CG40 system.

the minimum and maximum values of $r_a(s)$ employed in the original CG40 simulation (see Fig. 1).

All these approaches give us different dynamics of the system as it is shown in Fig. 9 where the mean aggregate size $\langle N \rangle$ is plotted as a function of time together with

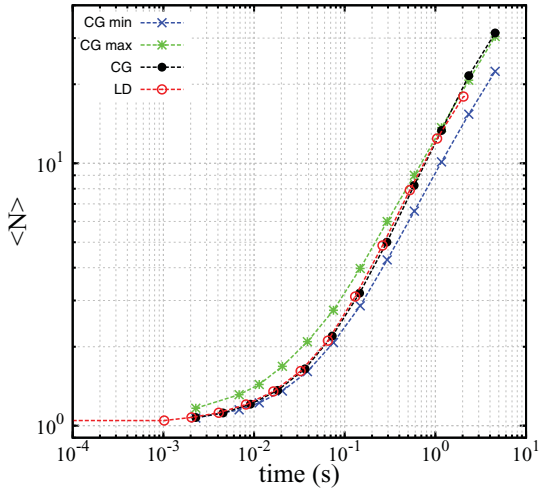

FIG. 9. (Color online) Comparison of the calculated mean chain size $\langle N \rangle$ between two simplified versions of the coarse-grain model (see main text for details) and the full version. Crosses correspond to the CG40-min simulation, stars to the CG40-max simulation and solid circles correspond to the CG40 (full version) simulation. We also show the Langevin dynamics results (LD40, open circles).

TABLE III. Set of parameters used for numerical integration in the coarse grain simulations of the same colloids described in case 2 in Table I but for different volume fractions ϕ_0. N_p is the number of particles in the simulation, L_z and $L_x = L_y$ are the sizes of the simulation box (in units of particle diameters) in the directions parallel and perpendicular to the magnetic field, respectively. Δt is the time step and t_f is the total simulated time. As in Table II, we also indicate the total amount of CPU time employed in the calculation.

Label	N_p	L_z	$L_x = L_y$	ϕ_0	Δt (s)	t_f (s)	CPU cost
CG247-00	8000	2436	1218	1.16×10^{-6}	1.038×10^{-4}	1221	130 h 1min
CG247-01	8000	1933	966.5	2.32×10^{-6}	1.038×10^{-4}	859	59 h 53min
CG247-02	8000	1534	767	4.64×10^{-6}	1.038×10^{-4}	616	29 h 35min
CG247-03	8000	1218	609	9.28×10^{-6}	1.038×10^{-4}	806	14 h 52min

the corresponding LD results. We observe that the CG40 simulation evolves from an initial behavior close to the CG-min simulation to a behavior closer to the CG-max simulation. Analogous calculations for the CG247 system (not shown here) exhibit identical behavior. In consequence, is important to take into account the full $r_a(s)$ dependence in the simulations as described in our formulation of the model in Sec. II.

C. An example of practical application: Chain growth and T_2 measurements

Our objective in this subsection is to illustrate the applicability of the methodology developed here in situations of interest for applications of superparamagnetic colloids. As an example, let us consider the use of superparamagnetic colloids as contrast agents in magnetic resonance imaging (MRI). An important issue in this application is the possibility of chain formation of colloids due to the strong magnetic fields applied in the experiments. The formation of chains of colloids in the sample increases the transversal relaxation time T_2 of protons, which is an undesired effect in practice. In a previous work, we have employed a preliminary version of our simulation code to analyze this possibility in MRI [9]. We have found that under conditions of interest for MRI, significant chaining occurs. We would like to discuss here the results of our simulations as well as compare our results with the experiments in a more direct way than the preliminary simulations presented in Ref. [9].

The system considered here is a dispersion of superparamagnetic colloids in water with the physical properties of case 2 in Table I but now we have considered four different values of the initial volume fraction of colloids, according to the experiments in Ref. [9]. The corresponding volume fractions are given in Table III. The simulations of these systems, performed with the methodology discussed in Sec. II, have been labeled as CG247-00, CG247-01, CG247-02, and CG247-03, respectively, and all the technical details are given in Table III (note that the CG247-02 simulation in this table is identical to the simulation CG247 of Table II).

The results for the average number of particles in a chain $\langle N(t) \rangle$ are given in Fig. 10 for the time scales relevant in the experiments of Ref. [9]. In all cases we observe significant chain formation even in the case of the smallest concentration. Of course, the kinetics of chain formation is observed to slow down as the concentration of colloids decreases.

The formation of chains has direct impact on the transversal relaxation rate $1/T_2$ of water protons. Initially ($t = 0$), the relaxation rate of water protons $1/T_2^{(0)}$ is determined by the presence of a random distribution of isolated (dispersed) colloids. As time goes on, chains form and modify the T_2 response of the surrounding water protons. Therefore the experimentally measured T_2 at a given instant t depends on the distribution of chain sizes at that time t. As proposed in Ref. [9], we can give a theoretical prediction of the relaxation rate $1/T_2(t)$ from our simulation results by computing the following average:

$$\frac{1}{T_2(t)} = \frac{1}{N_p} \sum_s s n_s(t) \frac{1}{T_2^{(s)}}, \tag{13}$$

In Eq. (13), $1/T_2^{(s)}$ is the relaxation rate of water protons near a colloid forming part of a chain containing exactly s colloids and $n_s(t)$ is the number of chains of size s at time t, as defined in Sec. II. Our simulation results provide $n_s(t)$ whereas the calculation of $1/T_2^{(s)}$ requires an additional study of the motion of water protons near a chain containing s colloids. For the particles of the experiments (case 2 in our Table I), the theoretical results for $1/T_2^{(s)}$ were given in Fig. 9 of Ref. [9].

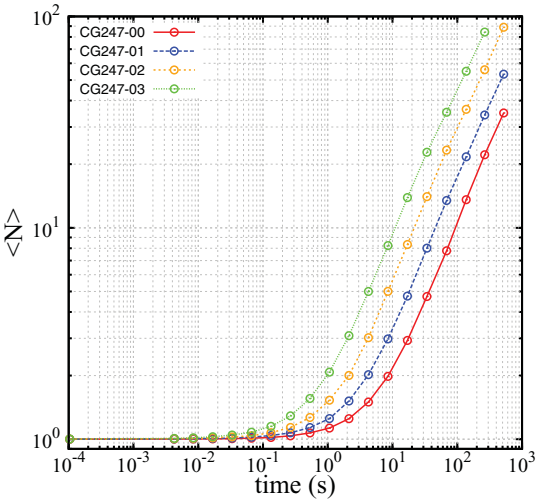

FIG. 10. (Color online) Average number of colloids in a chain $\langle N \rangle$ as a function of time for the simulations described in Table III.

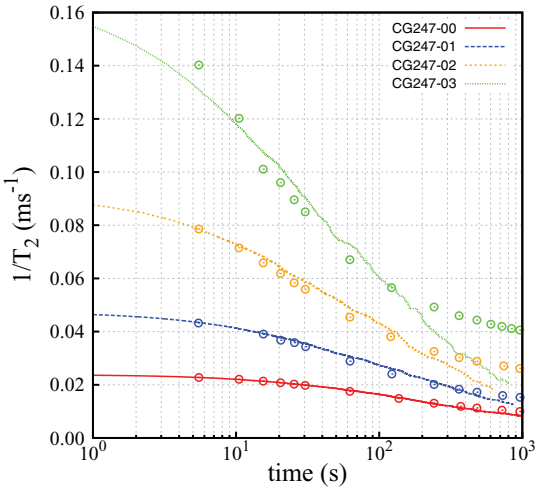

FIG. 11. (Color online) Evolution of the relaxation rate $1/T_2$ of water protons in four dispersions containing different concentrations of superparamagnetic colloids. Solid lines correspond to the predictions obtained from the simulations described in Table III and Eqs. (13) and (14). Symbols correspond to experimental data extracted from Fig. 5(a) in Ref [9].

These results can be well fitted to an analytical expression of the form

$$\frac{1}{T_2^{(s)}} = \frac{1}{T_2^{(0)}} s^{-a \cdot s^b}, \tag{14}$$

where a fit to the calculations in Ref. [9] gives $a = 0.0415$ and $b = 0.45$. Now, making use of such a fit in Eq. (13) and the values of $n_s(t)$ obtained from simulations CG247-00, CG247-01, CG247-02, and CG247-03, we can make a theoretical prediction for the relaxation rate $1/T_2(t)$. The results are compared in Fig. 11 with experimental results. The simulations show a remarkable agreement between theory and experiments for times corresponding to mean chain length $\langle N \rangle$ up to 50 colloids. It should be noted that in the case of very long chains, the measurements are not reliable due to sedimentation effects [9].

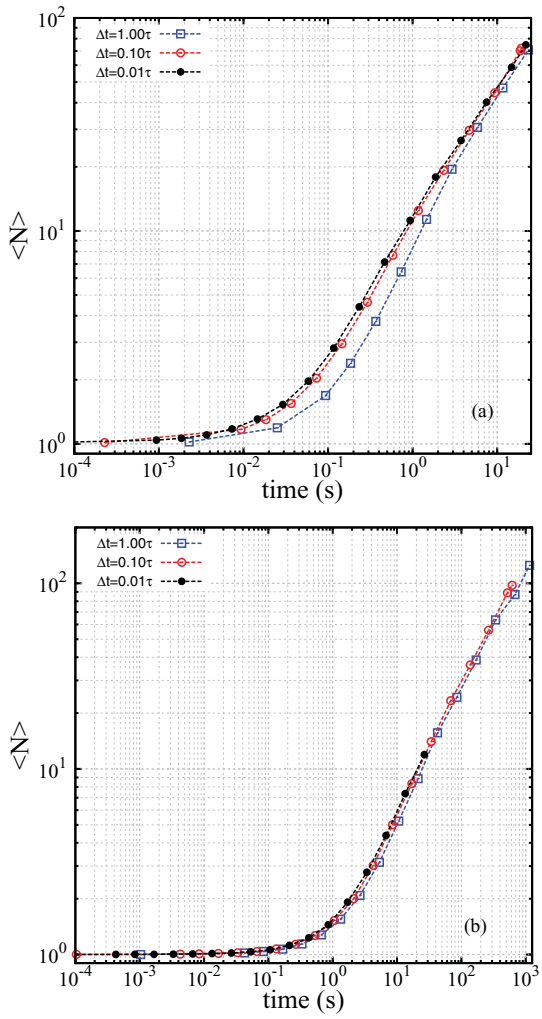

FIG. 12. (Color online) Influence of the integration time step Δt in the simulations CG40 and CG247 (top and bottom, respectively) on the time evolution of $\langle N \rangle$.

IV. CONCLUSIONS

In this paper, we have introduced an on-the-fly coarse-grain model to describe the chaining phenomena observed in dispersions of superparamagnetic colloids under strong external magnetic fields. We report simulation results with such methodology, which show good agreement with those obtained from more detailed Langevin dynamics (LD) simulations. The great advantage of the methodology presented here is its low computational cost in terms of CPU time. As a consequence, we are able to run longer simulations, reaching time scales not accessible in LD simulations. In order to illustrate the applicability of the code in experimentally relevant situations, we have considered the waiting time dependence of the relaxation rate $1/T_2$ of water protons observed in magnetic resonance experiments of dispersions of superparamagnetic colloids [9]. Experimental results corresponding to waiting times from 1 to 10^3 s were correctly predicted by our simulations.

The model, in its present formulation, cannot be applied to situations more complex than irreversible chain growth. However, it seems possible to expand the model to consider other situations of interest. A first generalization could involve the inclusion of lateral interactions between the chains [29], which are responsible for the formation of thick chains, observed at volume fractions larger than those considered here [22]. Optical microscopy observations [11] also show the formation of thick chains and bundles in magnetophoresis experiments (motion of magnetic particles under magnetic gradients). Hence the inclusion of lateral interactions and

deterministic motion of the CG objects will be needed in order to extend our model to study magnetophoresis. Another interesting extension, which is now under way, is the inclusion of the possibility of chain breaking due to thermal fluctuations, a mechanism relevant at low values of the magnetic coupling parameter Γ. This extension of the model will allow us to study in depth the equilibrium state described in Refs. [17,30].

A final improvement to the model could be taking into account the full magnetic response $M(H)$ of the particles in the simulation, in order to simulate situations in which the external magnetic fields are not strong enough to saturate the magnetic colloids. This is a typical situation in many published experimental studies of aggregation of magnetic colloids (see, for example, [23,24]), which focus on the linear magnetic response regime of the colloids.

ACKNOWLEDGMENTS

This work was supported by Spanish Government Grants No. FIS2009-13370-C02-02, No. PET2008-02-81-01, No. INNPACTO IPT-010000-2010-6, and No. CONSOLIDER-NANOSELECT-CSD2007-00041. J.F. and J.C. are also supported by Catalan Government Grant No. 2009SGR164. We would like to thank Professor D.-X. Chen (UAB) for invaluable discussions and help regarding Eqs. (13) and (14).

APPENDIX: SELECTION OF THE INTEGRATION TIME STEP

An important issue that one has to take into account when performing Brownian dynamics simulations is the proper selection of the integration time step. The typical diffusive displacement ℓ for a single colloid of diameter d and diffusion coefficient D after a time step Δt can be estimated by

$$\ell \approx \sqrt{6D\Delta t} = d\sqrt{6\Delta t/\tau}, \tag{A1}$$

where we have defined the characteristic diffusion time $\tau \equiv d^2/D$. In general, one selects a time step Δt, which results in a displacement ℓ smaller than the relevant length scales of the problem (typical separations between particles, range of interaction forces, etc.). In our model, the length scale of interactions is given by the radius of the attraction zones (see Fig. 1). The typical diffusive displacement ℓ corresponding to the selected Δt [Eq. (A1)] has to be smaller than the radius of the attraction zone r_a of the CG objects. In this way, CG objects will correctly explore the attraction zone of other surrounding CG objects. As it is shown in Fig. 1(c), the size r_a of the attraction zone depends on the chain length s (the smallest value of r_a corresponds to $s = 1$) and on the coupling parameter Γ. The dependence on Γ is strong, so one has to take into account this fact in selecting Δt.

In order to check the effect of Δt in the results of our simulations at $\Gamma = 40$ and $\Gamma = 247$, we have repeated the CG40 and CG247 simulations with three different time steps: $\Delta t = 1.00\tau$, 0.10τ, and 0.01τ. These time steps Δt correspond to typical displacements of $\ell \simeq 2.4d$, $0.8d$, and $0.24d$, respectively [see Eq. (A1)]. The results of these simulations for the average number of particles in a chain are shown in Fig. 12. As can be observed, the effects of the selection of the time step are critical for the CG40 system and irrelevant for the CG247 system. In order to understand the effect of these different Δt, one has to compare the ℓ obtained for each Δt with the values of $r_a(s = 1)$ calculated for $\Gamma = 40$ and $\Gamma = 247$ [see Fig. 1(c)]. In the CG40 simulation, the smallest radius of a CG attraction zone is $r_a(s = 1) = 1.46d$ [see Fig. 1(c), case $\Gamma = 40$], so the attraction sphere has a diameter similar to the displacement $\ell = 2.4d$ obtained for $\Delta t = 1.0\tau$. In this case, colloids cannot explore properly the attraction zones and many chain formation events are lost during the simulation run. The other two Δt give almost identical results since in both cases ℓ is smaller than $r_a(s = 1)$, and attraction zones are explored properly. In the CG247 simulations, we observe almost identical results for the three selected Δt. In this case, we have $r_a(s = 1) = 2.89d$ [see Fig. 1(c), case $\Gamma = 247$], which is larger than the corresponding typical displacements ℓ. As a general rule, if the time step selected is too large, the chains cannot properly explore the binding sites of the surrounding chains and the chaining process is not correctly simulated.

[1] S. O. Nielsen, C. F. Lopez, G. Srinivas, and M. L. Klein, J. Phys.: Condens. Matter **16**, R481 (2004).
[2] C. Hijón, P. Español, E. Vanden-Eijnden, and R. Delgado-Buscalioni, Faraday Discuss. **144**, 301 (2010).
[3] S. J. Marrink, H. J. Risselada, S. Yefimov, D. P. Tieleman, and A. H. de Vries, J. Phys. Chem. B **111**, 7812 (2007).
[4] H. J. Limbach, A. Arnold, B. A. Mann, and C. Holm, Comput. Phys. Commun. **174**, 704 (2006).
[5] E. Taboada *et al.*, Adv. Funct. Mater. **19**, 2319 (2009).
[6] C. T. Yavuz, A. Prakash, J. T. Mayo, and V. L. Colvin, Chem. Eng. Sci. **64**, 2510 (2009).
[7] J. L. Corchero and A. Villaverde, Trends Biotechnol. **27**, 468 (2009).
[8] K. M. Krishnan, IEEE Trans. Magn. **46**, 2523 (2010).
[9] D.-X. Chen, G. Via, F.-j. Xu, C. Navau, A. Sanchez, H.-C. Gu, J. S. Andreu, C. Calero, J. Camacho, and J. Faraudo, J. Appl. Phys. **110**, 073917 (2011).
[10] J. Faraudo and J. Camacho, Colloid Polym. Sci. **288**, 207 (2010).
[11] G. de las Cuevas, J. Faraudo, and J. Camacho, J. Phys. Chem. C **112**, 945 (2008).
[12] J. S. Andreu, J. Camacho, J. Faraudo, M. Benelmekki, C. Rebollo, and Ll. M. Martínez, Phys. Rev. E **84**, 021402 (2011).
[13] P. G. de Gennes and P. A. Pincus, Phys. Kondens. Materie **11**, 189 (1970).
[14] G. Helgesen, A. T. Skjeltorp, P. M. Mors, R. Botet, and R. Jullien, Phys. Rev. Lett. **61**, 1736 (1988).
[15] A. O. Ivanov, Z. Wang, and C. Holm, Phys. Rev. E **69**, 031206 (2004).
[16] P. Domínguez-García, S. Melle, J. M. Pastor, and M. A. Rubio, Phys. Rev. E **76**, 051403 (2007).
[17] J. S. Andreu, J. Camacho, and J. Faraudo, Soft Matter **7**, 2336 (2011).

[18] M. Carmen Miguel and R. Pastor-Satorras, Phys. Rev. E **59**, 826 (1999).
[19] V. Schaller, U. Kräling, C. Rusu, K. Petersson, J. Wipenmyr, A. Krozer, G. Wahnström, A. Sanz-Velasco, P. Enoksson, and C. Johansson, J. Appl. Phys. **104**, 093918 (2008).
[20] [http://www.icmab.es/softmattertheory/].
[21] J. Happel and H. Brenner, *Low Reynolds Number Hydrodynamics* (Cambridge University Press, Cambridge, England, 1985).
[22] M. Fermigier and A. P. Gast, J. Colloid Interface Sci. **154**, 522 (1992).
[23] F. Martínez-Pedrero, M. Tirado-Miranda, A. Schmitt, and J. Callejas-Fernández, Phys. Rev. E **76**, 011405 (2007).
[24] J. H. E. Promislow, A. P. Gast, and M. Fermigier, J. Chem. Phys. **102**, 5492 (1995).
[25] D. L. Ermak and J. A. McCammon, J. Chem. Phys. **69**, 1352 (1978).
[26] W. Humphrey, A. Dalke, and K. Schulten, J. Mol. Graphics **14**, 33 (1996).
[27] S. J. Plimpton, J. Comput. Phys. **117**, 1 (1995).
[28] M. M. Tirado and J. G. de la Torre, J. Chem. Phys. **71**, 2581 (1979).
[29] E. M. Furst and A. P. Gast, Phys. Rev. E **62**, 6916 (2000).
[30] M. Barrett, A. Deschner, J. P. Embs, and M. C. Rheinstädter, Soft Matter **7**, 6678 (2011).

5.3 Article 3

"Simple analytical model for the magnetic separation of superparamagnetic dispersion in a uniform magnetic eld gradient."
Jordi S. Andreu, Juan Camacho, Jordi Faraudo, Maria Benelmekki, César Rebollo and Lluís Miquel Martinez
Physical Review E **84**, 021402 (2011)

Simple analytical model for the magnetophoretic separation of superparamagnetic dispersions in a uniform magnetic gradient

J. S. Andreu,[1,2,*] J. Camacho,[2] J. Faraudo,[1] M. Benelmekki,[3] C. Rebollo,[4] and Ll. M. Martínez[5]
[1]*Institut de Ciència de Materials de Barcelona (ICMAB-CSIC), Campus UAB, E-08193 Bellaterra, Spain*
[2]*Departament de Física, Universitat Autònoma de Barcelona, Campus UAB, E-08193 Bellaterra, Spain*
[3]*Centro de Fisica, Universidade do Minho, P-4710-057 Braga, Portugal*
[4]*Sepmag Tecnologies, Parc Tecnològic del Valles, E-08290 Barcelona, Spain*
[5]*Sepmag Technologies, 191 Peachtree St. NE, Atlanta Georgia 03030, USA*
(Received 13 April 2011; revised manuscript received 27 June 2011; published 22 August 2011)

Magnetophoresis—the motion of magnetic particles under applied magnetic gradient—is a process of great interest in novel applications of magnetic nanoparticles and colloids. In general, there are two main different types of magnetophoresis processes: cooperative magnetophoresis (a fast process enhanced by particle-particle interactions) and noncooperative magnetophoresis (driven by the motion of individual particles in magnetic fields). In the case of noncooperative magnetophoresis, we have obtained a simple analytical solution which allows the prediction of the magnetophoresis kinetics from particle characterization data (size and magnetization). Our comparison with new experimental results shows good quantitative agreement. In addition, we show the existence of a universal curve onto which all experimental results should collapse after proper rescaling. The range of applicability of the analytical solution is discussed in light of the predictions of a magnetic aggregation model [Soft Matter **7**, 2336 (2011)].

DOI: 10.1103/PhysRevE.84.021402 PACS number(s): 82.70.Dd, 47.65.Cb, 85.70.Ay

I. INTRODUCTION

The manipulation of magnetic particles by the use of inhomogeneous magnetic fields (magnetophoresis) has emerged as a topic of great interest in a wide range of research and technological areas [1]. A broad spectrum of novel applications has been developed based on this concept: from environmental applications like wastewater treatments [2,3] and pollutant removal [4] to biomedical applications like protein isolation, drug delivery, magnetic hyperthermia for cancer treatment, and magnetic-particle imaging [5,6].

The particles employed in these applications are mainly superparamagnetic colloids with sizes ranging from a few nanometers to microns and with appropriate coatings, guaranteeing the stability and biocompatibility of the solutions. Superparamagnetic particles exhibit magnetizations of magnitudes similar to those of ferromagnetic materials, but they present no coercitivity nor remanence. This superparamagnetic behavior, which is of quantum origin, is limited to nanocrystals (NCs) of size below a critical size which depends on the material [7]. Larger superparamagnetic particles can be obtained as composite particles containing a nucleus of magnetic nanocrystals (typically iron oxide particles like magnetite Fe_3O_4 or its oxidized form maghemite γ-Fe_2O_3) inserted in a matrix of nonmagnetic material (such as polystyrene [8] or silica [9]). Since the superparamagnetic NCs contained inside the nucleus of the colloid are well separated, the behavior of the resulting colloid is also superparamagnetic. Thanks to this design, large magnetic moments can be obtained without losing the superparamagnetic response.

In this paper we study an issue that is common to some of the aforementioned applications of magnetic particles: the magnetic separation process. The idea behind magnetic separation is to take advantage of the distinctive magnetic response of the particles in solution to remove them from complex mixtures by the use of applied inhomogeneous magnetic fields [10]. In applications in closed containers [11,12], the inhomogeneous magnetic field is used to drive the magnetic particles toward certain regions of the containing vessel enabling the removal of the "clean" liquid phase from the solid content. Differently, in continuous flow applications, magnetic particles are typically deflected from the direction of the laminar flow by a perpendicular magnetic field gradient, depending on their magnetic susceptibility, their size, and the flow rate. This approach is common to different field-flow fractionation or split-flow thin fractionation techniques [13] integrated in microfluidic devices enabling the trapping of magnetic particles or the fractionation of magnetic particles with different magnetic response [14].

In the different applications, magnetic particles are typically functionalized with proper chemical groups, which are designed to bind to specific nonmagnetic components, thus enabling the separation of nonmagnetic materials by combining the use of magnetic particles and magnetic fields. This combination has many advantages over traditional fixed-bed separation methods, such as activated carbon adsorption for organics and affinity chromatography for proteins. In particular, the magnetic nanoparticles offer large exposed surface areas without the use of porous materials, which are often plagued by high mass-transfer resistances [15]. Therefore, it is not surprising that magnetic separation has been presented as an alternative to typical centrifugation and filtration steps in industrial processes as well as in laboratory applications.

Traditionally, the removal of magnetic particles (plus adsorbed biomaterial or pollutants) in solution is performed by the so-called high-gradient magnetic separation technique (HGMS) [11]. In an HGMS device, the dispersion containing

*jandreu@icmab.es

the magnetic nanoparticles is pumped through a column filled with a packed bed of stainless steel fibers of the order of a few microns. These fibers are responsible for the high magnetic gradients inside the column once an external magnetic field is applied. This field can be generated in several different ways: by permanent magnets [3], electromagnets [15], or superconducting solenoids [16]. The HGMS technology, initially developed for magnetic clays, has been successfully employed [15] to capture functionalized nanoparticles with sizes larger than ~10 nm.

The most important drawback present in HGMS is the loss of control over the magnetic conditions under which the magnetic particles are removed. Basically, the external magnetic field applied induces highly inhomogeneous gradients in the separator. These inhomogeneous conditions common to the HGMS approach make it difficult to develop numerical and/or analytical solutions to the problem, which would help in a better understanding of the magnetophoretic mechanisms and enhancing its performance; for instance, by means of a better design of separators or a better choice of the magnetic particles used in specific applications. So far, theoretical work has basically focused on the modeling of individual dispersed magnetic nanoparticles in an HGMS column. Most of these works have been limited to simulate the behavior of nanoparticles around a single HGMS wire [11,17–19] or, more recently, monitoring the absorbance of superparamagnetic nanoparticles under the effects of a single permanent magnet [20,21]. Unfortunately, analytical solutions for (at least approximate) predictions of these magnetophoresis processes are not known.

In previous works [12,22–24] we have made use of a new concept of magnetic separation (so-called precision magnetophoresis) to effectively remove different types of superparamagnetic nanoparticles from solution. The key aspect here is that the separation process is based on the application of a homogeneous magnetic gradient to drive the removal of the particles, enhancing the control of the experimental conditions. Also, this simpler situation seems suitable for establishing a proper framework for the development of analytical models. Herein, we fill this gap by providing an analytical solution for the kinetics of the magnetophoresis separation process. The solution obtained is valid under certain restrictive but realistic conditions, which are explicitly discussed here. We also show the utility of the analytical model by comparing our predictions with experimental results obtained with superparamagnetic particles of different sizes and magnetizations. We expect that the availability of a simple analytical model will allow for a better understanding of the underlying physics of magnetic separation processes and also allow a rational design of applications.

II. THEORY OF MAGNETOPHORESIS UNDER UNIFORM GRADIENT

First of all, let us briefly describe the magnetic separation process that is under study. We consider here the case of a radial magnetic gradient, as in the experiments reported in Refs. [12,23,24]. In these experiments, an initially homogeneous dispersion of magnetic particles is placed inside a cylindrical cavity (of radius L) containing a uniform magnetic gradient pointing toward the walls of the vessel. Due to the magnetic gradient, particles move radially, reaching the vessel wall at the end of the process. At this final stage, the remaining liquid can be removed by pumping it from the center of the vessel, if desired, and the separation process will be completed (see video in [25] for a demonstration). Our objective in this section is to obtain an analytical expression for the kinetics of this magnetic separation process, relating separation times to basic properties of the particles (such as size and magnetization).

As explained in previous works [12,23], the experimental conditions consist of a dispersion of superparamagnetic particles (nanocrystals or composites) with radius R and magnetization per unit mass $M(H)$ that are immersed in a fluid with viscosity η at temperature T. Let us assume that, under these experimental conditions, the magnetophoretic separation is driven by the motion of the individual particles under the external magnetic field. In other words, we assume that particles do not form chains induced by the dipole-dipole interaction during the magnetic separation process (see, for example, Refs. [14,15,26]). We also note here that many superparamagnetic particles are designed for use in biomedical applications [5], which strictly require no chain formation even under strong fields [magnetic resonance imaging (MRI) contrast agents or hyperthermia treatments].

Neglecting the interaction between particles, we can obtain the magnetophoretic velocity of particles by noting that the viscous drag $F_{\mathrm{vis}} = 6\pi\eta R v$ exerted by the solvent will be equal in magnitude (and opposite in direction) to the magnetic force over the particle [10,14,15,26]. Our approach follows the classical work of Senyei *et al.* [26] but, in our case, we have extended its validity to the nonlinear part of the magnetization response of the particle, contrary to what is typically required in other studies [14]. Under the effects of an external uniform magnetic gradient, the particle will experience a magnetic force F_{mag} (in our particular case, in the radial direction, pointing toward the vessel wall) given by

$$F_{\mathrm{mag}} = m\mu_0\left(\frac{\partial H}{\partial r}\right) = \frac{4}{3}\pi R^3\rho_p M(H)\mu_0\left(\frac{\partial H}{\partial r}\right), \qquad (1)$$

where ρ_p is the density of the particle, so its magnetic moment is given by $m(H) = (4/3)\pi R^3\rho_p M(H)$. Hence, in the stationary state the particles move with a velocity which depends both on the local values of the field H and its gradient:

$$v = \frac{2R^2}{9\eta}\mu_0\left(\frac{\partial H}{\partial r}\right)M(H)\rho_p. \qquad (2)$$

In order to proceed further we need to specify an analytical expression for the magnetic response $M = M(H)$ of the particles. For mathematical and conceptual simplicity, we assume that the magnetization curve $M = M(H)$ is described, to within a good approximation, by a Langevin function typical in theoretical descriptions of superparamagnetic systems [7,27–29]:

$$M(H) = M_{\mathrm{s}}\mathcal{L}[b\mu_0 H], \quad \mathcal{L}[x] = \coth x - \frac{1}{x}, \qquad (3)$$

where M_{s} denotes the saturation magnetic moment per unit mass and b^{-1} can be interpreted as a characteristic magnetic field required to reach saturation. For a superparamagnetic nanocrystal, b can be computed if M_{s} and R are known (see

Ref. [28] and our supplemental material [30]). Now we can obtain the equation of motion for the particles and study the separation process. By combining equations (2) and (3) and noting that the magnetic field is linear and radial pointing to the vessel walls [$H = (\partial H/\partial r)r$ where $\partial H/\partial r$ is constant] we obtain the following result for the velocity of a particle located at a distance r from the center of the system:

$$v(r) = v_s \mathcal{L}[\beta r/L], \tag{4}$$

where $\mathcal{L}(x)$ is the Langevin function [see Eq. (3)] and we have defined

$$v_s = \frac{2R^2}{9\eta}\mu_0 \left(\frac{\partial H}{\partial r}\right) M_s \rho_p, \tag{5}$$

$$\beta = b\mu_0 \left(\frac{\partial H}{\partial r}\right) L. \tag{6}$$

Physically, v_s is the magnetophoretic velocity of a particle with a magnetization equal to the saturation magnetization M_s. The dimensionless parameter β can be interpreted as the ratio between the magnetic field at the walls [the product $(\partial H/\partial r)L$] and the typical magnetic field [b^{-1}, see Eq. (3)] required to bring a particle to magnetic saturation. Note that, according to Eq. (4), the particles reach their maximum magnetophoretic velocities v_s at positions r verifying $\beta r/L \gg 1$. Now, we can obtain an exact, analytical expression for the separation time. Integrating Eq. (4) we obtain:

$$\frac{dr}{\mathcal{L}[\beta r/L]} = v_s dt,$$

$$\int_{r_0}^{r} \frac{dr}{\coth(\beta r/L) - \frac{L}{\beta r}} = \frac{L}{\beta}[\ln(\beta r/L \cosh(\beta r/L) - \sinh(\beta r/L))]_{r_0}^{r} = v_s t, \tag{7}$$

where r_0 is the radial coordinate of a particle at time $t = 0$ and r is its position at time t. Hence, the time t needed by a particle to reach the wall of the vessel ($r = L$) starting from an initial position $r_0 > 0$ [because the magnetic field at the center of the vessel is zero $H(0) = 0$] is

$$t = \frac{L}{\beta v_s} \ln\left[\frac{\beta\cosh(\beta) - \sinh(\beta)}{\frac{\beta r_0}{L}\cosh(\beta r_0/L) - \sinh(\beta r_0/L)}\right]. \tag{8}$$

Note that, if the particle is initially located at a position r_0 with a sufficiently high magnetic field, its magnetization is in the saturation regime ($\beta r_0/L \gg 1$) and we have $\mathcal{L}[\beta r/L] \approx 1$ and $v \approx v_s$, so that Eq. (8) reduces to $t = (L - r_0)/v_s$.

Now, from Eq. (8) is straightforward to obtain the fraction of particles remaining in dispersion inside the system at a time t. For a given time t, all particles with initial radial positions smaller than the value r_0 given by Eq. (8) will be still in solution (not at the wall). Hence, at that specific time t, the number of particles $N(t)$ remaining inside the separator is equal to the number of particles with initial radial coordinate smaller than r_0, which is proportional to πr_0^2. Therefore, the fraction $N(t)/N(0)$ of particles inside the magnetic separator is given by

$$f \equiv \frac{N(t)}{N(0)} = \left(\frac{r_0}{L}\right)^2. \tag{9}$$

Using Eqs. (8) and (9) we obtain the separation time t at which a given fraction of particles f is still in dispersion (not at the walls):

$$t = \frac{L}{\beta v_s} \ln\left[\frac{\beta\cosh(\beta) - \sinh(\beta)}{\beta\sqrt{f}\cosh(\beta\sqrt{f}) - \sinh(\beta\sqrt{f})}\right]. \tag{10}$$

In other words, Eq. (10) gives the time t needed to reach the state with a fraction of particles f still in solution. Note that, in the limiting case of $\beta \gg 1$ and $\beta\sqrt{f} \gg 1$, Eq. (10) reduces to

$$f \approx \left(1 - \frac{v_s}{L}t\right)^2. \tag{11}$$

In practice, β is typically between 10 and 100 (see next section), so Eq. (11) can usually be employed to estimate the initial kinetics of the separation process. Physically, Eq. (11) describes the separation process assuming that the magnetization of particles is at saturation, whereas Eq. (10) takes into account the full $M(H)$ dependence.

At this point, it is important to explicitly discuss under which conditions this requirement of no chain formation under a magnetic field is fulfilled. The classical criterion against chain formation induced by the dipole-dipole interaction derived in the context of ferrofluids (see, for example, p. 37 in Ref. [28]) requires that the magnetic coupling constant, defined as

$$\Gamma = \frac{\mu_0 m_s^2}{2\pi d^3 k_B T}, \tag{12}$$

verifies $\Gamma \ll 1$. In Eq. (12) m_s is the magnetic moment of a particle at saturation and d is its diameter. Physically, Γ is the ratio between the magnetic energy associated to the dipole-dipole attraction (which tends to induce the formation of chains of particles in the dipole direction) and the thermal energy (which tends to disaggregate). However, our recent simulation results show that this classical criterion is not fulfilled in dispersions of superparamagnetic particles. For example, we have shown that, for $\Gamma = 3$ and a volume fraction $\phi_0 = 5.23 \times 10^{-4}$, no aggregation is found (see Fig. 2 Ref. [31]), in disagreement with the classical criterion. In general, our simulations have shown that the aggregation behavior depends both on Γ and the volume fraction ϕ_0 (defined as the volume fraction of particles uniformly dispersed in solution before applying the magnetic field). Combining simulation results with a thermodynamical model [31] we have shown that the aggregation behavior of superparamagnetic dispersions is controlled by the dimensionless parameter N^* given by

$$N^* = \sqrt{\phi_0 e^{\Gamma - 1}}. \tag{13}$$

As shown in Ref. [31], in order to observe aggregation, the condition $N^* > 1$ should be verified. In this case, the number density of chains of length s follows

$$n_s \propto e^{-s/N^*}. \tag{14}$$

and the average length of chains is thus $\bar{n} \approx N^*$. For more details and a comparison with simulations, see Ref. [31]. Our results also agree with recent small angle neutron scattering results [32]. Typical values of Γ and N^* of superparamagnetic colloids employed in the laboratory will be discussed in detail

in the next section. Here it is enough to remark that all analytical results derived in this section are valid under the condition $N^* < 1$.

Another issue to be considered in applying our theoretical model is the possible effect of sedimentation due to gravity. In principle, sedimentation will be irrelevant in the separation process if the vertical distance sedimented during magnetophoresis is smaller than the vertical size of the system. In our experimental situations, we will have always a sedimentation velocity much smaller than magnetophoresis velocity; in addition, the radius is much smaller than the height of the container.

III. USE OF ANALYTICAL MODEL IN ANALYSIS OF MAGNETOPHORESIS EXPERIMENTS

A. Comparison of predictions with experiments

Now we will explore the use of the analytical results obtained in the previous section to understand the kinetics of actual magnetophoresis separation experiments. In particular, we will show the usefulness of Eq. (10) in predicting magnetophoresis kinetics in the case $N^* < 1$. We will also discuss the limitations of our analytical model by briefly discussing the case $N^* > 1$, for which no analytical solution is yet available.

For the sake of concreteness, we will consider results for dispersions of 4 different samples of superparamagnetic particles (see Table I), differing in size and composition but all of them representative of the many different kinds of particles employed in biotechnological applications. Further technical details (synthesis, characterization) are given in the supplemental material or in the indicated references. In all cases, our magnetophoretic separation experiments were performed using precision magnetophoresis systems from SEPMAG [33], the SEPMAG LAB 1×25 ml 2042 and 2042 plus (in both cases, $L = 1.5$ cm). The magnetophoresis kinetics is monitored by measuring the opacity of the sample, as in previous works [12,23,24] (we also describe again the full experimental methodology in the accompanying supplemental material). Here it suffices to say that the measured opacity (after appropriate normalization) provides a good estimate of the fraction f of particles remaining in solution.

Let us first consider sample S1, which consists of maghemite γ-Fe_2O_3 nanocrystals about 12 nm in size dispersed in water at a 10 g/L concentration. It is known that the colloidal stability (in the absence of a magnetic field) of these small nanocrystals in dispersions could be an issue. In our case, we ensure the stability by electrostatic stabilization.

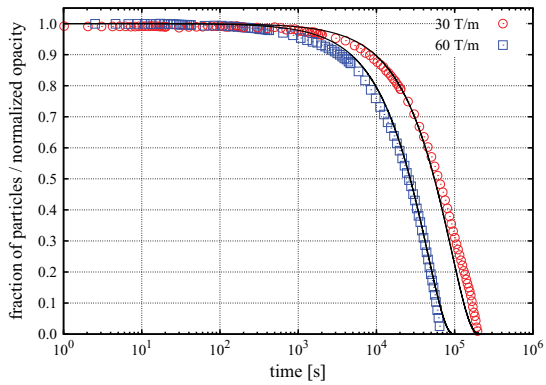

FIG. 1. (Color online) Kinetics of magnetophoretic separation of a 10 g/L dispersion of superparamagnetic γ-Fe_2O_3 nanocrystals (sample S1). Solid lines are the predictions of Eq. (10) (with no free parameters) and symbols are the experimental results under 30 T/m (circles) and 60 T/m (squares).

For full details of sample preparation, stabilization, and characterization, see the supplemental material. As shown in Table I, $N^* < 1$, so Eq. (10) applies in this case. The values of the required quantities v_s and β were computed by using the data in Table I in Eqs. (5) and (6). For example, under a 60 T/m gradient we obtain $v_s = 1.59 \times 10^{-7}$ m/s and $\beta = 61.7$. In Fig. 1 we show the theoretical predictions and the experimental results for two different magnetic gradients (30 and 60 T/m). Our results (see Fig. 1) show that Eq. (10) can be successfully applied to predict the magnetophoretic behavior from averaged properties of the sample, such as particle radius R and saturation dipole m_s. Of course, in real samples there are always factors difficult to control (such as a certain degree of polydispersity differing from batch to batch of identically produced particles) which may cause deviations from the ideal behavior predicted by Eq. (10). Also, the measurement of the full magnetophoresis curve is particularly challenging since, in some cases, it requires more than one day to complete and additional spurious effects (such as changes of viscosity of water due to temperature variations during the experiment) may reduce the agreement between theory and experiment. In spite of these limitations, the agreement between theory and experiment is rather satisfactory for this sample. For example, at a field gradient of 60 T/m we predict that half of the dispersion ($f = 0.5$) is removed at separation times of 7.5 h, close to the experimental value of 7 h.

TABLE I. Physical parameters for the different particles employed in the magnetophoretic experiments shown in Figs. 1 and 2: $2R$ is the diameter, ρ_p is the density, m_s is the magnetic dipole at saturation, and the quantities b, Γ, and N^* are defined in Eqs. (1), (12), and (13), respectively.

Sample	$2R$ [nm]	ρ_p [g/cm^3]	m_s [J/T]	b [T^{-1}]	Γ	N^*
S1 (γ-Fe_2O_3)	12	4.86	3.0×10^{-19}	68	2.5	0.1
S2 Core (γ-Fe_2O_3)/Shell (SiO_2)	82	2.40	3.0×10^{-18}	9.3	0.8	0.02
S3 Core (γ-Fe_2O_3)/Shell (SiO_2)	157	2.35	1.7×10^{-17}	13.8	3.5	0.2
Estapor® M1-020/50	200	1.10	2.5×10^{-16}	N/A	$\sim 10^3$	$\sim 10^{21}$

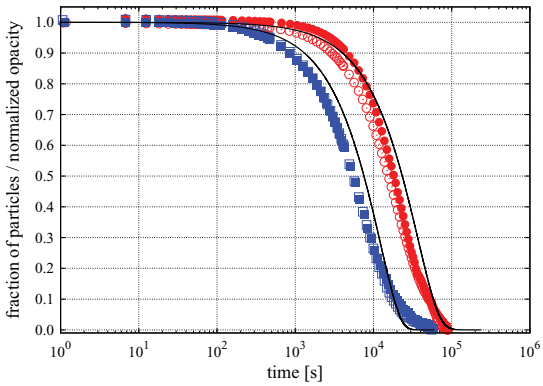

FIG. 2. (Color online) Comparison of magnetophoretic separation kinetics of colloidal dispersions containing different composite superparamagnetic particles obtained in experiments (symbols) with the predictions of Eq. (10) (solid line) without adjustable parameters. Circles correspond to sample S2 and squares to sample S3 with a magnetic gradient of 60 T/m (open and filled symbols correspond to different repetitions of the same experiment).

Now let us consider the results for a different kind of superparamagnetic particles. Samples S2 and S3 correspond to a dispersion in water of core shell composite particles described in Ref. [9] (also denoted by samples S2 and S3 in that reference) which were designed as image contrast agents in MRI. In these composite nanoparticles, the shell is made of microporous silica and the core contains several 6.5 nm γ-Fe_2O_3 nanocrystals previously synthesized in Ref. [34]. The average size of the composite particles is 82 nm in the case of S2 and 157 nm in the case of S3, as determined by transmission electron microscopy (TEM) (although there is some polydispersity in size, as discussed in Ref. [9]). In this case, the dispersions had a concentration of 1 g/L and $N^* < 1$ so Eq. (10) is expected to apply. It should be noted that, in applications, these particles need to be employed always under conditions with $N^* < 1$ to avoid magnetic aggregation and allow their use as image contrast agents.

In Fig. 2 we show the results under a gradient of 60 T/m. The values for the saturation velocity v_s and dimensionless parameter β, computed by using the data in Table I in Eqs. (5) and (6), are $v_s = 2.19 \times 10^{-7}$ m/s and $\beta = 9.5$ for S2 and $v_s = 6.46 \times 10^{-7}$ m/s and $\beta = 14.1$ for S3. Again, Eq. (10) can be applied to predict, with reasonable approximation, the magnetophoretic behavior from average particle data. For example, predicted times for $f = 0.5$ are 6 hours (sample S2) and 2 hours (sample S3), which are reasonably close to the experimental values of 4.3 hours and 1.5 hours, respectively.

We note here that the agreement between theory and experiments for S2 and S3 is less satisfactory than that observed for S1 (compare Fig. 1 with Fig. 2). This could be attributed to the fact that the fit of the magnetic response of samples S2 and S3 to the Langevin function Eq. (3) is less accurate than in the case of sample S1 (see the supplemental material for details on the magnetic characterization of the samples). We expect that the agreement could be further improved by using more sophisticated functions to model the $M(H)$ response (such as those proposed in Ref. [29]). However, this better fit of the $M(H)$ response will make it impossible to obtain an analytical solution for f. Here we prefer to maintain the model as simple as possible, even at the cost of losing some accuracy in the results (which is in fact not essential in practice).

Up to now, we have discussed the case of magnetophoresis due to single-particle motion ($N^* < 1$), which is a situation in which our analytical model holds. It is reasonable to expect that, in the case $N^* > 1$ (formation of chains of magnetic particles induced by the external field), the observed magnetophoresis kinetics will be faster than expected from our analytical calculations. However, it is not obvious how large the difference between the single-particle kinetics described by our model and cooperative kinetics will be. To this end, we also include a comparison with experimental results, obtained in our previous study [12], with commercial Estapor$^{(R)}$ M1-020/50 particles, which correspond to extremely large N^* (see Table I). These commercially available particles are made of magnetic nanocrystals embedded in a polystyrene matrix and are employed in immunoassay applications (in these applications, reversible magnetic aggregation under applied field is often a desired effect). An example of the experimental results obtained in Ref. [12] are shown in Fig. 3. These results correspond to a solution of 1 g/L concentration under a 30 T/m gradient. The kinetics of single-particle magnetophoresis was estimated using $v_s \simeq 4 \times 10^{-6}$ m/s (as calculated from the data in Table I). Since we do not pretend in this case to provide an accurate prediction, we employ, for simplicity, Eq. (11) for f, which assumes that individual particles always move with their maximum possible velocity v_s, which corresponds to the saturation magnetization. It is clear that the kinetics observed for Estapor$^{(R)}$ M1-020/50 particles is orders of magnitude faster than the kinetics expected from the v_s value for these particles. In fact, the magnetophoretic process is very fast and complete separation is obtained in less than 2 minutes.

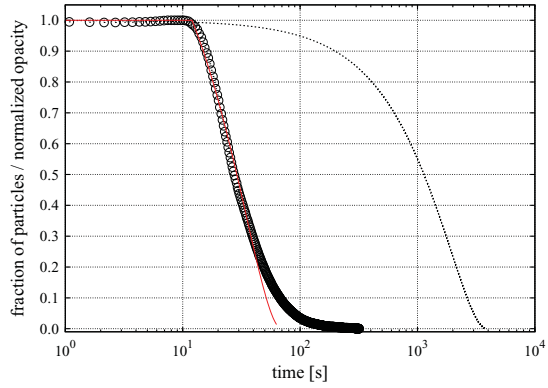

FIG. 3. (Color online) Comparison between cooperative magnetophoresis observed with commercial Estapor$^{(R)}$ M1-020/50 particles (symbols) and the single-particle magnetophoresis kinetics ($N^* < 1$) ideally expected by these particles moving at their maximum velocity v_s, according to Eq. (11) (dashed line). The solid line is a fit of the initial decay to Eq. (11) leaving the magnetophoretic velocity as a fitting parameter, which gives $v_s^{agg} \approx 2.6 \times 10^{-4}$ m/s.

Hence, the comparison shown in Fig. 3 is consistent with the existence of a cooperative process in the experiments, as we proposed originally in Ref. [12]. In that reference, the observed fast kinetics was attributed to the formation of elongated aggregates. In fact, the results of Fig. 3 can be employed to obtain a crude estimate of the velocity and size of these aggregates. The velocity of the aggregates can be estimated as follows: We interpret the experimental data in Fig. 3 as corresponding to an initial regime (for times up to 12 s) in which aggregates are formed and $f \approx 1$ followed by magnetophoresis kinetics obeying Eq. (11) with a certain velocity for the aggregates v_s^{agg}. Fitting the experimental data for t up to 100 s (see fit in Fig. 3), we obtain $v_s^{agg} \approx 2.6 \times 10^{-4}$ m/s; that is, we estimate that aggregates move 65 times faster than individual particles. If we approximate the aggregates as ellipsoids of semiaxis aR and cR ($a \geqslant c$), it is easy to show that the magnetophoretic velocity of the ellipsoid at magnetic saturation is given by $v_s^{agg} = [ac^2/C_D(a,c)]v_s$, where v_s is the velocity of a single particle [as given by Eq. (5)] and $C_D(a,c)$ is the drag coefficient given by [35] ($\delta^2 \equiv a^2 - c^2$)

$$C_D = \frac{8}{3}\left[\frac{1}{\delta}\ln\left(\frac{a+\delta}{a-\delta}\right) - \frac{2a^2}{\delta^3}\left(\frac{\delta}{a} - \operatorname{arcsinh}(\delta/c)\right)\right]^{-1}. \tag{15}$$

Hence, our previous estimate of $v_s^{agg} \approx 65 v_s$ is consistent with ellipsoidal aggregates of different dimensions. We provide just two examples: ellipsoids with semiaxes $a \approx 11.5$, $c \approx 4.7$ and $a \approx 32$, $c \approx 4.6$. The first one would contain around 250 particles and the second one about 700 particles. This indicates that aggregates in the cooperative magnetophoresis process may contain several hundred particles, a situation quite different from the one studied here (and the subject of future work).

We can conclude this subsection by saying that the results presented here support the view proposed in the previous section that two very different magnetophoresis processes are possible under a constant magnetic gradient. Single particle magnetophoresis (described by our analytical model) is observed for $N^* < 1$ whereas cooperative magnetophoresis (involving the formation of large elongated aggregates of particles induced by the magnetic field) is observed for $N^* \gg 1$.

B. Possibility of a universal curve

Interestingly, our theoretical results imply that all experimental magnetophoretic results obtained for $N^* < 1$ should collapse onto a unique, universal curve after properly rescaling quantities. In fact, by defining a dimensionless time $\tau \equiv t v_s/L$ and function $J(x) \equiv \ln(x\cosh(x) - \sinh(x))$, expression (10) becomes

$$\tau = \frac{1}{\beta}[J(\beta) - J(\beta f^{1/2})]. \tag{16}$$

Therefore, one obtains that τ is a function of f and is dependent on the specific magnetophoretic system through the dimensionless parameter β defined in Eq. (6). One can invert this function to get the fraction of particles in solution f in terms of the dimensionless time τ and parameter β. A direct manipulation of Eq. (16) yields

$$\beta^2 f = g\,(J(\beta) - \beta\tau)\,, \tag{17}$$

where $g(x) \equiv [J^{-1}(x)]^2$ and $J^{-1}(x)$ is the inverse of function $J(x)$. Equation (17) shows that the rescaled fraction of particles $\beta^2 f$ is a universal function g of a rescaled time defined as $J(\beta) - \beta\tau$.

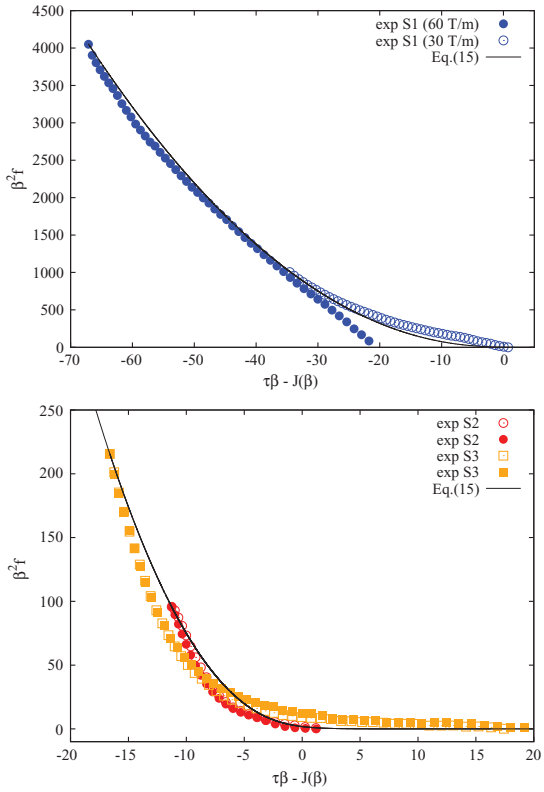

FIG. 4. (Color online) Comparison of theoretical predictions for a universal kinetic curve [Eq. (17), solid line] with experimental results (symbols). Top panel shows a comparison using experimental data for γ-Fe_2O_3 nanocrystals (sample S1) under 30 T/m (open symbols) and 60 T/m (filled symbols). Bottom panel shows a comparison using experimental results for composite particles. Circles correspond to sample S2 and squares to sample S3 (open and filled symbols correspond to different repetitions of the same experiment).

In Fig. 4 we show a plot of this universal curve compared with the experimental results for samples S1 (under two different gradients of 30 and 60 T/m) and samples S2 and S3 (under 60 T/m). These systems correspond to very different values for the scaled quantities, so we prefer to show the results in two different panels for easier visibility. The results for sample S1 (Fig. 4, top panel) show, in general, good agreement with the theoretical predictions, although deviations are found at small opacities, where measurements have less accuracy. For samples of composite particles (S2 and S3, Fig. 4, bottom panel), the agreement is satisfactory.

IV. CONCLUSIONS

In this paper, we have analyzed magnetophoretic separation of superparamagnetic particles of different types under well-controlled magnetophoretic conditions (in a system based on a radial, uniform magnetic gradient). Depending on the properties of the particles and the dispersion, we have proposed two different kinetic regimes for magnetophoretic separation, characterized by a dimensionless quantity denoted as N^* [see Eq. (13)]. For $N^* < 1$, the kinetics of the magnetophoresis process is dominated by the motion of single particles in a magnetic gradient (noncooperative magnetophoresis) and, consequently, the time scales for magnetic separation are large (many hours in the experiments performed here). In this case, it is possible to obtain an analytical solution for the kinetics of the magnetophoresis process with no free parameters and which shows a satisfactory agreement with experimental results. Our analytical results also show the existence of a universal curve [see Eq. (17) and Fig. 4], onto which all experimental results should collapse after proper scaling (provided that they correspond to the noncooperative regime, $N^* < 1$).

In the case of large N^* (which corresponds to particles with high magnetic dipole and moderate or large concentrations), the magnetophoresis process is enhanced by the formation of long chains of particles which move rapidly in the magnetic gradient. This cooperative magnetophoresis process (described in our previous work [12]) is characterized by a kinetics orders of magnitude faster than that expected from the single-particle model. No analytical models are available for this case yet, so this important case will be the subject of further work.

It is also interesting to note that we have focused here on the prediction of the magnetophoresis behavior of particles with known magnetic properties [i.e., a well-characterized $M(H)$ curve]. However, in some practical applications it could be of interest to obtain an estimation of the $M(H)$ curve as a byproduct of a magnetophoresis process by fitting the obtained kinetics with our analytical results: Eqs. (5), (6), and (10) (provided that $N^* < 1$).

Finally, as a limitation of our model, we note that polydispersity effects are not taken into account. Although synthesis methods are advancing rapidly and provide very monodisperse particles, some polydispersity is still possible. However, it is difficult to include this effect rigorously in an analytical model. An important difficulty is the lack of analytical knowledge of the distributions of sizes and magnetizations in real samples. In any case, our comparisons with experimental results shows that the assumption of a mean size for the particles is a good first-order approximation.

ACKNOWLEDGMENTS

This work is supported by the Spanish Government Grants No. FIS2009-13370-C02-02, No. PET2008-02-81-01/02, No. INNPACTO IPT-010000-2010-6, and No. CONSOLIDER-NANOSELECT-CSD2007-00041. J.F. and J.C. are also supported by the Catalan Government Grant No. 2009SGR164. We thank Anna Roig and Elena Taboada (ICMAB-CSIC) for kindly supplying us samples S2 and S3 and their characterization data, as well as for extensive discussions.

[1] C. T. Yavuz, A. Prakash, J. T. Mayo, and V. L. Colvin, Chem. Eng. Sci. **64**, 2510 (2009).
[2] C. De Latour, IEEE Trans. Magn. **9**, 314 (1973).
[3] G. Mariani, M. Fabbri, F. Negrini, and P. L. Ribani, Sep. Purif. Technol. **72**, 147 (2010).
[4] C. T. Yavuz, Science **314**, 964 (2006).
[5] J. L. Corchero and A. Villaverde, Trends Biotechnol. **27**, 468 (2009).
[6] K. M. Krishnan, IEEE Trans. Magn. **46**, 2523 (2010).
[7] C. P. Bean and J. D. Livingstone, J. Appl. Phys. **30**, 120S (1959).
[8] D. Leun and A. K. Sengupta, Environ. Sci. Technol. **34**, 3276 (2000).
[9] E. Taboada, R. Solanas, E. Rodríguez, R. Weissleder, and A. Roig, Adv. Funct. Mater. **19**, 2319 (2009).
[10] G. Friedman and B. Yellen, Curr. Opin. Colloid Interface Sci. **10**, 158 (2005).
[11] R. Gerber, M. Takayasu, and F. J. Friedlaender, IEEE Trans. Magn. **19**, 2115 (1983).
[12] G. de las Cuevas, J. Faraudo, and J. Camacho, J. Phys. Chem. C **112**, 945 (2008).
[13] N. Pamme and A. Manz, Anal. Chem. **76**, 7250 (2004).
[14] H. Watarai, M. Suwa, and Y. Iiguni, Anal. Bioanal. Chem. **378**, 1693 (2004).
[15] G. D. Moeser, K. A. Roach, W. H. Green, T. A. Hatton, and P. E. Laibinis, AIChE J. **50**, 2835 (2004).
[16] S. K. Baik, D. W. Ha, R. K. Ko, and J. M. Kwon, Physica C **470**, 1831 (2010).
[17] M. Takayasu, R. Gerber, and F. J. Friedlaender, IEEE Trans. Magn. **19**, 2112 (1983).
[18] L. P. Davies and R. Gerber, IEEE Trans. Magn. **26**, 1867 (1990).
[19] T. Y. Ying, S. Yiacoumi, and C. Tsouris, Chem. Eng. Sci. **55**, 1101 (2000).
[20] V. Schaller *et al.*, J. Appl. Phys. **104**, 093918 (2008).
[21] L. E. Helseth and T. Skodvin, Meas. Sci. Technol. **20**, 095202 (2009).
[22] J. Faraudo and J. Camacho, Colloid Polym. Sci. **288**, 207 (2010).
[23] M. Benelmekki, C. Caparros, A. Montras, R. Goncalves, S. Lanceros-Mendez, and Ll. M. Martínez, J. Nanopart. Res. **13**, 3199 (2010).
[24] M. Benelmekki, A. Montras, A. J. Martins, P. J. G. Coutinho, and Ll. M. Martínez, J. Magn. Magn. Mater. **323**, 1945 (2011).
[25] See video at [http://www.youtube.com/watch?v=BVipEdKoMh8].
[26] A. Senyei, K. Widder, and G. Czerlinski, J. Appl. Phys. **49**, 3578 (1978).
[27] R. Kaiser and G. Miskolczy, J. Apply. Phys. **41**, 1064 (1970).
[28] R. E Rosensweig, *Ferrohydrodynamics*, 1st ed. (Cambridge University Press, New York, 1985).

[29] D. X. Chen, A. Sanchez, E. Taboada, A. Roig, N. Sun, and H. C. Gu, J. Appl. Phys. **105**, 083924 (2009).

[30] See Supplemental Material at http://link.aps.org/supplemental/10.1103/PhysRevE.84.021402 for details on the synthesis of sample S1, the magnetic characterization of all samples, and a description of the magnetophoretic measurements.

[31] J. S. Andreu, J. Camacho, and J. Faraudo, Soft Matter **7**, 2336 (2011).

[32] M. Barrett, A. Deschner, J. P. Embs, and M. C. Rheinstädter, Soft Matter **7**, 6678 (2011).

[33] SEPMAG Tecnologies [http://www.sepmag.eu].

[34] E. Taboada, E. Rodríguez, A. Roig, J. Oró, A. Roch, and R. N. Muller, Langmuir **23**, 4583 (2007).

[35] H. Lamb, *Hydrodynamics*, 6th ed. (Cambridge University Press, Cambridge, 1993).

Supporting Information for the article "A simple analytical model for the magnetophoretic separation of Superparamagnetic dispersions in a uniform magnetic gradient."

J. S. Andreu,[1,2,*] J. Camacho,[2] J. Faraudo,[1] M. Benelmekki,[3,†] C. Rebollo,[4] and Ll. M. Martínez[5]

[1]*Institut de Ciència de Materials de Barcelona (ICMAB-CSIC), Campus UAB, E-08193 Bellaterra, Spain.*
[2]*Departament de Física, Universitat Autònoma de Barcelona, Campus UAB, E-08193 Bellaterra, Spain.*
[3]*Centro de Fisica, Universidade do Minho, 4710-057 Braga, Portugal.*
[4]*Sepmag Tecnologies, Parc Tecnològic del Valles, E-08290 Barcelona, Spain.*
[5]*Sepmag Technologies, 191 Peachtree St. NE, 03030 Atlanta. GA, USA.*

(Dated: July 19, 2011)

I. SUPPLEMENTARY INFORMATION FOR SAMPLE S1

A. Synthesis of γ-Fe_2O_3 nanocrystals

The maghemite nanoparticles (γ-Fe_2O_3) were prepared by co-precipitation from an aqueous mixture of $FeSO_4$ and $FeCl_3$ (1:2 molar ratio). NH_4OH was used as a precipitation agent [1]. The as precipitated and dried nanoparticles were stabilized by using 2 g/l of SDS (Sodium Dodecyl Sulphate) aqueous solution. This concentration corresponds to 0.838 times the SDS critical micelle concentration (CMC) in solution without particles [2]. A 1 g of the as precipitated and dried Fe_2O_3 nanoparticles was dispersed in 50 ml of the prepared SDS aqueous solution followed by vigorous stirring for 2 hours. The pH was maintained at 10 to assure a stable suspension. The suspension was washed with distilled water for several times to remove the excess of SDS. Finally the obtained NCs were dried and a suspension of 10 g/cm^3 aqueous solution of the SDS-modified NCs was prepared.

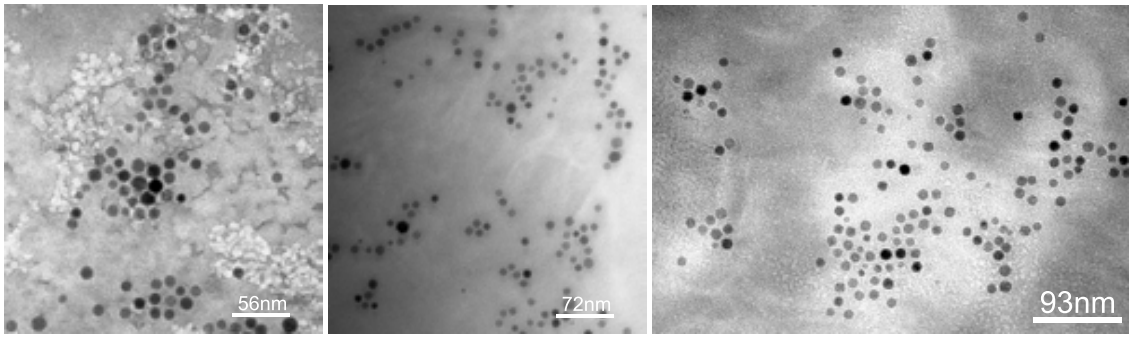

FIG. 1: TEM images of the superparamagnetic nanocrystals (sample S1) synthesized in this work.

A LEO 906E electron microscope operating at 100 KeV, was used for transmission electron microscopy (TEM) characterization (see fig. 1). The samples were prepared by deposition of a droplet of particles solution on a copper grid coated with carbon and allowed to dry. The particle size estimated was 10 ± 3 nm.

*Electronic address: jandreu@icmab.es
†Electronic address: benelmekki@fisica.uminho.pt

B. Stabilization of colloidal suspensions of γ-Fe_2O_3 nanocrystals

In general, it is not easy to find in colloidal suspensions in water, isolated γ-Fe_2O_3 nanocrystals but they tend to form clusters of about 100-150 nm in size. In order to avoid this agglomeration phenomena, a careful colloidal stabilization of the particles against Van der Waals forces is required. In general, two strategies can be used to stabilize small nanoparticles and colloidal particles [3, 4] by adding repulsive interactions: steric stabilization and electrostatic stabilization. Steric stabilization is acommplished by adding capping molecules at the surface of the particle. Electrostatic stabilization is obtained by charging the particles in solution. In this case, our γ-Fe_2O_3 nanocrystals are covered by SDS anionic molecules (a widely employed surfactant, which is negativelly charged in water), see Figure 2. This electrostatic stabilization has been characterized by ζ potential measurements using a Zetasizer Nano ZS (Malvern Instruments Ltd). As expected, we obtained a high (and negative) electrophoretic mobility of -3.5×10^{-8} $m^2/V \cdot s$. After three repetitions of the experiment, the instrument quoted an average ζ potential (estimated using the Smoluchowski equation) of -43.7 mV, enough to ensure electrostatic stability of the particles [3, 4] . Using the same instrument but in the DLS mode, we checked that the size of the dispersed objects remained consistent with the particle size previously measured by TEM imaging. In addition, we also expect some further repulsive (stabilizing) contribution from the steric interactions due to the presence of the SDS molecules at the surface of the nanoparticles.

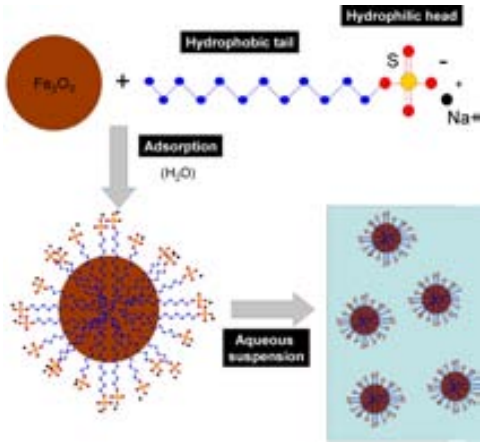

FIG. 2: Cartoon illustrating the stabilization of γ-Fe_2O_3 nanocrystals. Anionic surfactant SDS molecules are adsorbed onto the surface of the nanocrystals providing a negative charge in water. Therefore, the nanocrystals in solution repel one each other electrostatically giving raise to a stable colloidal suspension.

C. Magnetic Characterization

The magnetic response for sample S1 was characterized by a Quantum Design MPMS-XL-7T SQUID magnetometer at ICMAB. The applied magnetic field was in the range ±5 T at room temperature (298K). The measurements were performed using a dry sample of known mass of the γ-Fe_2O_3 nanocrystals (our magnetometer does not allow for direct measurements of liquid dispersions). In Figure 3 we show the results for fields up to 1 T, which is the range of magnetic fields of interest in our magnetophoresis experiments. The sample shows superparamagnetic behaviour, so we decided to fit the experimental $M(H)$ curves with a Langevin function typical in theoretical descriptions of superparamagnetic systems[5–7]:

$$M(H) = M_s \mathcal{L}[b\mu_0 H], \qquad \mathcal{L}[x] = \coth x - \frac{1}{x}. \tag{1}$$

In Eq.(1), M_s denotes the saturation magnetic moment per unit mass of the sample, and b^{-1} can be interpreted as a characteristic magnetic field required for the sample to reach saturation. According to the *macro-spin approximation*,

the two parameters M_s and b are not independent and are related by:

$$b = \frac{m_s}{k_B T} = \frac{4\pi R^3 M_s \rho_p}{3 k_B T}, \tag{2}$$

where m_s is the magnetic dipole of the nanoparticles at saturation, R is their radius and ρ_p is their density. Due to the uncertainities inherent to the determination of R and ρ_p, we have decided to fit the $M(H)$ curve with Eq.(1) using M_s and b as independent parameters, and then determine the size of the γ-Fe_2O_3 nanocrystals from Eq.(2). In this case we have obtained as a best fit the values $M_s = 68.00 \pm 0.09$ emu/g and $b = 68 \pm 1$ T^{-1} (see Figure 3). For a typical particle density for the γ-Fe_2O_3 phase of 4.86 g/cm^3, we obtain for an estimation of the magnetic moment at saturation of the nanocrystals $m_s = 3.0 \times 10^{-19}$ J/T.

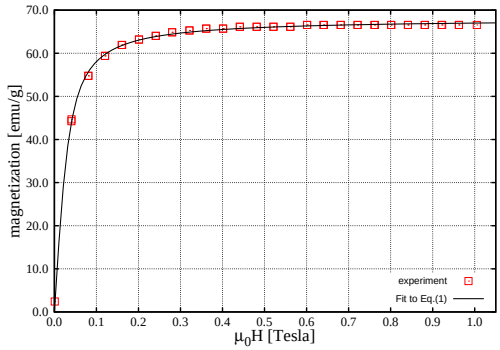

FIG. 3: Magnetization curve for the γ-Fe_2O_3 nanocrystals (S1) from SQUID measurements. The solid line is the Langevin function obtained from fitting the experimental data to Eq.(1). The selected fitting interval ($\mu_0 H = (0, 1]$ T) has been selected to achieve the best accuracy according to the maximum field applied in our experimental setup.

Now, since we have determined b and M_s as independent parameters from the $M(H)$ curve, we can employ Eq.(2) to calculate the radius R, which is given by:

$$R = \left(\frac{3 b k_B T}{4\pi M_s \rho_p} \right)^{1/3}. \tag{3}$$

Assuming again that the density of the nanocrystals is $\rho_p(\gamma\text{-}Fe_2O_3)$=4.86 g/cm^3, we obtain $2R \sim 12$ nm, consistent with the size determined by TEM.

II. MAGNETIC CHARACTERIZATION OF SUPERPARAMAGNETIC COMPOSITES: S2 AND S3 SAMPLES

In this case, the $M(H)$ curves were kindly provided to us by Anna Roig and Elena Taboada (ICMAB-CSIC) and are shown in figure 4 (see Ref[8] for details about the measurements). Here, we have analyzed these $M(H)$ curves employing the same approach used in the previous section, i.e. we have fitted the experimental data to Eq.(1) using two free parameters, M_s and b. The results of the fit are shown in figure 4 and table I. In order to calculate the magnetic moment at saturation, $m_s = (4/3)\pi R^3 M_s \rho_p$, we need to estimate the density ρ_p of a composite particle. Following the methodology and values in ref. [8] we have calculated the particle density according to the following expression:

$$\rho_p = \rho_{shell} \times x_{shell} + \rho_{core} \times x_{core} \tag{4}$$

where x_{shell} and x_{core} are the weight fraction of the shell and the core of the composite particle, respectively. Using the values in reference [8] (a density of 2.2 g/cm^3 for the silica shell and the reported weight fraction of iron oxide content in each sample (i.e. 0.070 for sample S2 and 0.059 for sample S3), we obtain a particle density of 2.40 g/cm^3 and 2.35 g/cm^3 for samples S2 and S3, respectively. The resulting values for m_s are given in Table I.

As a final remark, it should be noted that equation 2 relating the parameters M_s and b with the radius R does not hold for composite nanoparticles, although generalizations are possible. These generalizations allow the calculation of the size of the magnetic nanocrystals embedded in the composite particles from magnetic characterization data. The interested reader is referred to Ref.[7] for details.

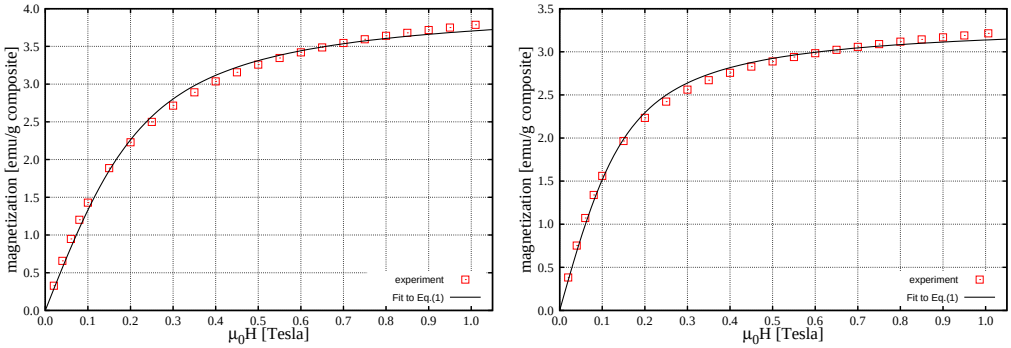

FIG. 4: Magnetization curves from SQUID measurements corresponding to composite nanoparticles, sample S2 (left) and sample S3 (right). The solid line is the Langevin function obtained from fitting the experimental data to Eq.(1) in the interval $\mu_0 H = (0, 1]$ T. We notice here that the behavior exhibited by these composite particles resembles those found in ref.[9].

TABLE I: Values obtained from fitting the experimental results to a simple 2-parameters Langevin function corresponding to the composite particles. We also present here the (Volume) magnetization and the estimation of the magnetic moment for these samples.

sample	M_s	$M_s\rho_p$	b	m_s
[-]	[emu/g]	[A/m]	[T^{-1}]	[J/T]
S2	4.27 ± 0.04	1.034×10^4	9.3 ± 0.3	2.82×10^{-18}
S3	3.49 ± 0.03	0.831×10^3	13.8 ± 0.6	1.59×10^{-17}

III. METHODS FOR THE MAGNETOPHORETIC SEPARATION MEASUREMENTS

Our magnetophoretic separation experiments have been performed using precision magnetophoresis systems from SEPMAG [10], the SEPMAG LAB 1×25ml 2042 and 2042 plus. These systems consists of a cylindrical cavity containing a high permanent magnetic field with a uniform gradient pointing towards the walls of the cylindrical vessel (see fig. 5).

The magnetophoresis experiments are performed by placing a bottle of radius L =1.5 cm containing 25 ml of aqueous solution inside the SEPMAG cylindrical cavity. Laboratory temperature during all measurements was 293 ± 5K. In a successful magnetophoresis experiment, the initially opaque dispersion becomes more transparent as time goes on, eventually reaching a transparent final state with all particles close to the walls of the bottle (see Figure 5). At the end of the process, the "clean" solution can be removed by extracting the solvent from the central region of the vessel, so the magnetophoresis process can be applied as a separation technique (see video in [11] for a demonstration). The magnetophoresis process is monitored though opacity measurements as in previous works [1, 12]. The dispersion is illuminated from below and a photoresistance (LDR) placed on top quantifies the relative transmitted light through the sample during the experiment. The voltage $V(t)$ measured in the LDR is converted into a normalized opacity by the relation opacity(t)= $(V(t) - V_f)/(V(0) - V_f)$, where $V(0)$ is the voltage measured at $t = 0$ and V_f the value measured at the end of the process, which corresponds to the maximum transparency of the sample (see fig. 5). In this way, a opacity of 1 corresponds to the initial dispersion and 0 corresponds to a final state with all particles at the walls of the container (no dispersed particles). Absolute values of the voltage excursion due to opacity changes are typically of tens of milivolts. The measurements were done with a $6\frac{1}{2}$ digits multimeter (Keithley 2000) and the

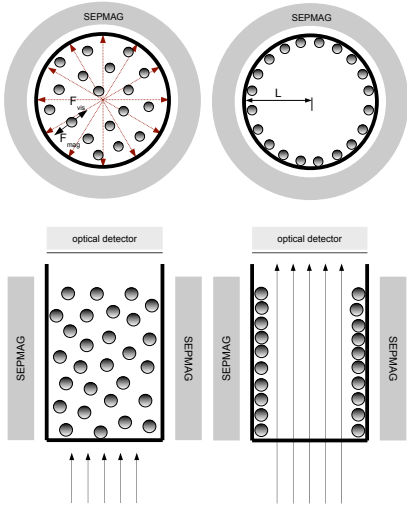

FIG. 5: Sketch of the magnetophoresis process and opacity measurements. Top: the homogeneously dispersed nanoparticles (left) move towards the vessel wall (with radius L) due to the magnetic gradient in the radial direction. At the end of the process (right), all the magnetic particles are close to the vessel wall and the "clean" solution can be removed by pumping it from the center of the vessel. Bottom: The light incides from below and reaches the photoresistance (situated at the top of the bottle) after dispersion by the sample. Initially (left), particles are uniformly distributed in the bottle containing the dispersion and the opacity of the sample is high. After some time (right), particles move towards the walls of the container leaving a clean circle behind so that the opacity of the sample decreases.

noise of the measurement is around 1 mV. Opacities below 0.1 approach quickly the experimental sensitivity limits and are therefore difficult to measure. In fact, these low values of opacity correspond to nearly transparent samples and the separation process has almost concluded.

[1] M. Benelmekki, C. Caparros , A. Montras, R. Goncalves, S. Lanceros-Mendez, Ll. M. Martínez, *J. Nanopart. Res.* **13**, 3199 (2010).
[2] Ching-Ju Chin, S. Yiacoum, C. Tsouris, *Colloids Surf., A*, **204** 63 (2002).
[3] R.E Rosensweig, *Ferrohydrodynamics*. Cambridge University Press, 1st Edition, New York (1985).
[4] D.F. Evans and H. Wennerström, *The Colloidal Domain*, Wiley-WCH, 2nd Edition, New York (1999).
[5] C. P. Bean and J. D. Livingstone, *J. Appl. Phys.*, **30** 120S (1959).
[6] R. Kaiser and G. Miskolczy, *J. Apply. Phys.*, **41** 1064 (1970).
[7] D. X. Chen, A. Sanchez, E. Taboada, A. Roig, N. Sun and H. C. Gu, *J. Appl. Phys.*, **105** 083924 (2009).
[8] E. Taboada, R. Solanas, E. Rodríguez, R. Weissleder and A. Roig, *Adv. Func. Mater.*, **19** 2319 (2009).
[9] V. Schaller et al., *J. Appl. Phys.*, **104** 093918 (2008).
[10] SEPMAG Technologies, http://www.sepmag.eu
[11] See video at `http://www.youtube.com/watch?v=BVipEdKoMh8`
[12] G. de las Cuevas, J. Faraudo, J. Camacho, *J. Phys. Chem. C*, **112** 945 (2008)

5.4 Article 4

"Simulation of magnetophoretic separation processes in dispersions of superparamagnetic nanoparticles in the noncooperative regime."
Jordi S. Andreu, Pablo Barbero, Juan Camacho and Jordi Faraudo
Journal of Nanomaterials **Article ID:** 678581 (2012)

Hindawi Publishing Corporation
Journal of Nanomaterials
Volume 2012, Article ID 678581, 10 pages
doi:10.1155/2012/678581

Research Article

Simulation of Magnetophoretic Separation Processes in Dispersions of Superparamagnetic Nanoparticles in the Noncooperative Regime

Jordi S. Andreu,[1,2] Pablo Barbero,[2] Juan Camacho,[2] and Jordi Faraudo[1]

[1] *Materials Simulation and Theory Department, Institut de Ciència de Materials de Barcelona (ICMAB-CSIC), Campus UAB, 08193 Bellaterra, Spain*
[2] *Departament de Física, Universitat Autònoma de Barcelona, Campus UAB, 08193 Bellaterra, Spain*

Correspondence should be addressed to Jordi S. Andreu, jandreu@icmab.es

Received 15 December 2011; Accepted 30 January 2012

Academic Editor: Carlos Martinez-Boubeta

Magnetic separation has gained much attention due to its implications in different fields, becoming feasible as an alternative to existent technologies at the industrial and lab scale. Substantial efforts are focused to improve the magnetic particles used in these applications. Here we show how a relatively simple and low-cost simulation strategy (tracer simulations) can be employed to predict the effect of various key factors in magnetic separation processes, namely, particle properties and magnetic separator designs. For concreteness, we consider here specific problems in magnetic separation. The first one is the effect of different profiles of the magnetic field in the separation of magnetic nanoparticles, and the second one is the magnetophoresis of colloidal particles in a dispersion of magnetic nanoparticles.

1. Introduction

The manipulation of magnetic particles by the use of inhomogeneous magnetic fields has emerged as a topic of great interest in a wide range of research and technological areas [1]: from wastewater treatments [2, 3] or pollutants removal [4] to biomedical applications like protein isolation, drug delivery, magnetic hyperthermia, or magnetic particle imaging [5, 6]. The use of inhomogeneous magnetic fields to drive magnetic particles apart from solution, what is known as magnetic separation or magnetophoresis, has provided new techniques capable to improve standard technologies, especially in biotechnological applications [7].

The idea behind magnetic separation is to take advantage of the distinctive magnetic response of the particles in solution to remove them from complex mixtures by the use of applied inhomogeneous magnetic fields [8]. In a wide range of applications, magnetic particles are typically functionalized with proper chemical groups, designed to bind to specific nonmagnetic components, thus enabling the separation of nonmagnetic materials by combining the use of magnetic particles and magnetic fields. This combination has many advantages over traditional fixed-bed separation methods, such as activated carbon adsorption for organics and affinity chromatography for proteins. In particular, magnetic nanoparticles offer large exposed surface areas without the use of porous materials, which are often plagued by high mass transfer resistances [9]. Therefore, it is not surprising that magnetic separation has been presented as an alternative to typical centrifugation and filtration steps in industrial processes as well as in lab applications. In the biomedical field, magnetic separation may help to overcome some disadvantages of standard column liquid chromatography in the separation of proteins and peptides, and it serves as a basis of various immunoassays systems. Moreover, magnetic separation can also be used to concentrate large volumes of diluted protein solutions in a very gentle way [7].

The basic ingredients in any magnetic separation application are two: the selection of appropriate magnetic particles

and the design of the magnetic separator. Typically, the particles employed in these applications are superparamagnetic particles. One has to bear in mind that superparamagnetism emerges as a quantum effect in some ferromagnetic and ferrimagnetic materials, below the single domain size. This implies that this phenomenon is limited to nanocrystals of size below a certain critical size which depends on the material [10]. Since the magnetic force is proportional to the particle magnetization, superparamagnetic nanoparticles with large magnetic response are desired. A standard way to enhance the magnetic response of the carrier particles is to synthesize larger particles by embedding superparamagnetic nanocrystals in a matrix of nonmagnetic material (such as polystyrene [11] or silica [12]), thus preserving the superparamagnetic behavior of these crystals and guaranteeing the stability and biocompatibility of the solutions. In this manner, particles with larger magnetizations are obtained, increasing the magnetic response under an external field. Nevertheless, one has to balance this increase on the magnetic response (which could enhance the separation process) with the reduction on the active surface area of the particles, implying a reduction on the capture and retention of target entities. Actually, a wide range of different particles are already commercially available (from nanoparticles to larger superparamagnetic colloids) combining different magnetic response, size and decorated surfaces designed to target specific components.

A second issue about the separation process is the application of a specific magnetic field over the target sample, inducing a magnetic moment in the carrier particles. This magnetic field has not only to induce a magnetic moment but also to generate a magnetic gradient (which produces a magnetic force on the particle) in order to drive carrier particles apart from solution. Then, the conditions to be fulfilled by the magnetic field source are two: it has to induce large magnetizations but also a gradient in the intensity of the magnetic field. The simplest option to induce magnetophoresis in a lab tube or vial is by the application of a simple bar magnet, but this option is highly inefficient, since typically only those particles near the magnet really experience enough magnetic force to move. However, it is possible to obtain efficient magnetic separators by combining permanent magnets in convenient arrangements in order to generate magnetic fields suitable for magnetic separation. Among the possible arrangements of the magnets, we will discuss here the advantages and drawbacks of two possible cylindrical tube geometries, which have been called open and closed arrangements. Essentially, the closed structure consists of an arrangement of magnets around the tube containing the suspension, which generates a uniform magnetic gradient pointing towards the wall of the tube (see, e.g., [13–17]). In this case, one obtains uniform magnetophoretic conditions, a desirable feature in order to characterize, model, and scale-up the magnetophoresis process. The open-type magnetic separator [18, 19] is similar to the previous one, but in this case the design contains an aperture, that is, there is a region near the tube walls which does not contain magnets. These open structures are designed to operate directly to test tube racks and helps on the visual monitoring of the process. In a preliminary communication [20], we noted that these two different separator designs induce substantial differences in the dynamics of the magnetic separation process.

Here, we propose a simple simulation methodology which allows to model the magnetophoretic separation of nanoparticles inside different designs of magnetic separators. As a first application, the methodology proposed here will be employed to compare the performance of open and closed separator designs. In a second one, we will study the magnetophoretic separation process of a mixture containing particles with different sizes and magnetic responses.

2. Tracer Simulation of Magnetophoresis of Superparamagnetic Nanoparticles

2.1. Basic Equations and Simulation Methodology. Let us start by describing the equations of motion of superparamagnetic nanoparticles (NPs) in a liquid dispersion under the effects of an external magnetic field. In this situation, NPs will move in the direction of the magnetic gradient (magnetophoresis). As shown experimentally and theoretically in previous works [13, 17], we have two different kinds of magnetophoretic separation processes. The first case is called cooperative magnetophoresis, and it is characterized by fast separation times (magnetophoretic velocities can be roughly estimated as of the order of a cm per minute) which depend strongly on the concentration of the sample. It is usually found for composite colloids of several hundreds of nm in diameter (made of magnetic NPs embedded in a nonmagnetic matrix) and its driving force is the reversible formation of chains of colloids under the magnetic field [13]. The second case corresponds to noncooperative magnetophoresis, and it is typically found for dispersions of small NPs [17]. In this case, magnetophoretic velocities are much lower, and they do not depend on particle concentration; instead, they depend strongly on the magnetic gradient and the design of the magnetic separator [17, 20]. In this case, the magnetophoretic separation process is ruled by the individual motion of the superparamagnetic NPs. In addition to experimental characterization of both situations, we have formulated a mathematical criterion which allows us to predict whether we will observe cooperative or noncooperative magnetophoresis. This criterion (see [17] for details) establishes that cooperative magnetophoresis is observed when the aggregation parameter N^* verifies $N^* > 1$. This parameter is given by

$$N^* = \sqrt{\phi_0 e^{\Gamma - 1}}, \tag{1}$$

where ϕ_0 is the initial volume fraction of particles in suspension, and Γ is the magnetic coupling parameter characterizing the strength of magnetic interaction of particles at contact as compared with thermal agitation and defined as

$$\Gamma = \frac{\mu_0 m_s^2}{2\pi d^3 k_B T}. \tag{2}$$

In (2) μ_0 is the permeability of the free space, m_s is the magnetic moment of a particle at saturation, d is its diameter, and T the absolute temperature.

In this work, we will consider only the noncooperative case characterized by $N^* < 1$, which is typically the case for

dispersions of NPs. For example, a 10 g/L dispersion of superparamagnetic γ-Fe_2O_3 NPs (diameter 12 nm) employed in [17] provide $\Gamma = 2.5$ and $N^* = 0.1$.

Under these conditions, we thus need to consider only the individual motion of NPs in the magnetic gradient to obtain the magnetophoretic behavior, ignoring the interaction between NPs. The magnetophoretic velocity of a NP immersed in a fluid with viscosity η submitted to a magnetic gradient can be obtained as follows. The magnetic force acting on a magnetic particle can be written as

$$\vec{F}_{\text{mag}} = \mu_0 V \rho_p \left(\vec{M}(H) \cdot \nabla\right)\vec{H}, \tag{3}$$

where $\vec{H}$ is the magnetic field, V is the volume of the particle, ρ_p is its density, and $\vec{M}$ is the magnetization of the particle per unit mass. Notice here that this expression assumes that the magnetization of the particle is uniform [8] so that the magnetic moment is given by

$$m(H) = V \rho_p M(H). \tag{4}$$

Nevertheless, in the case of a superparamagnetic particle, its total magnetic moment aligns parallel to the applied magnetic field and (3) can be written as

$$\vec{F}_{\text{mag}} = \mu_0 V \rho_p M(H) \vec{\nabla} H, \tag{5}$$

where H is the modulus of the magnetic field. On the other hand, the viscous drag force exerted by the solvent over a single spherical particle of radius R is

$$\vec{F}_{\text{vis}} = -6\pi\eta R \vec{v}. \tag{6}$$

The magnetophoretic velocity of a particle in the steady state is obtained by balancing the magnetic force F_{mag} and the viscous drag force F_{vis} exerted by the solvent:

$$\vec{v} = \frac{2\mu_0 \rho_p M(H) R^2}{9\eta} \vec{\nabla} H. \tag{7}$$

In order to apply (7) in a real situation, one needs to know not only the profile of the applied magnetic field but also a full characterization of the magnetic response $M(H)$ of the NPs. In our calculations, we will assume that the magnetization $M(H)$ of a single superparamagnetic nanoparticle under an external magnetic field H is described within a good approximation by a Langevin function typical in theoretical descriptions of this superparamagnetic behavior [10, 21–23]

$$M(H) = M_s \mathcal{L}[b\mu_0 H], \qquad \mathcal{L}[x] = \coth x - \frac{1}{x}, \tag{8}$$

where M_s denotes the saturation magnetic moment per unit mass, and b is related to M_s and R by (see [17, 22])

$$b = \frac{m_s}{k_B T} = \frac{4\pi R^3 M_s \rho_p}{3 k_B T}. \tag{9}$$

The value of b^{-1} can be interpreted as a characteristic magnetic field required to reach saturation. Equations (7)–(9) allow one to predict the magnetophoretic motion of a superparamagnetic NP if the spatial profile of the magnetic field of the magnetic separator is known.

In the case of a very simple geometry for the magnetic field, it has been possible [17] to obtain analytically an exact equation for the trajectory of a NP inside a magnetic separator and also obtain the kinetics of the separation process (number of particles remaining in solution as a function of time). However, for a general magnetic field geometry, finding an analytical solution is not possible. The option explored in this paper will be to perform simulations of tracer particles under known magnetic profiles. In this simulation method, each particle tracer is not intended to represent a real particle but it effectively describes the dynamics of a given particle under the external conditions imposed (tracer simulations are common in fields such as fluid mechanics, see, e.g., [24]).

The simulation technique is as follows. First of all, we need to know the geometry of the magnetic separator and the magnetic field $H(\vec{r})$ in all points inside the magnetic separator. Then, we consider the motion of N_p tracers inside the given geometry and magnetic field. Initially ($t = 0$), the positions $\vec{r}_i(t = 0)$ ($i = 1, \ldots, N_p$) of these tracers are generated to be distributed uniformly inside the magnetic separator. The simulation then proceeds by assuming that each of these tracers behaves as a superparamagnetic NP. The position $\vec{r}_i(t)$ of a tracer evolves obeying

$$\frac{d\vec{r}_i}{dt} = \vec{v}(\vec{r}_i), \tag{10}$$

where the magnetophoretic velocity $\vec{v}(\vec{r}_i)$ is computed from (7)–(9) taking into account the local value of the magnetic field and the magnetic gradient evaluated at position $\vec{r}_i$. The equation of motion of the tracers ((10) supplemented with (7)–(9)) is integrated numerically in discrete time steps Δt by employing a Verlet [25] type integration algorithm which provides good accuracy at a reasonable cost of CPU time. All these calculations were implemented in a C code developed in house, which is available under request to the authors.

2.2. Validation of the Simulation Methodology. In this subsection, we will consider a magnetophoretic separation problem for which we obtained both experimental results and an analytical solution. Comparison of the results of our simulations with previously known results is a necessary step in order to ensure the validity of our simulation approach. After this validation step, we will employ our simulation method in the following subsection to explore other situations in which previous theoretical results are not available.

Here we consider the closed geometry for the magnetic separator, similar to the actual separators employed in recent experimental works [13, 15–17]. The geometry of the separator is a cylinder (radius $L = 1.5$ cm), and it contains a magnetic field increasing from zero in the center to a maximum value at the walls, as shown in Figure 1 (see also inset in Figure 2 for a sketch of the separator). Note that the gradient of the modulus of the magnetic field is approximately uniform inside the system ($\approx$30 T/m). The parameters for the simulation were selected in order to match the experimental system considered in Figure 1 of [17]. In

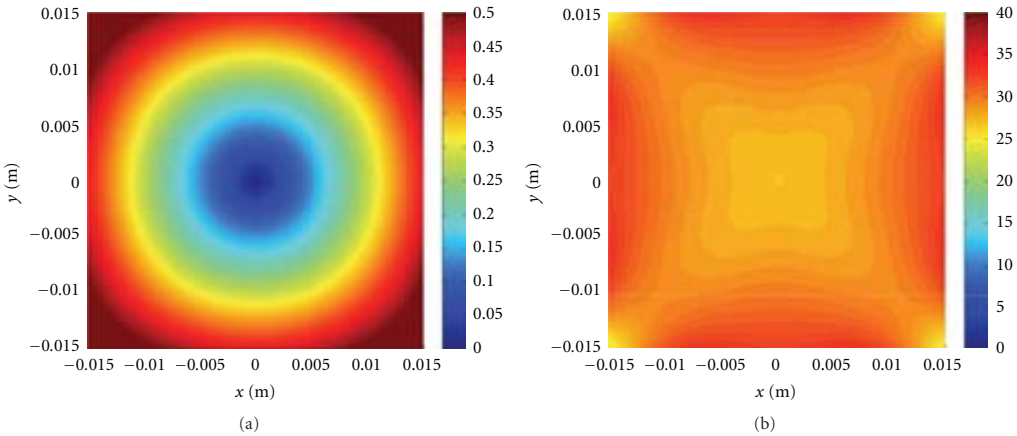

Figure 1: Profile of the magnitude (modulus) of the quadrupolar magnetic field in Tesla (a) and its gradient in Tesla/m (b) for the closed type magnetic separator (top view) employed in the simulations. Note that the magnitude of gradient of the field intensity corresponds to ≈30 T/m in most regions of the separator; however, inhomogeneities due to the quadrupolar nature of the field can be clearly seen.

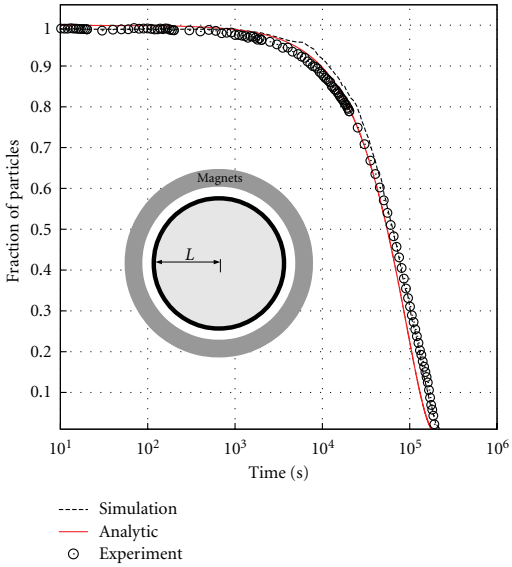

Figure 2: Magnetophoretic separation of superparamagnetic γ-Fe_2O_3 NPs of diameter 12 nm inside a 30 T/m magnetic separator. Comparison between the simulations performed here, the analytical solution and the experimental results reported in [17] for the evolution of the fraction of particles remaining in the separator. Inset: sketch (top view) of the magnetic separator.

this experiment, a 10 g/L dispersion of superparamagnetic γ-Fe_2O_3 NPs (diameter 12 nm) was placed inside the separator. The magnetization curve for these NPs was given also in [17], and it was shown that they obey (8) and (9) with $m_s = (4/3)\pi R^3 \rho_p M_s = 3 \times 10^{-19}$ J/T and $b = 68\,\mathrm{T}^{-1}$. The employed solvent was water (with viscosity $\eta \simeq 0.001$ Pa · s at 298 K). Our tracer simulations were performed considering $N_p = 10^3$ tracer particles and a time step of $\Delta t = 10^2$ s. The simulations were performed until a simulation time of 2×10^5 s. The calculations required only 26 min of CPU running in a single core of an AMD Opteron Magny Cours 6136 processor. During the simulation, we saved the trajectories of the tracer particles for further analysis. From these results, we estimated the concentration profile of the NPs at different times and we also computed the time evolution of the fraction of particles inside the dispersion (i.e., the number of tracers which have not reached the walls of the system divided by the total number of tracers). This last quantity is compared in Figure 2 with the experimental results obtained in [17]. We also show the results corresponding to the analytical expression developed in [17]. Our simulation results are in good agreement with these previous results, thereby validating our simulation technique.

2.3. Comparison between Different Separator Designs. Now, we employ our simulation methodology to compare the performance of two different designs of magnetic separators. The first design we consider here is the one considered in the previous subsection, which we will call "closed type" separator from now on. As we said previously, the main advantage of this geometry for the magnetic separator is the fact that the magnetic gradient is approximately uniform inside the system. The second design we will consider here is an "open type" separator. In this case, the geometry of the separator is the same as the closed type considered in the previous subsection, but now part of the magnets were removed. As we have mentioned in the introduction, this partial removal of magnets is made in commercial separators in order to facilitate visual contact with the dispersion during the separation process so that the separation can be monitored easily

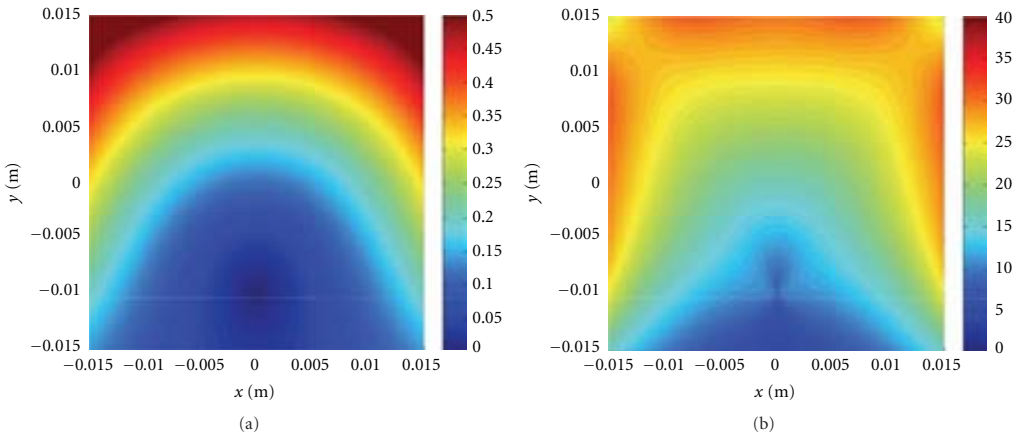

Figure 3: Profile of the magnitude of the magnetic field B in Tesla (a) and its gradient in Tesla/m (b) in the open-type magnetic separator employed in the simulations.

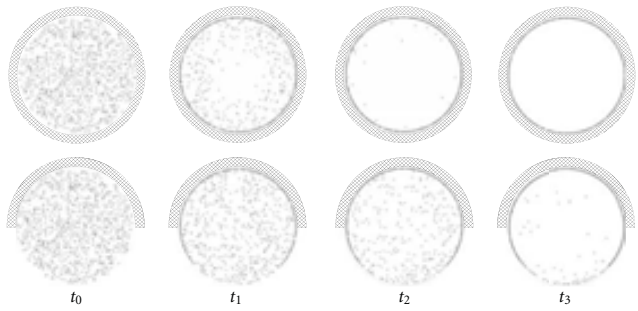

Figure 4: Series of snapshots extracted from simulations comparing the time evolution of the separation process in the closed-geometry (upper row) and open-geometry (bottom row) schemes. The snapshots are taken from a top view of the cylindrical separator with radial geometry. The different snapshots correspond to different times during separation ($t_0 = 0$, $t_1 = 1 \times 10^5$ s, $t_2 = 2 \times 10^5$ s and $t_3 = 5 \times 10^5$ s).

by eye inspection [19] (in closed type separators as the one considered in the previous subsection, monitoring of the separator process is made by an optical sensor, see, e.g., [13]). In Figure 3 we show the profile of the magnetic field generated by a hypothetical open-type magnetic separator constructed by removing half of the magnets from the closed type magnetic separator employed in the previous subsection. In this open case, the magnetic gradient is far from uniform. It is again about 30 T/m near the magnets, but now it is less than 10 T/m in a substantial part of the separator (the region far from the magnets). We will employ these profiles of magnetic field and gradient in order to compare the performance of the open and closed separator designs in a simulation of a specific example of magnetic separation.

In order to compare the different performance between the open and the closed type separators, we consider the same suspension of γ-Fe_2O_3 NPs of diameter 12 nm described in the previous subsection. Now we perform simulations for this suspension in the case of open-type geometry of the magnetic separator. The technical details (number of tracer particles, time step, etc.) were the same as employed in the simulation of the previous subsection. Here, the simulations were performed until a simulation time of 1.2×10^6 s, and the calculations required 39 min of CPU in a AMD Opteron Magny Cours 6136 processor. The corresponding results are presented in Figure 4 (snapshots) and Figure 5 (fraction of remaining particles as a function of time). The differences between results for both types of separators are clear. In the closed type geometry, the motion of particles is much more uniform since the magnetic gradient is nearly uniform in the whole system. In this case, separation proceeds by a radial motion of the particles towards the wall (following the magnetic gradient, see (7)), leaving a circle of "clear" solution (free of particles) which increases with time. In the open-type case, the distribution of particles becomes inhomogeneous as separation proceeds, because of the inhomogeneities in the magnetic gradient (see Figure 3). Particles close to the magnets move faster than the ones placed far from the magnets (Figure 4, top) since they experience larger magnetizations and larger magnetic gradients (see Figure 3). Also,

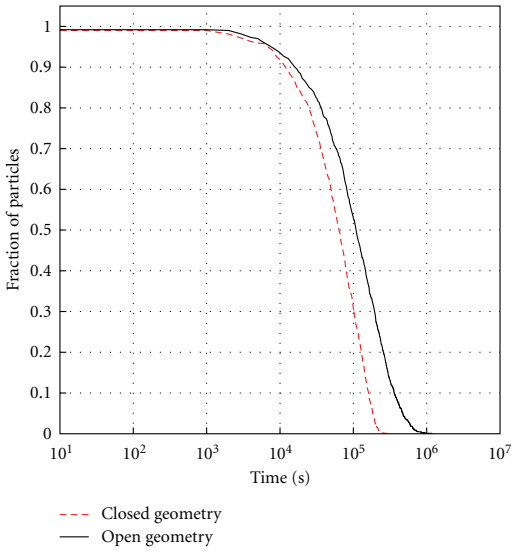

Figure 5: Comparison of the fraction of particles in solution as a function of time as obtained in tracer simulations for open and closed type magnetic separators with magnetic profiles shown in Figures 1 and 3 (see text for details).

these slow-moving particles have to travel distances larger than the cylinder radius in order to reach the walls of the system and become separated from the liquid. As a consequence, separation times are substantially longer in open-type separators than in closed type separators, as shown in Figure 5.

3. Magnetophoresis of Colloidal Particles in a Magnetic Fluid

3.1. Motivation and Basic Equations. The problem we would like to consider in this section is the motion of colloidal particles (with sizes of the order of hundreds of nm or larger) in a dispersion containing superparamagnetic NPs. This particularly asymmetric mixture has a fascinating behavior which has received significant attention in recent years. For example, it is possible to induce the assembly and transport of nonmagnetic colloids immersed in a dispersion of superparamagnetic NPs by applying external magnetic fields [26, 27]. Physically, this interesting behavior is due to the fact that a nonmagnetic colloidal particle, immersed in a suspension of NPs, behaves as a magnetic hole with an effective dipole pointing in a direction opposed to that of the local magnetization of the NPs. Hence, after the application of a magnetic field, a nonmagnetic colloid immersed in a dispersion of NPs behaves as an effective super-diamagnetic particle. This effect is not only found in nonmagnetic colloids but also it is possible in the case of composite colloidal particles made of superparamagnetic NPs embedded in a nonmagnetic matrix (e.g., polymer or silica). As demonstrated in [8, 28, 29] theoretically and experimentally, a colloidal particle in a dispersion of superparamagnetic NPs under a magnetic field H behaves as having an effective magnetic dipole given by

$$m_{\text{eff}}(H) = m_c(H) - \frac{4}{3}\pi R_c^3 n_p m_p(H), \tag{11}$$

where $m_c(H)$ is the intrinsic magnetic dipole of the colloid (the one observed when the colloid is not embedded in a dispersion of NPs), R_c is the radius of the colloid, n_p is the local concentration of NPs (in number of particles per unit volume), and $m_p(H)$ is the magnetic dipole of the NPs induced by the external field H. Equation (11) can be interpreted as a magnetic buoyancy effect due to the different magnetic response of the colloid and its surroundings, as discussed in [8]. Note that a nonmagnetic colloid ($m_c = 0$) will have always $m_{\text{eff}} < 0$, that is, a super-diamagnetic behavior with an effective dipole opposite to that of the superparamagnetic NPs. In the case of $m_c > 0$, the behavior of the colloids can be tuned to an effective superparamagnetic ($m_{\text{eff}} > 0$) or super-diamagnetic ($m_{\text{eff}} < 0$) behavior depending on the concentration of NPs.

Here, our interest will be the study of the behavior of a mixture of colloidal particles and NPs in a magnetic separator. Experimentally, this system has been studied in [30] in the case of a closed type separator. The magnetophoretic velocity of the superparamagnetic NPs will obey the same equations discussed in Section 2. In particular, the NPs will move in the direction of the magnetic gradient with a velocity given by (7). The magnetophoretic velocity of a colloidal particle v_c can be easily obtained using the same relations derived in Section 2 but taking into account that the magnetic dipole of the colloid is described by m_{eff} as given by (11). The result is given by

$$\vec{v}_c(\vec{r}) = \vec{v}_p(\vec{r})\frac{R_p}{R_c}\left[\frac{m_c}{m_p} - \frac{4}{3}\pi R_c^3 n_p(\vec{r},t)\right], \tag{12}$$

where $\vec{v}_p(\vec{r})$ is the magnetophoretic velocity of a NP located at $\vec{r}$, and $n_p(\vec{r},t)$ is the local concentration of NPs at $\vec{r}$ and time t.

3.2. Simulations: Methodology and Results. The simulation methodology employed here is based on particle tracers simulations as developed in the previous section. Now, we will have two different types of tracer particles, one corresponding to NPs and another one corresponding to colloidal particles. For simplicity, we will consider the simulation of this mixture only in the case of closed type magnetic separators. The profile of the magnetic field is shown in Figure 1. As we have seen in the previous section, this case is more easy to understand due to the near uniformity of the magnetic gradient. In this case, the magnetic gradient is pointing in the radial direction, and it has a constant magnitude. Hence, (7) gives the following expression for the radial velocity of a NP at a radial distance r from the center of this cylindrical separator:

$$v_p(r) = \frac{2\mu_0 R_p^2 \rho_p M(H)}{9\eta}\frac{\partial H}{\partial r}, \tag{13}$$

where $M(H)$ is given by (8) and (9). In the case of the colloidal particles, the radial velocity can be obtained from (12)

$$v_c(r) = v_p(r)\frac{R_p}{R_c}\left[\frac{m_c}{m_p} - N_f(r,t)\right], \quad (14)$$

where N_f is the number of NPs "excluded" by the presence of a colloidal particle, and it is given by

$$N_f(\vec{r},t) = \frac{4}{3}\pi R_c^3 n_p(\vec{r},t). \quad (15)$$

Due to the symmetry of the problem, we consider only the radial motion of the particles so the simulations can be performed in 2 dimensions (the vertical coordinate z was ignored). As in the previous section, the equation of motion of the tracer NPs, $dr/dt = v_p(r)$ was solved using the Verlet integration scheme. Also, we have to solve the motion of the tracer particles corresponding to the colloids. This is done as follows. At each time step (after updating the position of the NPs), we compute the concentration profile of NPs, and the function $N_f(r,t)$ is updated in the following way. The value of $N_f(r,t)$ is given by the initial value N_f^0 multiplied by the ratio between the NPs density found in the region comprised between r and $r + \delta r$ and the initial NPs density. Different combinations of integration time step and δr values were tested. The results reported here correspond to $\delta r = L/100$ where L is the radius of the magnetic separator. Once this function is updated, the velocity of each colloidal tracer is calculated as follows. A first estimate of the velocity for each latex particle at a given time step $v_1(t_n)$ is calculated according to the NPs concentration at time t_n. Then, each latex particle is moved to a new virtual position according to this initial estimate $v_1(t_n)$. Also, we update the position for each NP at time t_{n+1}, the new NPs concentration is computed, and a new estimation of the velocity of each latex particle (located at their virtual positions) is calculated $v_2(t_{n+1})$. Finally, the real velocity used to calculate the position at t_{n+1} for each latex particle is calculated as the average of these two estimates of the latex velocities that is, $v(t_n) = (v_1(t_n) + v_2(t_{n+1}))/2$. This two-steps, methodology is necessary in order to account for the effect of variations in NPs concentration during the motion of the latex particles.

In this case, we have performed a single simulation for a particular case of interest which is now being realized experimentally [30]. We have considered a mixture containing a dispersion of nanoparticles identical to that considered in the previous section (10 g/L dispersion of superparamagnetic γ-Fe_2O_3 NPs of diameter 12 nm) and colloidal particles similar to commercial latex micro spheres (1 g/L dispersion of colloids with diameter 900 nm). In these conditions, the initial value of the quantity N_f defined in (15) is $N_f^0 = 868$ in all the system. As we said before, the magnetic separator considered here is the same closed type separator with a gradient of approximately 30 T/m discussed in Section 2.2. Under these conditions, the behavior of the NPs is the same as discussed in Section 2.2. The behavior of the latex colloids depends strongly on the value considered for m_c. The most interesting case corresponds to the case with $m_c/m_p < N_f$. In this situation, (14) predicts that the initial motion of the colloidal particles will be in the opposite direction to that of NPs. In our simulations, we have focused in the particular case $m_c/m_p = 500$, which we have found realizable experimentally [30].

We have performed different simulations with a total number of 10^6 tracer NPs together with 10^4 tracer latex particles. The initial system configuration was prepared by placing all the particles at random positions inside the separator of radius 1.5 cm. As in previous simulations, the solvent viscosity was set to $0.001\,\text{Pa}\cdot\text{s}$ which corresponds to the viscosity of water at 298 K. The integration time step was set to $\Delta t = 5$ s, and the positions of the particles were recorded at intervals of 50 s. The simulation was performed until a simulated time of 2.9×10^5 s, which required 131 min of CPU. At this point, we recall that all our calculations were performed by a C code developed in house, which is available under request to the authors.

Experimentally [30], it was observed that the latex particles behave in an interesting, nontrivial way. First, it was observed that latex colloids generate a sort of ring-shaped structure. Then, this ring of latex particles experiences a thinning process, and later it moves towards the walls of the system. This experimental behavior is also found in our simulations, as seen in the snapshots in Figure 6, and also it can be seen in the movies provided as supporting online information (see the movies provided in supplementary material available online at doi:10.1155/2012/678581).

The observed profiles of latex particles can be understood from the analysis of the trajectories of individual tracers. Typical trajectories for the radial distance $r(t)$ of latex particles are shown in Figure 7. Latex particles move initially towards the center of the system due to the fact that initially $m_{\text{eff}} < 0$ (see (11)). As time advances, the latex motion is slown down and at certain point (different for each particle), the motion is reversed. For example, a particle starting near the center of the system ($r = 0.1$ cm) reverses its motion after 1 h, reaching the wall after a total of 31 h. A particle starting at the wall (at $r = 1.5$ cm) reverses its motion after 10 h, at a distance $r = 0.7$ cm and reaches the wall ($r = 1.5$ cm) also after 31 h. This reversal of latex motion is due to the radial motion of the NPs towards the walls, which changes the local concentration of NPs. The reversal of the trajectory of a latex particle occurs when it founds a decreased local concentration of NPs at which $m_{\text{eff}} = 0$ ((12) gives a threshold NP concentration of 5.8 g/L for our case). This initial motion towards the center of the system generates the observed formation and thinning of the ring profile of latex particles shown in Figure 6. The subsequent motion of the ring profile of latex towards the wall corresponds to the time at which all latex particles have inverted their motion. All this process is also illustrated in the accompanying movies, showing the motion of latex particles superimposed to the evolution of the concentration profiles of NPs.

3.3. Simplified Model. Although our simulations described in the previous section are not particularly costly from the computational point of view, they require the use of relatively large amounts of disk space to store the tracer trajectories and later analysis to obtain relevant quantities such as concentration profiles and number of particles remaining inside the magnetic separator. For this reason, it could be convenient to

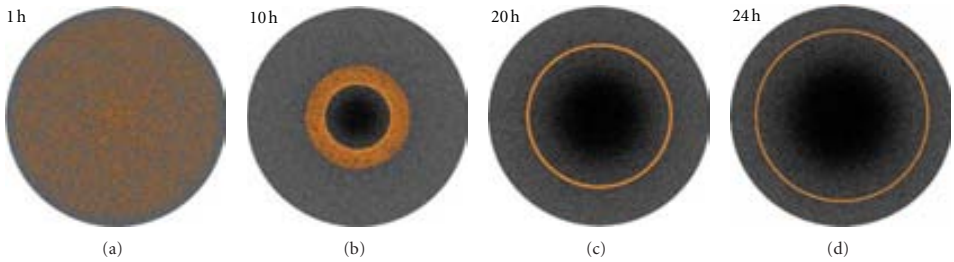

Figure 6: Snapshots from simulations of the magnetophoresis of an aqueous dispersion of γ-Fe_2O_3 superparamagnetic nanoparticles (grey) and latex polystyrene particles (orange) under a magnetic gradient of 30 T/m at different times (1 h, 10 h, 20 h, and 24 h resp.).

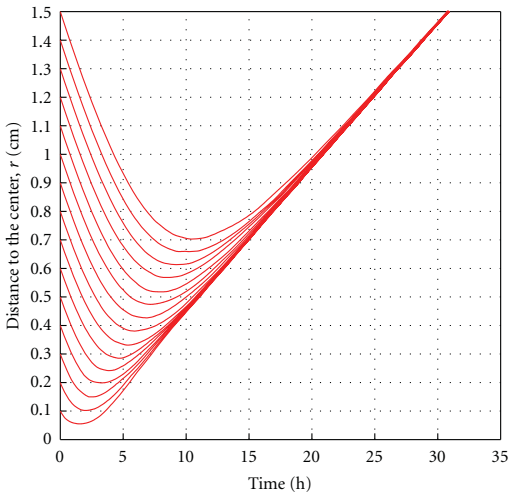

Figure 7: Examples of 15 trajectories obtained in simulations corresponding to tracer latex particles immersed in a dispersion of NPs starting from different distances to the center of the system (see details in the text.)

develop a simplified approach amenable of solution without the need of performing computer simulations.

The motion of the latex particles observed in the simulations can be described with reasonable accuracy with a simple equation. The basic idea is to disregard the radial dependence in the magnetophoretic velocity of the NPs in (13) and assume that the NPs move at constant velocity v_p^s which is the magnetophoretic velocity at magnetic saturation

$$v_p^s = \frac{2R_p^2}{9\eta}\mu_0\left(\frac{\partial H}{\partial r}\right)M_s\rho_p. \tag{16}$$

This approximation is justified by the observation that the magnetic field observed in most parts of the magnetic separator (see Figure 1) is large enough to saturate the NPs. In the case of the 10 g/L suspension of γ-Fe_2O_3 NPs under 30 T/m considered in our previous subsection, we have $v_p^s = 7.9\times10^{-8}$ m/s. Within this approximation, the concentration profile of NPs is given approximately by

$$n_p(r,t) = n_0\left(1-\frac{v_p^s t}{r}\right) \quad \text{for } r > v_p t, \tag{17}$$

$$n_p(r,t) = 0 \quad \text{for } r < v_p t. \tag{18}$$

Using (16)–(18) in (14), we obtain that the trajectory of a latex particle obeys the differential equation

$$\frac{dr}{dt} = v_c(r) = v_p^s\frac{R_p}{R_c}\left[\frac{m_c}{m_p} - \frac{4}{3}\pi R_c^3 n_0\left(1-\frac{v_p^s t}{r}\right)\right]. \tag{19}$$

Equation (19) is a first-order differential equation which can be solved numerically to obtain the trajectory $r(t)$ for a latex particle initially at a position $r(t=0) = r_0$. In Figure 8 we compare the predictions of (19) with the results obtained from tracer simulations. In general, numerical solutions of (19) give a reasonable approximation to colloid trajectories with differences of the order of 10% with simulations. This result is remarkable in view of the apparently strong approximations involved in their derivation (see (16) and (18)). Therefore, in order to estimate systematically the effect of the different parameters of the system (e.g., the effect of the value of m_c), it could be convenient in practice to solve numerically (19) instead of performing a full simulation. However, for more complex magnetic field geometries, to get analytical solutions becomes much more difficult, and numerical simulations as the ones presented here would be necessary.

4. Conclusions

In this work, we have presented a low-cost simulation strategy based on the concept of particle tracers aimed to tackle the magnetophoresis process in the noncooperative magnetophoretic regime. We have successfully validated this simulation approach by comparing the results obtained against existing experimental and also analytical results obtained for the separation process of a colloidal dispersion of γ-Fe_2O_3 superparamagnetic nanoparticles in an aqueous solution. Thanks to this methodology, we have been able to evaluate different key factors involved in the magnetophoretic

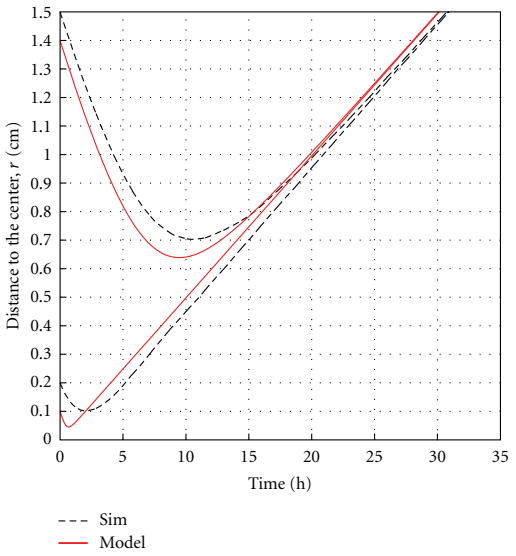

Figure 8: Comparison of trajectories of two tracer latex particles as obtained in the simulations and by numerical solution of (19).

separation process. Regarding the separator design, we have shown that the homogeneous magnetophoretic conditions created by a closed type separator (high magnetic field over almost the whole sample and constant magnetic gradient) enhance the separation process, providing more control over the process and reducing the expected separation time when compared to the open-type version of the separator. We have also extended that methodology to solutions of colloidal particles in aqueous solutions of superparamagnetic nanoparticles in the closed type geometry. The simulation performed in this case is able to account for the ring-like structure expected in some experimental situations and agrees with the simplified numerical model proposed.

Acknowledgments

This work was supported by the Spanish Government Grants no. FIS2009-13370-C02-02, PET2008-02-81-01/02, and CONSOLIDER-NANOSELECT-CSD2007-00041. J. Faraudo and J. Camacho are also supported by the Catalan Government Grant no. 2009SGR164. The authors thank LL. M. Martínez from SEPMAG Technologies for help regarding the calculation of the profiles of the magnetic fields and for extensive discussions.

References

[1] C. T. Yavuz, A. Prakash, J. T. Mayo, and V. L. Colvin, "Magnetic separations: from steel plants to biotechnology," *Chemical Engineering Science*, vol. 64, no. 10, pp. 2510–2521, 2009.

[2] C. De Latour, "Magnetic separation in water pollution control," *IEEE Transactions on Magnetics*, vol. 9, no. 3, pp. 314–316, 1973.

[3] G. Mariani, M. Fabbri, F. Negrini, and P. L. Ribani, "High-Gradient Magnetic Separation of pollutant from wastewaters using permanent magnets," *Separation and Purification Technology*, vol. 72, no. 2, pp. 147–155, 2010.

[4] C. T. Yavuz, J. T. Mayo, W. W. Yu et al., "Low-field magnetic separation of monodisperse Fe_3O_4 nanocrystals," *Science*, vol. 314, no. 5801, pp. 964–967, 2006.

[5] J. L. Corchero and A. Villaverde, "Biomedical applications of distally controlled magnetic nanoparticles," *Trends in Biotechnology*, vol. 27, no. 8, pp. 468–476, 2009.

[6] K. M. Krishnan, "Biomedical nanomagnetics: a spin through possibilities in imaging, diagnostics, and therapy," *IEEE Transactions on Magnetics*, vol. 46, no. 7, Article ID 5439840, pp. 2523–2558, 2010.

[7] I. Safarik and M. Safarikova, "Magnetic techniques for the isolation and purification of proteins and peptides," *BioMagnetic Research and Technology*, vol. 2, no. 1, article no. 7, 2004.

[8] G. Friedman and B. Yellen, "Magnetic separation, manipulation and assembly of solid phase in fluids," *Current Opinion in Colloid and Interface Science*, vol. 10, no. 3-4, pp. 158–166, 2005.

[9] G. D. Moeser, K. A. Roach, W. H. Green, T. A. Hatton, and P. E. Laibinis, "High-gradient magnetic separation of coated magnetic nanoparticles," *AIChE Journal*, vol. 50, no. 11, pp. 2835–2848, 2004.

[10] C. P. Bean and J. D. Livingston, "Superparamagnetism," *Journal of Applied Physics*, vol. 30, no. 4, pp. S120–S129, 1959.

[11] D. Leun and A. K. Sengupta, "Preparation and characterization of magnetically active polymeric particles (MAPPs) for complex environmental separations," *Environmental Science and Technology*, vol. 34, no. 15, pp. 3276–3282, 2000.

[12] E. Taboada, R. Solanas, E. Rodríguez, R. Weissleder, and A. Roig, "Supercritical-fluid-assisted one-pot synthesis of biocompatible core(γ-Fe_2O_3)/shell(SiO_2) nanoparticles as high relaxivity T_2-contrast agents for magnetic resonance imaging," *Advanced Functional Materials*, vol. 19, no. 14, pp. 2319–2324, 2009.

[13] G. De Las Cuevas, J. Faraudo, and J. Camacho, "Low-gradient magnetophoresis through field-induced reversible aggregation," *Journal of Physical Chemistry C*, vol. 112, no. 4, pp. 945–950, 2008.

[14] J. Faraudo and J. Camacho, "Cooperative magnetophoresis of superparamagnetic colloids: theoretical aspects," *Colloid and Polymer Science*, vol. 288, no. 2, pp. 207–215, 2010.

[15] M. Benelmekki, C. Caparros, A. Montras, R. Gonçalves, S. Lanceros-Mendez, and L. M. Martinez, "Horizontal low gradient magnetophoresis behaviour of iron oxide nanoclusters at the different steps of the synthesis route," *Journal of Nanoparticle Research*, vol. 13, no. 8, pp. 3199–3206, 2011.

[16] M. Benelmekki, A. Montras, A. J. Martins, P. J.G. Coutinho, and L. M. Martinez, "Magnetophoresis behaviour at low gradient magnetic field and size control of nickel single core nanobeads," *Journal of Magnetism and Magnetic Materials*, vol. 323, no. 15, pp. 1945–1949, 2011.

[17] J. S. Andreu, J. Camacho, J. Faraudo, M. Benelmekki, C. Rebollo, and L. M. Martínez, "Simple analytical model for the magnetophoretic separation of superparamagnetic dispersions in a uniform magnetic gradient," *Physical Review E*, vol. 84, no. 2, Article ID 021402, 2011.

[18] G. P. Hatch and R. E. Stelter, "Magnetic design considerations for devices and particles used for biological high-gradient

magnetic separation (HGMS) systems," *Journal of Magnetism and Magnetic Materials*, vol. 225, no. 1-2, pp. 262–276, 2001.

[19] S. J. Hershberger, A. Parakka, B. Trudeau, C. Patel, and P. Schultz, "Scalable magnetic designs to achieve comparable capture rates and capture efficiency across multiple vessel diameters," *AIP Conference Proceedings*, vol. 1311, pp. 351–362, 2010.

[20] J. S. Andreu, J. Camacho, J. Faraudo, M. Benelmekki, C. Rebollo, and L. Martínez, "Magnetophoretic separation of superparamagnetic dispersions in a uniform magnetic gradient: experimental study and analytical solution," in *Proceedings of the 4th Iberian Meeting on Colloids and Interfaces*, pp. 191–197, 2011.

[21] R. Kaiser and G. Miskolczy, "Magnetic properties of stable dispersions of subdomain magnetite particles," *Journal of Applied Physics*, vol. 41, no. 3, pp. 1064–1072, 1970.

[22] R. Rosensweig, *Ferrohydrodynamics*, Cambridge University Press, New York, NY, USA, 1st edition, 1985.

[23] D. X. Chen, A. Sanchez, E. Taboada, A. Roig, N. Sun, and H. C. Gu, "Size determination of superparamagnetic nanoparticles from magnetization curve," *Journal of Applied Physics*, vol. 105, no. 8, Article ID 083924, 2009.

[24] J. J. Monaghan, "Particle methods for hydrodynamics," *Computer Physics Reports*, vol. 3, no. 2, pp. 71–124, 1985.

[25] D. Frenkel and B. Smit, *Understanding Molecular Simulations*, Academic Press, 2nd edition, 2001.

[26] B. B. Yellen, O. Hovorka, and G. Friedman, "Arranging matter by magnetic nanoparticle assemblers," *Proceedings of the National Academy of Sciences of the United States of America*, vol. 102, no. 25, pp. 8860–8864, 2005.

[27] R. M. Erb, H. S. Son, B. Samanta, V. M. Rotello, and B. B. Yellen, "Magnetic assembly of colloidal superstructures with multipole symmetry," *Nature*, vol. 457, no. 7232, pp. 999–1002, 2009.

[28] R. M. Erb and B. B. Yellen, "Concentration gradients in mixed magnetic and nonmagnetic colloidal suspensions," *Journal of Applied Physics*, vol. 103, no. 7, Article ID 07A312, 2008.

[29] R. M. Erb, D. S. Sebba, A. A. Lazarides, and B. B. Yellen, "Magnetic field induced concentration gradients in magnetic nanoparticle suspensions: theory and experiment," *Journal of Applied Physics*, vol. 103, no. 6, Article ID 063916, 2008.

[30] M. Benelmekki, Ll. M Martínez, J. Andreu, J. Faraudo, and J. Camacho, "Magnetophoresis of colloidal particles in a dispersion of superparamagnetic nanoparticles: theory and experiments," *Soft Matter*. In press.

5.5 Article 5

"Magnetophoresis of colloidal particles in a dispersion of superparamagnetic nanoparticles: theory and experiments."
Maria Benelmekki, Lluís Miquel Martínez, Jordi S. Andreu, Juan Camacho and Jordi Faraudo
Soft Matter **8**, 6039 (2012)

View Online / Journal Homepage / Table of Contents for this issue
Dynamic Article Links

Soft Matter

Cite this: *Soft Matter*, 2012, **8**, 6039

www.rsc.org/softmatter

PAPER

Magnetophoresis of colloidal particles in a dispersion of superparamagnetic nanoparticles: theory and experiments†

M. Benelmekki,*[a] Ll. M. Martinez,[b] J. S. Andreu,[cd] J. Camacho[d] and J. Faraudo[c]

Received 1st February 2012, Accepted 26th March 2012
DOI: 10.1039/c2sm25243k

Recent works have demonstrated the exciting possibility of inducing a tunable magnetic behavior in non-magnetic colloids by immersing them in a dispersion of superparamagnetic nanoparticles (NPs). Here we show experimentally that non-magnetic latex particles in a dispersion of superparamagnetic NPs experience a nontrivial, two-step "go and come-back" motion when brought under a uniform magnetic gradient. Our theoretical analysis indicates that the observed motion is due to the combined effect of the behavior of latex particles as magnetic holes and the adsorption of NPs at the latex surface. In agreement with theory, the NPs adsorption has been confirmed in our experiments by three independent experimental techniques (EDS, SEM and electrophoresis).

I. Introduction

Recent works have demonstrated the possibility of manipulating non-magnetic colloids by employing magnetic fields.[1–9] The basic requirement that makes this manipulation possible is that the non-magnetic particles should be dispersed in a suspension containing strongly magnetic particles of a smaller size (for example, superparamagnetic nanoparticles). In this case, the non-magnetic particles behave as non-magnetic cavities inside the magnetizable medium and experience a magnetic buoyant force. The non-magnetic particles show an effective diamagnetic response with respect to the surrounding medium.[10]

Several microfluidic applications have been developed taking advantage of this effective diamagnetic response. Zhu *et al.* studied the microfluidic transport of non-magnetic particles of a few microns size immersed in ferrofluids.[7–9] In this work, they showed the possibility to fractionate and focus the non-magnetic particles from solution by depleting the particles' trajectories with respect to the flow direction, similar to the techniques used to control the fractionation of superparamagnetic nanoparticles, such as the split-flow fractionation.[11]

Yellen *et al.*[1] introduced a method for transporting non-magnetic colloidal particles immersed in a ferrofluid by using magnetic trap arrays to drive the particles motion. They employed lithographic patterning into 70 nm thick cobalt thin films to produce reprogrammable magnetic field maps, obtaining dynamic control over the motion of latex particles of various sizes immersed in a ferrofluid. The steady-state particle concentration gradients similar to those obtained in ref. 1 were also studied theoretically[2] and experimentally.[3] They obtained an approximate analytical expression to describe the equilibrium concentration profiles of mixed suspensions of magnetic and non-magnetic nanoparticles under high magnetic field gradients, showing a qualitative agreement with the experimental results reported.

Taking advantage of the induced change on the magnetic response due to the magnetizable medium, Erb and co-workers demonstrated the self-assembly of multicomponent mixtures of paramagnetic and non-magnetic particles in different multipolar geometries with rotationally symmetric arrangements.[4] The stability of these structures was explained on the basis of magnetostatic energy arguments and they were able to predict the formation of different ring structures depending on the ferrofluid concentration.[5] Applying the same principle, Krebs *et al.*[6] successfully created linearly ordered cellular structures inside a passivated ferrofluid which could be applied in tissue engineering applications.

Our interest here is to study the magnetophoretic separation process of mixtures containing magnetic nanoparticles and nonmagnetic particles using a novel magnetophoretic separation method previously introduced for dispersions of superparamagnetic particles.[12–15] A key aspect of this method, as compared with classical magnetophoretic setups, is that the separation process is based on the application of a homogeneous magnetic gradient to drive the removal of the particles, which guarantees uniform magnetophoretic conditions in the entire sample. Also, this situation seems more suitable for establishing a proper framework for the development of theoretical models. As compared with previous examples of magnetic manipulation

[a]*Centro de Física, Universidade do Minho, E-4710-057 Braga, Portugal. E-mail: benelmekki@fisica.uminho.pt*
[b]*Sepmag, Parc Tecnologic del Valles, E-08290 Barcelona, Spain*
[c]*Institut de Ciència de Materials de Barcelona (ICMAB-CSIC), Campus UAB, E-08193 Bellaterra, Spain*
[d]*Departament de Física, Universitat Autònoma de Barcelona, Campus UAB, E-08193 Bellaterra, Spain*

† Electronic supplementary information (ESI) available. See DOI: 10.1039/c2sm25243k

of non-magnetic particles mentioned above, our system is able to operate over larger sample volumes, which could be of interest for some applications. On the other hand, the magnetic fields used here are more than 10 times larger than the ones used in previous applications, bringing the magnetic nanoparticles to the saturation regime and enhancing the effective diamagnetic response of the non-magnetic particles in suspension.

This paper is organized as follows. In Section II, we introduce the concepts and theory necessary to understand the design of our new magnetophoretic experiments in mixtures. The experimental details are presented in Section III and the experimental observations and discussion are presented in Section IV. We finally end up with the conclusions (Section V).

II. Theory: magnetophoretic separation of colloidal particles in a ferrofluid

Our aim in this section is to extend the theory of magnetophoretic separation to the case of a mixed dispersion containing both superparamagnetic nanoparticles and colloidal particles of larger size, lower concentration, and different magnetic properties from those of the superparamagnetic nanoparticles (NPs).

The experimental setup is depicted in Fig. 1. We consider a cylindrical cavity containing a magnetic field which is zero at the center of the system and maximum at the walls. The magnitude of the field varies linearly from the walls to the center, so one obtains a uniform magnetic gradient, as in the magnetophoresis experiments performed in our previous work.[15] This setup is particularly convenient since it provides uniform magnetophoretic conditions in the whole system. Thus, the magnetic force (in this case, towards the vessel wall) experienced by a magnetic particle is given by (see ref. 10 for a detailed derivation):

$$F = m\mu_0 \frac{\partial H}{\partial r} \tag{1}$$

where μ_0 is the magnetic constant, m is the magnetic moment of the particle and $\partial H/\partial r$ is the modulus of the magnetic gradient (which is fairly constant within the system). Such a particle will move towards the walls with a magnetophoretic velocity given by:

$$v = \frac{1}{6\pi\eta R} m\mu_0 \frac{\partial H}{\partial r}, \tag{2}$$

where η is the viscosity of the solvent and R is the radius of the particle. This equation assumes that the magnetic particles do not form chains due to the magnetic field. The conditions (particle size, concentration and magnetic response) for which this requisite is fulfilled have been discussed in detail in ref. 15 and 16. In this case, eqn (2) successfully predicts the magnetophoretic motion of dispersions of superparamagnetic nanoparticles.[15]

Let us consider now the case of interest in this work, namely a mixture consisting of a solvent (water), superparamagnetic nanoparticles (NPs) and colloidal particles of larger size and much lower concentration. The colloidal particles are assumed to have different magnetic properties than the surrounding nanoparticles (the most extreme case is that of non-magnetic colloids). Current theory[1–10] establishes that the behavior of the colloidal particles will be strongly influenced by the mismatch in magnetic properties between the colloids and their environment (the local concentration of NPs with a different magnetic response). Inside the NPs suspension (the magnetic fluid), the behavior of the colloid depends not only on its properties but also on the properties of the surrounding ferrofluid. In order to be more specific, let m_{col} be the dipole of a colloidal particle (which could be zero in the case of non-magnetic particles) and m_f be the magnetic dipole of the NPs induced by the external magnetic field. Inside this mixed dispersion, the colloidal particles will behave as having an effective magnetic dipole given by:[10]

$$m_{eff} = m_{col} - \frac{4}{3}\pi R_{col}^3 n_f m_f, \tag{3}$$

where R_{col} is the radius of the colloidal particles, n_f is the local concentration of NPs (measured in number of nanoparticles per unit volume). Note that in eqn (3), m_{col} depends on R_{col} according to how the magnetic pigment is distributed in the colloid (adsorption at the surface or homogeneous distribution inside all the volume). Eqn (3) implies that a non-magnetic particle ($m_{col} = 0$) behaves as a magnetic hole with an effective magnetization opposite to that of the surrounding ferrofluid. In the case of paramagnetic colloids ($m_{col} > 0$), the effective magnetization could be negative or positive depending on the concentration of NPs (see eqn (3)). This effect has interesting implications. For example, in the presence of a non-uniform magnetic field, the colloids will experience a magnetic force given by eqn (1) and (3). Hence, in the case of $m_{eff} < 0$ colloids and NPs will move in opposite directions due to their different magnetic response. NPs will always move towards the walls of the system and colloids with $m_{eff} < 0$ will move towards the centre of the

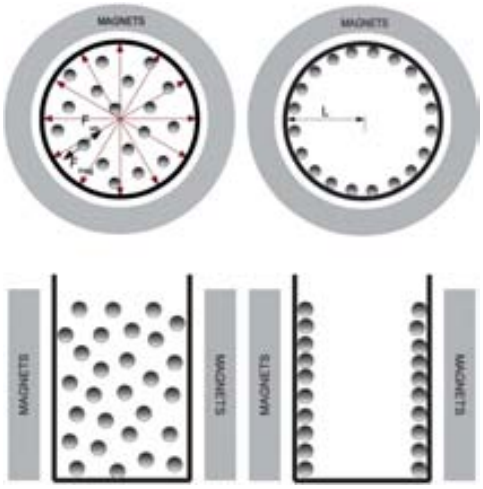

Fig. 1 Sketch (top and lateral view) of the magnetophoresis process in a cylindrical separator with a radial magnetic gradient. The homogeneously dispersed magnetic nanoparticles (left) move towards the vessel wall (with radius L) due to the magnetic gradient in the radial direction. At the end of the process (right), all the magnetic particles are close to the vessel wall and the "clean" solution can be removed by pumping it from the center of the vessel.

system. In fact, using eqn (2) and (3) it is easy to show that the velocity of a colloidal particle (v_{col}) and the velocity of a NP (v_f) are related by

$$v_{col} = v_f \frac{R_f}{R_{col}} \left[\frac{m_{col}}{m_f} - \frac{4}{3}\pi R_{col}^3 n_f \right]. \quad (4)$$

A non-magnetic colloidal particle ($m_{col} = 0$) will always move in the opposite direction to that of NPs. Moreover, according to eqn (4), the magnitude and direction of the magnetophoretic velocity of colloids possessing a magnetic dipole ($m_{col} \neq 0$) will depend on the local concentration of NPs.

Let us now consider the possible trajectories of colloidal particles in a magnetic separator according to eqn (4). To this end, we have first to recall a few facts on the movement of NPs in the system. In a typical magnetic separator such as that shown in Fig. 1, NPs acquire their saturation magnetization and move with approximately constant magnetophoretic velocity, well described by eqn (2) (see ref. 15 for a detailed theoretical and experimental analysis of the magnetophoresis of NPs). For example, consider the 12 nm diameter γ-Fe_2O_3 nanoparticles employed in the experiments of ref. 12, which we will consider again here in the experimental part (Section III). Inside the magnetic separator, these NPs do not form chains (see ref. 15 for details) and therefore eqn (2) can be applied. Using the saturation magnetization for these nanoparticles, eqn (2) gives magnetophoretic velocities of $v_f = 7.9 \times 10^{-8}$ m s^{-1} and $v_f = 1.59 \times 10^{-7}$ m s^{-1} under a 30 T m^{-1} and 60 T m^{-1} magnetic gradient, respectively, in good agreement with experimental results.[15]

Due to their magnetophoretic motion, the local concentration of NPs evolves with time. At a given instant of time t, n_f is given approximately by $n_f(r,t) = n_{f,0}(1 - v_f t/r)$ for distances r verifying $r > v_f t$ and $n_f(r,t) \approx 0$ elsewhere (r is the radial coordinate, $r = 0$ at the centre of the system and $r = L$ at the walls); $n_{f,0}$ is the uniform initial concentration. Hence, in a mixture containing NPs and larger colloidal particles, the velocity of colloidal particles will be affected by these local changes in NPs concentration. From eqn (4) we have:

$$\frac{dr}{dt} = v_{col} = \frac{R_f}{R_{col}} \left[\frac{m_{col}}{m_f} - N_f \left(1 - \frac{v_f t}{r}\right) \right] v_f \quad r > v_f t \quad (5a)$$

$$\frac{dr}{dt} = v_{col} = \frac{R_f}{R_{col}} \frac{m_{col}}{m_f} v_f \quad r \leq v_f t \quad (5b)$$

In eqn (5a) we have defined:

$$N_f = \frac{4}{3}\pi R_{col}^3 n_{f,0} \quad (6)$$

which can be interpreted as the number of NPs "excluded" by the presence of a single colloidal particle in the initial homogeneous solution. Hence, eqn (5a) and (5b) are the differential equations which give the time evolution of the distance r of a latex particle to the centre of the system ($r = 0$). They can be solved numerically to obtain the trajectory $r(t)$ for a latex particle initially at a position $r(t = 0) = r_0$.

In order to illustrate the implications of eqn (5a) and (5b), let us consider a specific example, with parameters relevant to the experiments that will be presented in Section III. We consider a mixture of colloidal particles with radius $R_{col} = 450$ nm (which is typical of commercial latex microspheres) and NPs with a radius of $R_f = 6$ nm. For these NPs, we consider a magnetophoretic velocity of $v_f = 1.59 \times 10^{-7}$ m s^{-1} which was observed for γ-Fe_2O_3 NPs under a 60 T m^{-1} magnetic gradient (see details in ref. 15). Considering a typical concentration of NPs of 10 g L^{-1}, eqn (6) gives $N_f \approx 870$.

Let us first consider the case where the colloidal particles are non-magnetic ($m_{col} = 0$). In this case, eqn (5a) predicts a velocity which is always negative, *i.e.* directed towards the center of the vessel, as illustrated in Fig. 2a. Hence, NPs and colloids move in opposite directions. In this case, colloids behave as having an effective diamagnetic behavior. This opposite motion of colloids and NPs implies that the motion of a colloid will stop at a certain distance of the center, before reaching $r = 0$, as seen in Fig. 2a. This is because the motion of the non-magnetic colloids requires the presence of NPs (see eqn (5a) and (5b)), so when a colloidal particle reaches a region which has been depleted of NPs, it will stop. The final state for the colloidal particles will be a disk-shaped spot which in this example extends from the center of the system up to 0.16 cm (see Fig. 2a). These non-magnetic colloidal particles move an order of magnitude faster than NPs; according to Fig. 2a a colloid starting at the walls moves at a speed of about 1.8×10^{-6} m s^{-1}. Non-magnetic colloidal particles will complete their separation process in about 2.8 hours whereas NPs will require about 26 hours. Hence, one obtains a well-separated final state in which NPs are found at the walls and non-magnetic colloids are found in the central region.

Let us consider now the opposite situation of a large magnetic dipole for the colloidal particles. If this is large enough, it compensates the negative contribution due to the NPs suspension, and the effective diamagnetic behavior described before is not observed here (*i.e.* colloid particles behave as superparamagnetic particles with an effective magnetic dipole smaller than their actual magnetic dipole). Eqn (5a) shows that this happens whenever $m_{col}/m_f > N_f$. In order to be specific, let us consider the case $m_{col}/m_f = 1000 \approx 1.1N_f$ (Fig. 2b). In this case, colloidal particles always move towards the walls, as the NPs. However, the velocity of the colloids is much faster than that of the NPs, completing their separation in only 6 hours (as compared with the 26 hours required by NPs).

Now, let us consider the case of colloidal particles having a weak magnetic dipole. According to eqn (5a), the most interesting case corresponds to colloids with a dipole verifying $m_{col}/m_f < N_f$, since, in that case, the velocity of the colloids can be positive or negative depending on the location of the colloid inside the system. As a particular example, we take $m_{col}/m_f = 500$ (which is around $0.6N_f$). In this case, the motion of the colloidal particles is more complex than in the previous cases, as illustrated in Fig. 2c. For example, a colloid particle initially at the walls will start moving towards the center of the system. However, after reaching half of its trajectory towards the center, it will reverse its motion returning towards the walls. Colloidal particles starting initially at the center of the system will move always towards the walls in the same direction of NPs motion, but with a faster velocity (about 6.7 times faster according to eqn (5b)). This complex motion has interesting consequences over the concentration profiles of colloidal particles. Colloids starting from the walls of the system or the center will move in *opposite* directions. Hence, the colloid region will have the shape of a ring, with

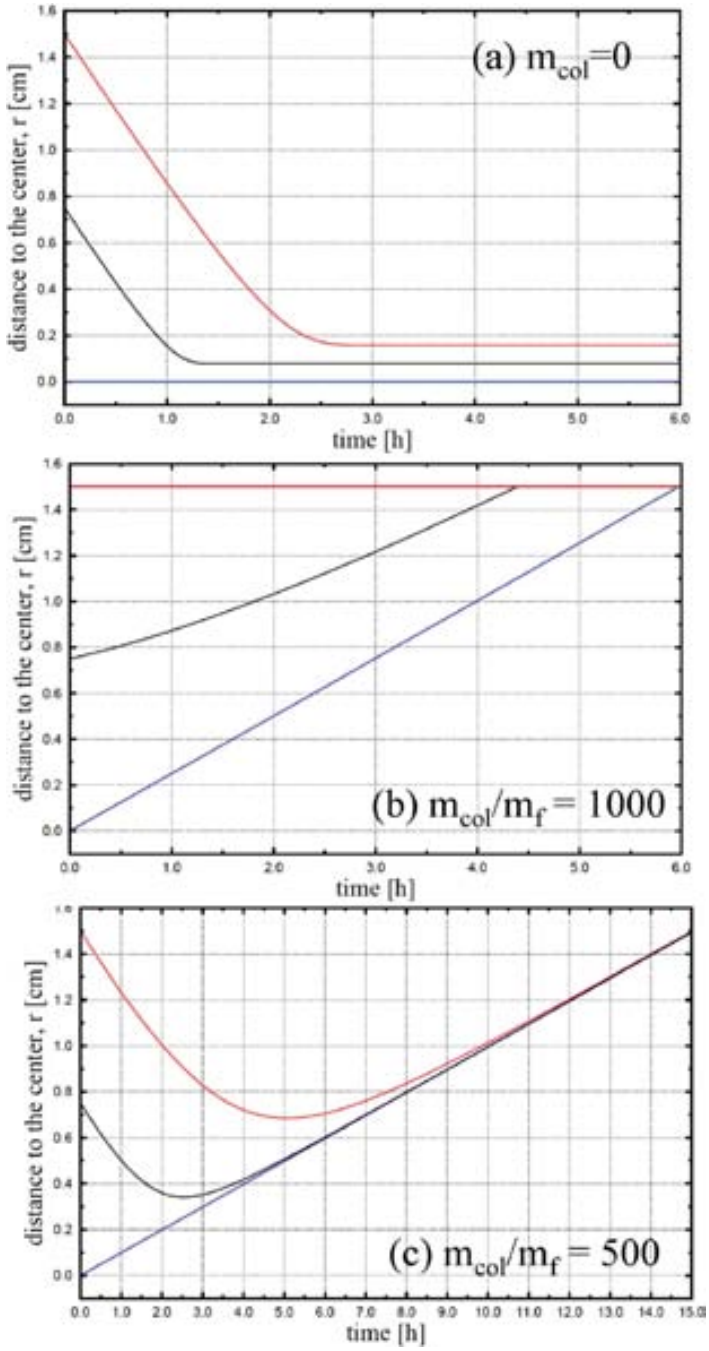

Fig. 2 Trajectories of colloidal particles under 60 T m^{-1} gradient magnetic field in a mixture containing superparamagnetic NPs as obtained from numerical solution of eqn (5a) and (5b) (see text for details). The different lines correspond to colloids initially at different positions of the system: walls of the system (1.5 cm, red line), centre of the system (0 cm, blue line) or the midpoint between these two cases (0.75 cm, black line). Panel (a) corresponds to non-magnetic colloids ($m_{col} = 0$) and panels (b) and (c) correspond to magnetic colloids with $m_{col} = 1000m_f$ and $m_{col} = 500m_f$, respectively.

a concentration hole at the center of the system. As time advances, this ring will experience a *thinning process*, which will last until the particles starting from the walls reverse their motion. After that point (which we will denote as the reversal time T_r), the ring will move towards the walls of the system and the latex particles will arrive at the walls at a separation time T_c *before* the magnetophoresis of NPs is completed. This process of ring formation, ring thinning and final movement of the ring towards the wall is illustrated in the cartoon of Fig. 3.

The values of the reversal time T_r and the colloid separation time T_c depend on the ratio m_{col}/m_f. In order to study this dependence, we have solved again the differential equations eqn (5a) and (5b) for different values of m_{col}/m_f (smaller than N_f). The numerical solution of the trajectories (as done in Fig. 2) allows us to evaluate both the reversal time T_r, the outer radius of the ring r_{ring} at reversal, and the final separation time T_c, *i.e.* the time for the latex particles starting at the center to reach the walls. The results are presented in Table 1. One observes that the reversal time T_r displays a non-trivial behavior; it initially grows with the ratio m_{col}/m_f, reaches a maximum and then decreases. The size of the ring at reversal r_{ring}, however, always grows with m_{col}/m_f, because the speed of colloids towards the center reduces so that they are surpassed by the concentration front closer to the walls. The separation time of the colloids, T_c, always decreases with m_{col}/m_f as expected, *i.e.* more magnetic colloids separate faster.

In addition to the particular examples considered so far, a few general results can be obtained directly without solving eqn (5a) and (5b). First of all, it should be noted that the process of ring formation and movement described in Fig. 3 requires the possibility of inverting the sign of the velocity of the colloids. Therefore, it will occur only for $m_{col}/m_f < N_f$. Hence, the experimental window in which this phenomenon should be observable is quite narrow. However, it is observable as we will demonstrate in Section IV. Another interesting result is that the separation time T_c for completion of the motion of the colloids can be computed without solving eqn (5a) and (5b) as follows. In the case of $m_{col} \neq 0$, this time is determined by the motion of the colloidal particles starting from the center of the system. This motion proceeds with constant velocity, as shown by the blue lines in Fig. 2b and c. This velocity, which we will denote by v_c, can be obtained from eqn (5a) by noting that $r = v_c \times t$ and solving the resulting algebraic equation (with $x = v_c/v_f$)

$$x^2 + \frac{R_{col}}{R_f}\left[N_f - \frac{m_{col}}{m_f}\right] x - \frac{R_{col}}{R_f} N_f = 0 \qquad (7)$$

Then, the separation time of the colloids (T_c) can be computed as $T_c = L/v_c = T_f/x$, where $T_f = L/v_f$ is the separation time for the NPs. The result is given by:

$$T_c = \frac{2T_f}{N_f - \frac{m_{col}}{m_f}} \frac{R_{col}}{R_f} \left[\sqrt{1 + 4\frac{R_{col}}{R_f} \frac{N_f}{\left(N_f - \frac{m_{col}}{m_f}\right)^2}} - 1 \right]^{-1} \qquad (8)$$

Eqn (8) can be employed for direct comparison with experimental results avoiding the necessity of solving the differential eqn (5a) and (5b).

Table 1 Kinetics of the "go and come-back" movement of the latex particles for different values of ferrofluid particles adsorbed onto the latex surface according to theory (see text). T_r is the required time for particles starting at the walls to reverse their movement, and r_{ring} the corresponding distance to the center, *i.e.* the external radius of the ring. T_c is the total time required for the latex particles to reach the walls of the vessel at the end of the separation process

m_{col}/m_f	100	200	300	400	500	600	700	800
T_r [h]	3.4	3.7	4.1	4.7	5.1	5.1	4.1	2.0
r_{ring} [cm]	0.23	0.27	0.36	0.49	0.68	0.94	1.22	1.45
T_c [h]	25.5	22.8	20.1	17.5	15.1	11.7	10.6	8.8

III. Experimental details

The magnetophoresis experiments were performed using a mixture of magnetic fluid consisting of SDS modified maghemite (γ-Fe_2O_3) nanoparticles (SDS-NPs) and a commercial solution of Red Dyed Latex microparticles. The SDS-NPs with a uniform diameter of about 12 nm ($R_f = 6$ nm) are dispersed in distilled water with a concentration of 10 g L^{-1} (ferrofluid). The synthesis and characterization of this ferrofluid are described in

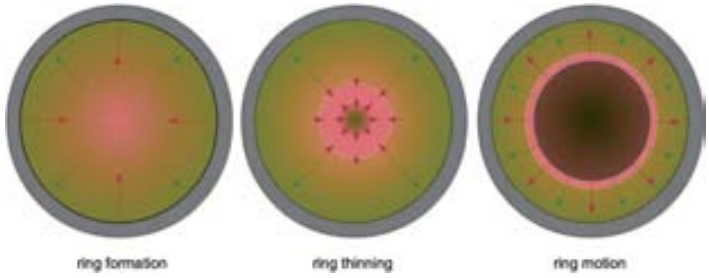

Fig. 3 Cartoon illustrating the predictions of the theory for a dispersion containing a mixture of superparamagnetic NPs and weakly magnetic colloids inside a magnetic gradient. NPs are indicated in green and colloidal particles in pink. NPs move always towards the walls of the magnetic separator (green arrows). Left (ring formation): colloids situated near the walls move towards the centre and colloids situated in the centre move towards the wall, creating a ring of colloids. This ring thins as time goes on (center of the figure) due to the opposite motion of particles located at the center and borders of the ring. Right (ring motion): after some time, colloids moving inward invert their motion and then move outwards. Therefore, thinning of the ring is stopped, and both ends of the ring move at the same radial speed towards the walls of the system.

the ESI† and in ref. 15. Previous magnetophoretic studies of these NP dispersions using the magnetophoretic setup employed here can be found in ref. 15.

An aqueous solution of 10 g L^{-1} of Red Dyed sulfonated Latex microspheres (K100 Red) was kindly provided by Merck Estapor. The diameter of the latex microspheres is about 900 nm. These particles have no functional groups onto their surfaces apart from the SO_4^- terminal groups responsible for the electrostatic stability of the colloids.

Dynamic light scattering (DLS) and particle electrophoresis measurements were performed with a Zetasizer Nano ZS (Malvern instruments), provided by a He/Ne laser of 633 nm wavelength. A NovaTM NanoSEM and Pegasus X4M (EDS/EBSD) were used for scanning electron microscopy and elemental microanalysis, respectively.

The magnetophoresis setups employed in our experiments are the SEPMAG LAB 1 × 25 mL 2042 and 2042 Plus systems, commercially available from SEPMAG company.[17] The systems consist of a cylindrical cavity containing a high permanent magnetic field with a field intensity which increases radially from the center towards the wall. The maps of the magnetic field intensity and its radial gradient are shown in Fig. S4 (ESI†). As seen in Fig. S4†, the radial gradient is approximately uniform. The two systems used in this study correspond to magnetic field gradients of 30 T m^{-1} and 60 T m^{-1} and the absolute values of the magnetic field vary radially from 0 to 0.45 T, and 0 to 0.9 T respectively, being zero at the center and maximal at the cylindrical walls. These values of the magnetic field ensure a substantial magnetization of the employed NPs, as can be seen from the magnetization curve $M(H)$ of the NPs (see ESI†). The NPs can be assumed to be in magnetic saturation for fields larger than 0.1 T, which is verified in almost all the magnetic separators. The region with fields smaller than 0.1 T corresponds to a small central cylindrical region which corresponds to 1.2% of the volume of the 60 T m^{-1} separator and 5% of the volume of the 30 T m^{-1} separator. The non-saturated NPs have a lower magnetic moment implying a slightly slower separation process for this small amount of particles (1.2–5% of the total). However, in terms of a quantitative analysis of the phenomena using the theory described in Section II, these effects are negligible in comparison with other experimental uncertainties (size distribution, exact concentration value, finite size effects in the real magnetic field profile and many others).

Due to the finite height of the separation system, a small vertical magnetic gradient is also present inside the cavity, as shown in Fig. S5 of ESI†. Its value is zero at the symmetry plane, increases slowly and steadily inside the cavity reaching higher values at the ends.

Three suspensions of latex microparticles were prepared with different concentrations (5 g L^{-1}, 1 g L^{-1}, and 0.1 g L^{-1}). 60 μL of each suspension were added to 15 mL of the 10 g L^{-1} ferrofluid. In the case of 5 g L^{-1} latex particles concentration, the suspension was opaque, *i.e.* the incident light from the bottom of the bottle was not able to reach the surface of the solution. In the case of the concentration of 0.1 g L^{-1} of latex particles, the quantity of latex particles was very low and it was difficult to perform simple pictures showing the behavior of the particles during the separation process. The concentration of 1 g L^{-1} of latex particles was the optimum suspension allowing the behavior of the different particles to be shown using a standard photographic camera.

IV. Results and discussion

As shown in Fig. 4, the sample is introduced in the SEPMAG LAB 1 × 25 mL 2042 Plus system (60 T m^{-1} of gradient magnetic field). It is observed that the latex particles start moving from the walls to the center of the bottle (Fig. 4A and B). The inward motion of latex particles initially situated near the walls takes about 6 hours. At this stage (see Fig. 4C1 and C2), there is a clear depletion of latex particles both near the walls and also at the center of the system. As seen in Fig. 4C2, the region containing the latex particles displays a clear ring shape. This ring shaped concentration profile also experiences a motion towards the walls. As shown in Fig. 5 after 24 hours in the SEPMAG LAB 1 × 25 mL 2042 Plus system (60 T m^{-1}), both SDS-NPs and latex particles are found in the walls of the bottle.

We have also performed experiments under a 30 T m^{-1} gradient magnetic field (Fig. 6). In that case, the behavior of the suspension is the same as that in the case of 60 T m^{-1} gradient magnetic field, except for the longer times as expected for the decrease in the magnetic gradient (see eqn.(2)).

Now, we would like to compare the experimental observations with the behavior predicted by eqn (5a) and (5b), discussed in detail in Section II. In the case of $m_{col} = 0$ (non-magnetic colloids) eqn (5a) predicts a motion of latex particles in the direction opposite to that of the magnetic nanoparticles and a final state with the colloidal particles in the central region of the system and the NPs at the walls of the container (see also Fig. 2a). However, the motion observed in our experiments

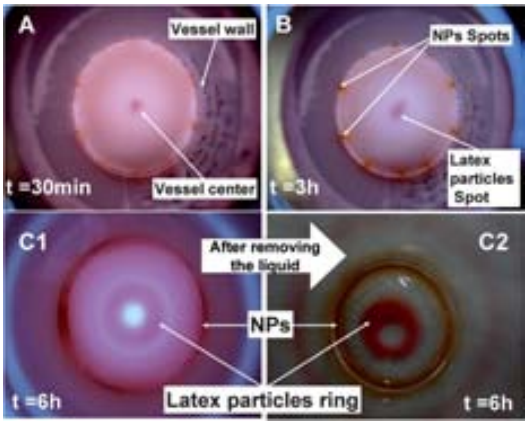

Fig. 4 Magnetophoretic behavior of the mixture of the latex particles (red) and SDS-NPs suspension under a 60 T m^{-1} gradient. (A) After 30 minutes inside the magnetic system, a red spot appears at the center of the vessel indicating the beginning of latex particles migration to the center of the bottle. (B) After 3 hours, brown-yellow spots appear close to the walls of the vessel confirming the continuous arrival of the SDS-NPs to the walls. The central red spot size increases slightly. (C1 and C2) After 6 hours, the latex particles ring is formed. A clear depletion of latex particles both near the walls and also at the center of the system is observed.

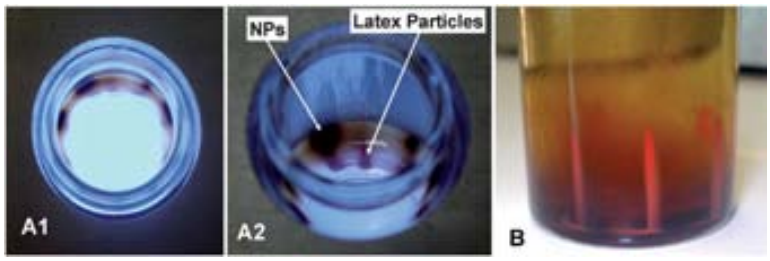

Fig. 5 After 24 hours inside the magnetic system at 60 T m^{-1} both SDS-NPs and latex particles are trapped at the wall of the bottle (A1 and A2). This behavior indicates that both the separation process of SDS-NPs and the "go and come-back" motion of the latex particles have completed. When the bottle is removed from the separation system, a re-suspension of both SDS-NPs and latex particles is observed (B).

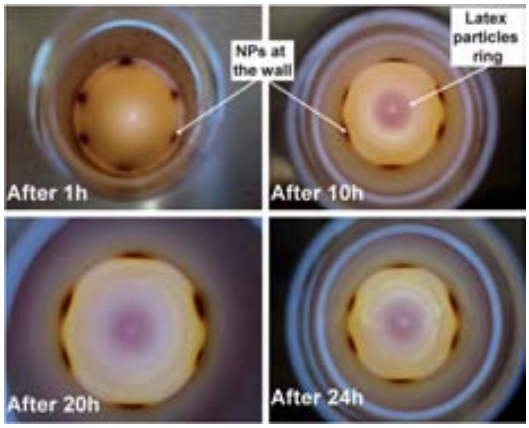

Fig. 6 Magnetophoretic behavior of the mixture of the latex particles and SDS-NPs suspension at 30 T m^{-1}. The pictures show the concentration of the latex particles in the central region of the bottle.

corresponds to the "go and come-back" motion illustrated in Fig. 3 (see also Fig. 2c). Eqn (5a) and (5b) allow this kind of motion only in the case of weak magnetization of the colloids, $m_{col} > 0$ with $m_{col}/m_f < N_f$. The observed motion of the latex particles is consistent with our calculations presented in Section II only if we assume that $m_{col} \neq 0$. This is surprising since the employed latex colloids do not have any magnetic material. A plausible explanation of this behavior is that some NPs are adsorbed at the surface of the latex particles, thereby providing a small but significant magnetic dipole to the colloids. Comparing our experimental observations with the results presented in Table 1 of Section II, we can estimate the number N_a of adsorbed NPs onto each latex colloid, by noting that $N_a = m_{col}/m_f$. These calculations indicate that the number of adsorbed particles should be around $N_a \approx 500$. For this case, we have estimated that formation and thinning of the central ring of colloids require about 5 hours (see Fig. 2c). We also estimate about 15 h for the whole separation process of the latex particles and 26 h for the NPs. A more precise determination of N_a can be done if the separation times of colloids and NPs can be measured accurately. In fact, from both eqn (7) or (8) we obtain for N_a:

$$N_a = \frac{m_{col}}{m_f} = N_f\left[1 - \frac{T_c}{T_f}\right] + \frac{R_{col}}{R_f}\frac{T_f}{T_c} \quad (9)$$

In order to confirm experimentally the adsorption of NPs onto the latex particles, we have conducted SEM imaging, elemental microanalysis (EDS) and electrophoretic mobility measurements. The samples for SEM imaging were obtained from the situation shown in Fig. 4C2 (at $t = 6$ h under 60 T m^{-1}) as follows. The bottle was maintained in the SEPMAG system and the liquid was removed slowly from the bottle. The sample was extracted from the latex particles ring concentrated in the centre of the bottle, for its analysis. For this, a drop of the diluted sample was deposited on a carbon substrate and dried at ambient temperature. Fig. 7 shows the resulting SEM images performed in backscattered electron mode. The images show light spots surrounding the darker latex spheres. These light spots suggest the adhesion of the SDS-NPs to the latex particles. Elemental microanalysis (EDS) was performed on different areas of the sample of about 25 μm^2 each. Depending on the area analyzed, the results show contents of Fe element in the range of 0.3–2.8% in weight. These Fe contents correspond to about 400 and 3000 NPs by each latex particle, respectively (ESI†). This estimate is also consistent with our previous calculations which indicate an adsorbed amount of about 500 NPs per latex particle. One should also keep in mind that in the procedure followed to obtain the samples for the EDS measurements non-adsorbed NPs can also be extracted and hence the number of adsorbed NPs could be overestimated with this method.

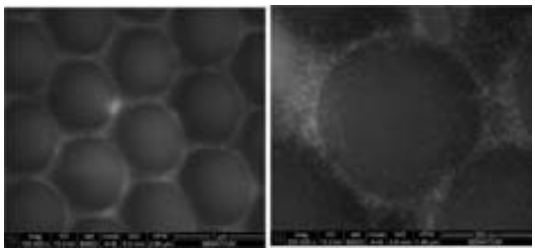

Fig. 7 SEM images in the backscattered detection mode. The images show light spots surrounding the darker latex spheres, which correspond to magnetic nanoparticles.

Another technique which may help in showing evidence for SDS-NPs adsorption is particle electrophoresis. Since both SDS-NPs and latex particles are negatively charged, the adsorption of the NPs onto latex particles gives a resulting entity (latex + NPs) with a larger negative charge than the original latex particles. Therefore, we expect an increase of the measured electrophoretic mobility. We obtained a mobility of $3.5 \times 10^{-8}\ m^2\ V^{-1}\ s^{-1}$ for the SDS-NPs and $4.9 \times 10^{-8}\ m^2\ V^{-1}\ s^{-1}$ for the latex particles (extracted from the original sample, before contact with the SDS-NPs). On the other hand, the measurement of the sample extracted from the mixture of SDS-NPs and latex particles during magnetophoresis shows a mobility peak at $6.2 \times 10^{-8}\ m^2\ V^{-1}\ s^{-1}$. This peak at a larger mobility is consistent with the adsorption of negatively charged SDS-NPs onto negatively charged latex particles.

Even if neither EDS analysis nor electrophoresis measurements can quantify the exact amount of the SDS-NPs adsorbed on the latex particles surface, we have confirmed qualitatively by both independent techniques that this adsorption has occurred. Since both NPs and latex colloids are negatively charged (as confirmed by electrophoresis) this adsorption process should be induced by a chemical driving force. One possibility for this driving force is the hydrophobic effect. Recent works have demonstrated that small hydrophobic objects (ions or macroions) can be adsorbed in substantial amounts onto the surface of identically charged latex colloids,[18,19] the hydrophobic effect being strong enough to overcome electrostatic repulsion. In any case, our experiments do not allow us to discriminate between this possibility and other options, so this question requires further investigation.

At this point, we would like to summarize (Fig. 8) our experimental observations together with the proposed interpretation. In our magnetophoresis experiments, the (initially) non-magnetic latex particles adsorb at their surface a certain amount of SDS-NPs, acquiring a magnetic dipole. The number of adsorbed SDS-NPs per latex particle is not very high, so they will move inside a magnetic gradient by creating a ring shaped profile, as predicted by the theory presented in Section II.

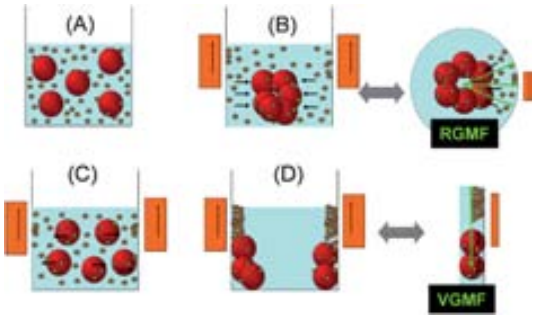

Fig. 8 Scheme of the "go and come-back" movement of the latex particles inside the magnetic separator. (A) The initial mixture. (B) Focus of the latex particles (red balls) towards the central region creating a ring-shaped structure. During this process, the SDS-NPs (brown balls) migrate to the walls where the magnetic field value is maximum (RGMF refers to Radial Gradient Magnetic Field). (C) The latex particles reverse their motion and start their migration towards the walls. (D) When both the latex particles and the SDS-NPs are trapped on the walls of the separator, the latex particles move to the bottom of the magnetic separator, where the magnetic field is smaller due to the small vertical variations in the intensity of the magnetic field (see text for details. VGMF refers to Vertical Gradient Magnetic Field).

We should also note that at the end of the process (Fig. 5), the latex particles are swept to the bottom of the vessel. This behavior can also be explained using the theory of Section II. When all the latex particles and the SDS-NPs arrive to the walls forming a layer, the particles movement is no longer driven by the radial gradient of the magnetic field. At this layer, n_f is large, as all the SDS-NPs are concentrated in the same region, so that the latex particles (even with the adsorbed particles) act again as magnetic holes. On the one hand, they are radially confined on the walls, because if they move inwards, they exit the high n_f region and act again as magnetic colloids thus returning to the wall. On the other hand, there are small vertical variations in the intensity of the magnetic field due to finite size effects, as explained in the Experimental section. This vertical gradient drives the magnetic particles upwards letting the bottom of the bottle clean. However, as the colloidal particles in a high SDS-NP concentration region act as magnetic holes, they move oppositely. This explains why the latex particles go down in the bottle walls. Once the latex particles are pushed out of the NPs rich region, the adsorbed SDS-NPs will try to go back, thus explaining why latex particles do not fall to the bottom of the bottle despite having a higher density than water. Therefore, although detailed calculations cannot be done analytically, as the vertical gradient is not uniform, the theory developed in Section II helps to explain the observed behavior.

V. Conclusions

As demonstrated in previous works,[1–10] superparamagnetic NPs can be employed to induce a tunable magnetic response in non-magnetic colloidal particles. In this work, we have extended these studies by considering the magnetophoretic behavior of commercial latex particles (the same employed in relevant applications such as latex agglutination tests) induced by superparamagnetic NPs. Our theoretical calculations show three possible magnetophoretic behaviors for colloids in a dispersion of superparamagnetic NPs. In the case of non-magnetic colloids, the colloidal particles and superparamagnetic NPs are predicted to move in opposite directions (with the colloids experiencing typical magnetophoretic velocities larger than those of the NPs). The colloids behave as magnetic holes (strongly diamagnetic particles). In the case of weakly paramagnetic colloids, we predict an interesting, two-step motion of the colloids. First, colloids move in a direction opposite to that of superparamagnetic NPs. But at some point (different for particles starting at different positions) the motion of the colloids is reversed and they move in the same direction of the superparamagnetic NPs. This behavior is due to the competition between two effects: the effective diamagnetic response also present in the case of non-magnetic colloids, and the "expected" superparamagnetic response due to the intrinsic magnetism of the colloid. This behavior of the colloids induces the formation of a ring-shaped profile of colloids, which experiences first a thinning process and later a movement towards the walls of the

magnetic separator. Finally, colloids with high intrinsic magnetic response always move in the same direction as the super-paramagnetic NPs.

Surprisingly, in our experiments with commercial latex spheres, we observed the behavior predicted for weakly magnetic particles. To explain this observation we have suggested the possibility of adsorption of NPs at the surface of the latex colloids. We have estimated that the adsorption of 500 NPs per latex colloid is enough to explain the observed magnetophoretic behavior. The actual adsorption of NPs at latex surfaces has been confirmed experimentally in our samples by three independent experimental techniques: SEM, EDS and electrophoresis.

Our findings suggest exciting possibilities for applications in non-magnetic latex colloids. For example, it could be possible to improve the latex agglutination tests performance, increasing their detection limits of infectious diseases by concentrating the latex particles with the suitable antibodies after the reaction with the antigen in the initial mixture without the need for costly centrifugation steps.

However, to make this method attractive for bioindustrial applications, a deep understanding of the mechanism of the magnetic nanoparticles adsorption on the latex surface is needed. In this way, to obtain a better fit between the model predictions and the experimental results, some of our simplifications need to be relaxed, and a refinement of the experimental setup is necessary.

Acknowledgements

We thank Dr Fabrice Sultan from Merck Estapor for providing us with the sample of latex particles employed in our experiments. M.B. thanks the FCT for financial support under the "*Compromisso com a Ciência*" program. We also acknowledge financial support from the Spanish Government grants no. FIS2009-13370-C02-02 and CONSOLIDER-NANOSELECT-CSD2007-00041. J.F. and J.C. are also partially supported by the Catalan Government grant no. 2009SGR164. J.F. acknowledges Dr Bastos-González (Univ. de Granada, Spain) for helpful comments on the chemistry of latex colloids.

References

1 B. B. Yellen, O. Hovorka and G. Friedman, *Proc. Natl. Acad. Sci. U. S. A.*, 2005, **102**(25), 8860.
2 R. M. Erb and B. Yellen, *J. Appl. Phys.*, 2008, **103**, 07A312.
3 R. M. Erb, D. S. Sebba, A. A. Lazarides and B. B. Yellen, *J. Appl. Phys.*, 2008, **103**, 063916.
4 R. M. Erb, H. S. Son, B. Samanta, V. M. Rotello and B. B. Yellen, *Nature*, 2009, **457**, 999.
5 K. H. Li and B. Yellen, *Appl. Phys. Lett.*, 2010, **97**, 083105.
6 M. D. Krebs, R. M. Erb, B. B. Yellen, B. Samanta, A. Bajaj, V. M. Rotello and E. Alsberg, *Nano Lett.*, 2009, **9**(5), 1812.
7 T. Zhu, F. Marrero and L. Mao, *Microfluid. Nanofluid.*, 2010, **9**, 1003.
8 T. Zhu, D. J. Lichlyter, M. A. Haidekker and L. Mao, *Microfluid. Nanofluid.*, 2010, **10**(6), 1233.
9 T. Zhu, R. Cheng and L. Mao, *Microfluid. Nanofluid.*, 2011, **11**, 695.
10 G. Friedman and B. Yellen, *Curr. Opin. Colloid Interface Sci.*, 2005, **10**, 158.
11 N. Pamme and A. Manz, *Anal. Chem.*, 2004, **76**, 7250.
12 G. De Las Cuevas, J. Faraudo and J. Camacho, *J. Phys. Chem. C*, 2008, **112**, 945.
13 M. Benelmekki, A. Montras, A. J. Martins, P. J. G. Coutinho and Ll. M. Martínez, *J. Magn. Magn. Mater.*, 2011, **323**, 1945.
14 M. Benelmekki, C. Caparros, A. Montras, R. Gonçalves, S. Lanceros-Mendez and Ll. M. Martínez, *J. Nanopart. Res.*, 2011, **13**, 3199.
15 J. S. Andreu, J. Camacho, J. Faraudo, M. Benelmekki, C. Rebollo and Ll. M. Martínez, *Phys. Rev. E: Stat., Nonlinear, Soft Matter Phys.*, 2011, **84**, 021402.
16 J. S. Andreu, J. Camacho and J. Faraudo, *Soft Matter*, 2011, **7**, 2336.
17 Sepmag Technologies, http://www.sepmag.eu.
18 A. Martín-Molina, C. Calero, J. Faraudo, M. Quesada-Pérez, A. Travesset and R. Hidalgo-Álvarez, *Soft Matter*, 2009, **5**, 1350.
19 C. Calero, J. Faraudo and D. Bastos-González, *J. Am. Chem. Soc.*, 2011, **133**, 15025.

Magnetophoresis of colloidal particles in a dispersion of superparamagnetic nanoparticles: Theory and Experiments

M. Benelmekki[a*], Ll. M. Martinez[b], J. S. Andreu[c,d], J. Camacho[d], J. Faraudo[c]

[a] *Centro de Física, Universidade do Minho E-4710-057 Braga, Portugal*
[b] *Sepmag Technoloies, Parc Tecnologic del Valles E-08290 Barcelona, Spain*
[c] *Institut de Ciència de Materials de Barcelona (ICMAB-CSIC), Campus UAB, E-08193 Bellaterra, Spain*
[d] *Departamentde Física, Universitat Autònoma de Barcelona. Campus UAB, E-08193 Bellaterra, Spain*

.

Supplementary Information

MATERIALS AND METHODS

Synthesis of SDS-modified nanoparticles

The ferrofluid was prepared by conventional co-precipitation of iron oxide nanoparticles from an aqueous mixture of FeSO4 and FeCl3. (1:2 molar ratio) NH4OH was used as a precipitation agent. FeSO4·7H2O (0.5 mM, 1.4 g in 50 mL) and FeCl3·6H2O (1 mM, 2.7 g in 50 mL) were mixed and heated to 80ºC. In order to precipitated the iron hydroxides, the pH value was raised and maintained to pH=3 for 30 min. The solution was rigorously stirred at a constant temperature during all the process. Then, the pH value was increased to 10. [1,2]. 1 g of the as precipitated nanoparticles was dispersed in 50 ml of a 2g/l aqueous solution of SDS (Sodium Dodecyl Sulphate) followed by vigorous stirring for 2 hours. The pH was maintained at 10 to assure a stable suspension. The prepared suspension was washed with distilled water and magnetically separated for several times to remove the excess of SDS. Finally the NPs were dried and a suspension of 10g/l aqueous solution of the SDS-modified nanoparticles was prepared.

Characterization of SDS modified nanoparticles

A LEO 906E electron microscope operating at 100 KeV, was used for transmission electron microscopy. The samples were prepared by deposition of a droplet of particles solutions on a copper grid coated with carbon and allowed to dry. The as synthesised

nanoparticles (NPs) were characterized by X-ray diffraction with a Bruker D8 Discover diffractometer using Cu Kα incident radiation. Hysteresis loop of the NPs at room temperature curves were measured with a superconducting quantum interference device (SQUID) magnetometer (Quantum Design MPMS5XL). A Nova^{TM} NanoSEM and Pegasus X4M (EDS/EBSD) were used for scanning electron microscope and elemental microanalysis, respectively.

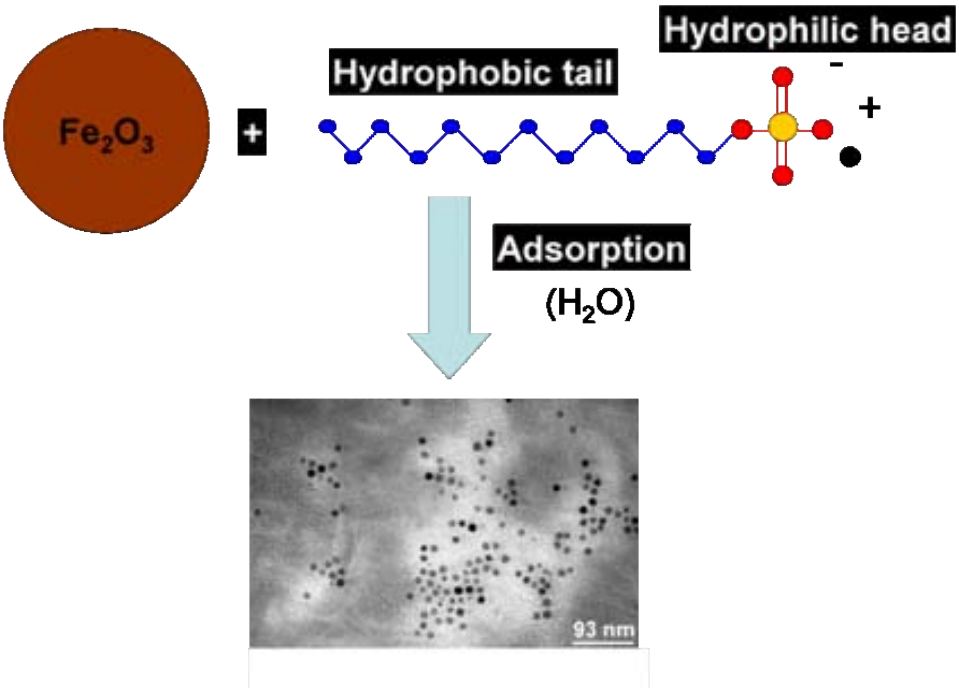

Figure S1. Scheme of the different steps of the preparation of the suspension and TEM image of SDS modified maghemite nanoparticles (SDS-NPs).

Transmission electron microscopy images of the SDS-modified nanoparticles show nanoparticles with average size of 12 nm **(Figure S1**). X- ray diffraction was performed on dry nanoparticles. Because of the modest amount of the available sample, the peaks of the diffractogram are not very well defined. They can be indexed either to maghemite or magnetite. Magnetic measurements of SDS-Modified nanoparticles show a magnetization saturation of 68 Am^2/Kg at about 0.1T (**Figure S2**).

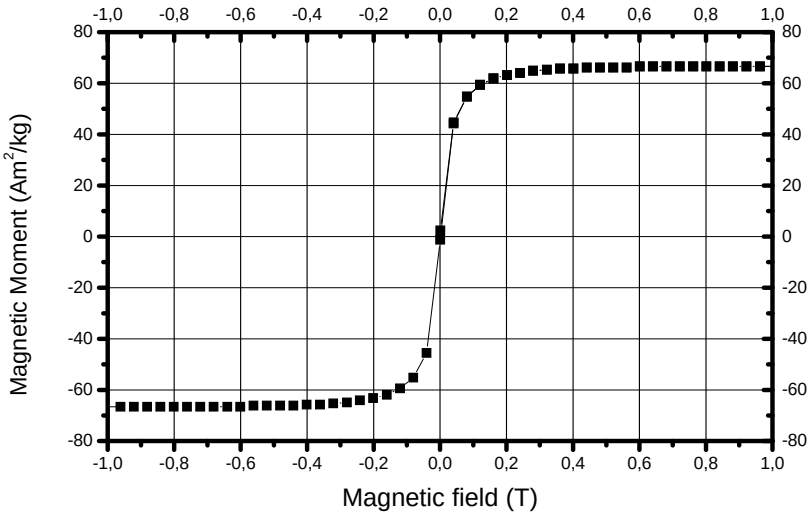

Figure S2. Magnetization curve of SDS-NPs at room temperature

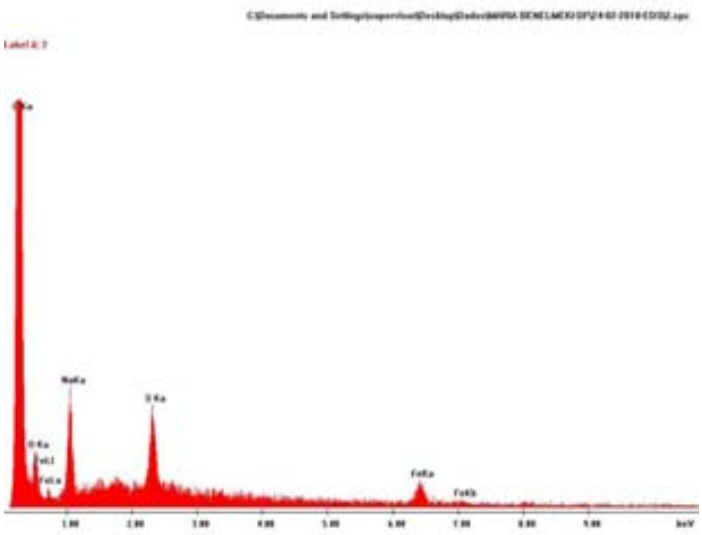

Figure S3. EDS spectrum of the mixture of latex particles and SDS-NPs

Table S1 show the composition of the sample of a 2.8% in weight of Fe (corresponding to about 3000 magnetic nanocrystal by latex particle). Other EDS measurements on

others areas of the sample (not shown) show a content of 0.33- 0.44% in weight of Fe with an acceptable integration error value (about 10), this percentage correspond to about 400-500 magnetic nanocrytal by latex particle.

Element	*Wt %*	*At %*	*Integration Error*
C K	76.5	84.1	1.0
O K	14.7	12.1	5.1
NaK	3.6	2.1	3.7
S K	2.2	0.9	3.6
FeK	2.8	0.6	5.6

Table S1. EDS microanalysis in the case of 2.8% Fe weight content. Data are expressed as both weight and atomic percents.

Magnetophoresis experiments:

The magnetophoresis setups employed in our experiment are the SEPMAG LAB 1x25 ml 2042 and 2042 Plus systems, commercially available from SEPMAG company [3]. The systems consist of a cylindrical cavity containing a high permanent magnetic field with a uniform radial gradient magnetic field pointing toward the walls of the cylindrical vessel, and a vertical gradient magnetic field close the wall and pointing to the extremities of the cylinder walls. Opacity monitoring is performed using the external light source SEPMAG CBL Q250 ml, also available in SEPMAG company [3].

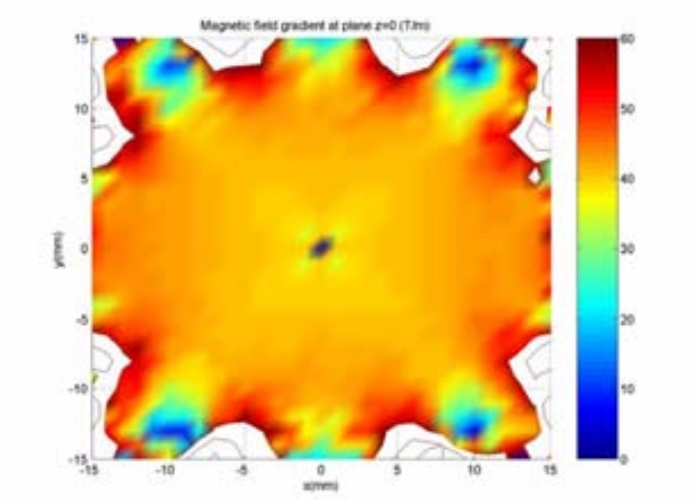

Figure S4. Distribution of the radial gradient magnetic field in the SEPMAG LAB 1x25 ml 2042 plus sytem (60T/m)

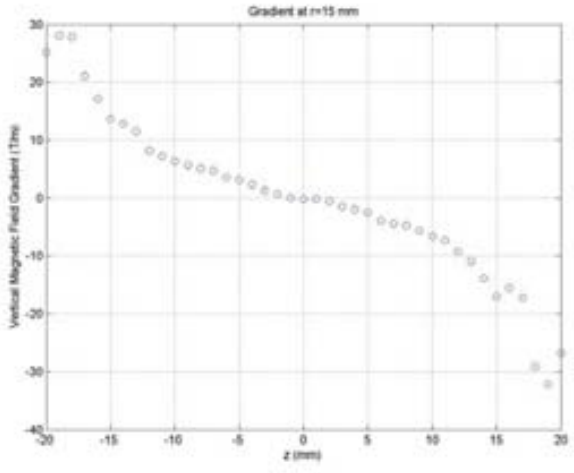

Figure S5. Distribution of the vertical gradient magnetic field in the cylindrical walls of the SEPMAG LAB 1x25 ml 2042 plus (60T/m).

Magnetophoresis behavior of the SDS-NPs:

The magnetoforesis experiment was performed by placing a glass bottle containing 15 ml of the synthesised ferrofluid (10g/l) inside the SEPMAG cylindrical cavity. The initial yellow-brown solution becomes transparent reaching a transparent final state with all particles close to the walls of the bottle. By applying 60T/m gradient the total time separation is about 20 hours. By applying 30T/m gradient the total time separation is about 55 hours (Figure S6).

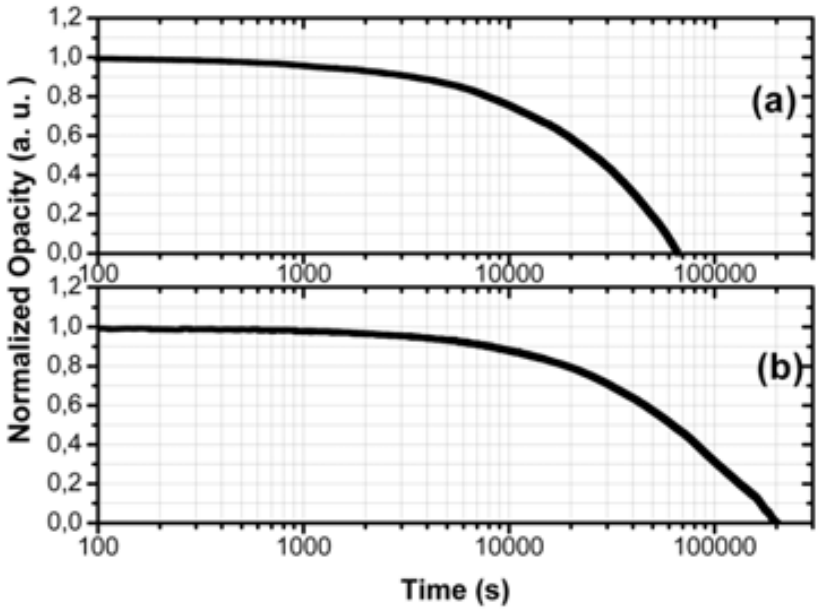

Figure S6. Magnetophoresis curves of the synthesised SDS-NPs core-shell at different magnetic field gradients: (a) 60 T/m and (b) 30T/m

References

1. M. Benelmekki, C. Caparros, A. Montras, R. Goncalves, S. Lanceros-Mendez, Ll.M. Martinez J. Nanopart. Res. Doi10.1007/s11051-010-0218-6. (2010).
2. Zhang, Jing; Yu, Demei; Chen, Wei; Xie, Yunchuan; Wan, Weitao; Liang, Honglu; Min, Chao *Journal of Magnetism and Magnetic Materials* **2009,** *321*, 572-77

4. Sepmag tecnologies www.sepmag.eu

Bibliography

[1] C. P. Bean and J. D. Livingston. Superparamagnetism. *Journal of Applied Physics*, 30(4):S120–S129, 1959.

[2] A. Lu, E. L. Salabas, and F. Schüth. Magnetic nanoparticles: Synthesis, protection, functionalization, and application. *Angewandte Chemie International Edition*, 46(8):1222–1244, 2007.

[3] K. M. Krishnan. Biomedical nanomagnetics: A *Spin* through possibilities in imaging, diagnostics, and therapy. *Magnetics, IEEE Transactions on*, 46(7):2523–2558, 2010.

[4] E. Taboada, E. Rodríguez, A. Roig, J. Oró, A. Roch, and R. N. Muller. Relaxometric and magnetic characterization of ultrasmall iron oxide nanoparticles with high magnetization. Evaluation as potential T_1 magnetic resonance imaging contrast agents for molecular imaging. *Langmuir*, 23(8):4583–4588, 2007.

[5] C. Baumgartner, L. Deecke, G. Stroink, and S. J. Williamson. *Biomagnetism: Fundamental Research and Clinical Applications*. IOS Press, Amsterdam, 1st edition, 1995.

[6] D. Eberbeck, C. Bergemann, S. Hartwig, U. Steinhoff, and L. Trahms. Binding kinetics of magnetic nanoparticles on latex beads and yeast cells studied by magnetorelaxometry. *Journal of Magnetism and Magnetic Materials*, 289:435–438, 2005.

[7] J. S. Andreu, J. Camacho, J. Faraudo, M. Benelmekki, C. Rebollo, and Ll. M. Martínez. Simple analytical model for the magnetophoretic separation of superparamagnetic dispersions in a uniform magnetic gradient. *Physical Review E*, 84(2):021402–8, 2011.

[8] D. X. Chen, A. Sánchez, E. Taboada, A. Roig, N. Sun, and H. C. Gu. Size determination of superparamagnetic nanoparticles from magnetization curve. *Journal of Applied Physics*, 105(8):083924–6, 2009.

[9] R. Chantrell, J. Popplewell, and S. Charles. Measurements of particle size distribution parameters in ferrofluids. *Magnetics, IEEE Transactions on*, 14(5):975–977, 1978.

[10] R. E. Rosensweig. Magnetic fluids. *Scienti c American*, 10(4):136–145, 1982.

[11] R. Kaiser and G. Miskolczy. Magnetic properties of stable dispersions of subdomain magnetite particles. *Journal of Applied Physics*, 41(3):1064–1072, 1970.

[12] D. Leun and A. K. Sengupta. Preparation and characterization of magnetically active polymeric particles (MAPPs) for complex environmental separations. *Environmental Science & Technology*, 34(15):3276–3282, 2000.

[13] T. K. Jain, J. Richey, M. Strand, D. L. Leslie-Pelecky, C. A. Flask, and V. Labhasetwar. Magnetic nanoparticles with dual functional properties: Drug delivery and magnetic resonance imaging. *Biomaterials*, 29(29):4012–4021, 2008.

[14] S. Behrens. Preparation of functional magnetic nanocomposites and hybrid materials: recent progress and future directions. *Nanoscale*, 3(3):877–892, 2011.

[15] B. M. Berkovsky, V. F. Medvedev, and M. S. Krakov. *Magnetic Fluids, Engineering Applications*. Oxford University, USA, 1993.

[16] Magnetic Carriers, http://www.magneticmicrosphere.com (2012).

[17] P. Tartaj, M. del Puerto Morales, S. Veintemillas-Verdaguer, T. González-Carreño, and C. J. Serna. The preparation of magnetic nanoparticles for applications in biomedicine. *Journal of Physics D: Applied Physics*, 36(13):R182–R197, 2003.

[18] K. Kluchova, R. Zboril, J. Tucek, M. Pecova, L. Zajoncova, I. Safarik, M. Mashlan, I. Markova, D. Jancik, M. Sebela, H. Bartonkova, V. Bellesi, P. Novak, and D. Petridis. Superparamagnetic maghemite nanoparticles from solid-state synthesis. Their functionalization towards peroral MRI contrast agent and magnetic carrier for trypsin immobilization. *Biomaterials*, 30(15):2855–2863, 2009.

[19] X. Xu, G. Friedman, K. D. Humfeld, S. A. Majetich, and S. A. Asher. Synthesis and utilization of monodisperse superparamagnetic colloidal particles for magnetically controllable photonic crystals. *Chemistry of Materials*, 14(3):1249–1256, 2002.

[20] E. Taboada, R. Solanas, E. Rodríguez, R. Weissleder, and A. Roig. Supercritical-fluid-assisted one-pot synthesis of biocompatible Core(γ-Fe_2O_3)/Shell(SiO_2) nanoparticles as high relaxivity T_2-contrast agents for magnetic resonance imaging. *Advanced Functional Materials*, 19(14):2319–2324, 2009.

[21] M. Benelmekki, C. Caparrós, A. Montràs, R. Gonçalves, S. Lanceros-Méndez, and Ll. M. Martínez. Horizontal low gradient magnetophoresis behaviour of iron oxide nanoclusters at the different steps of the synthesis route. *Journal of Nanoparticle Research*, 13(8):3199–3206, 2011.

[22] X. Liu, Y. Guan, Z. Ma, and H. Liu. Surface modification and characterization of magnetic polymer nanospheres prepared by miniemulsion polymerization. *Langmuir*, 20(23):10278–10282, 2004.

[23] N. Arsalani, H. Fattahi, and M. Nazapoor. Synthesis and characterization of PVP-functionalized superparamagnetic Fe_3O_4 nanoparticles as an MRI constrast agent. *eXPRESS Polymer Letters*, 4(6):329–338, 2010.

[24] H. Wang, Y. B. Sun, Q. W. Chen, Y. F. Yu, and K. Cheng. Synthesis of carbon-encapsulated superparamagnetic colloidal nanoparticles with magnetic-responsive photonic crystal property. *Dalton Transactions*, 39(40):9565–9569, 2010.

[25] J. Lim, C. Lanni, E. R. Evarts, F. Lanni, R. D. Tilton, and S. A. Majetich. Magnetophoresis of nanoparticles. *ACS Nano*, 5(1):217–226, 2010.

[26] M. Benelmekki, A. Montràs, A. J. Martins, P. J. G. Coutinho, and Ll. M. Martínez. Magnetophoresis behaviour at low gradient magnetic field and size control of nickel single core nanobeads. *Journal of Magnetism and Magnetic Materials*, 323(15):1945–1949, 2011.

[27] N. Paunovi , Z.V. Popovi , and Z.D. Doh evi -Mitrovi . Superparamagnetism in iron-doped CeO_{2-y} nanocrystals. *Journal of Physics: Condensed Matter*, 24(45):456001–6, 2012.

[28] D. Y. Chung, T. R. Hickman, R. P. De Paula, and J. H. Cole. Magneto-optics of ferrofluids, using fiber optics. *Journal of Magnetism and Magnetic Materials*, 39(1–2):71–74, 1983.

[29] S. Z. Malynych, A. Tokarev, S. Hudson, G. Chumanov, J. Ballato, and K. G. Kornev. Magneto-controlled illumination with opto-fluidics. *Journal of Magnetism and Magnetic Materials*, 322(14):1894–1897, 2010.

[30] Y. Zhao, Y. Zhang, R. Lv, and Q. Wang. Novel optical devices based on the tunable refractive index of magnetic fluid and their characteristics. *Journal of Magnetism and Magnetic Materials*, 323(23):2987–2996, 2011.

[31] J. Ge, Y. Hu, and Y. Yin. Highly tunable superparamagnetic colloidal photonic crystals. *Angewandte Chemie International Edition*, 46(39):7428–7431, 2007.

[32] J. Ge, L. He, J. Goebl, and Y. Yin. Assembly of magnetically tunable photonic crystals in nonpolar solvents. *Journal of the American Chemical Society*, 131(10):3484–3486, 2009.

[33] Q. A. Pankhurst, J. Connolly, S. K. Jones, and J. Dobson. Applications of magnetic nanoparticles in biomedicine. *Journal of Physics D: Applied Physics*, 36(13):R167–R181, 2003.

[34] J. L. Corchero and A. Villaverde. Biomedical applications of distally controlled magnetic nanoparticles. *Trends in Biotechnology*, 27(8):468–476, 2009.

[35] C. C. Berry and A. S. G. Curtis. Functionalisation of magnetic nanoparticles for applications in biomedicine. *Journal of Physics D: Applied Physics*, 36(13):R198–R206, 2003.

[36] V. Salgueiriño-Maceira, M. A. Correa-Duarte, M. Spasova, L. M. Liz-Marzán, and M. Farle. Composite silica spheres with magnetic and luminescent functionalities. *Advanced Functional Materials*, 16(4):509–514, 2006.

[37] C. T. Yavuz, J. T. Mayo, W. W. Yu, A. Prakash, J. C. Falkner, S. Yean, L. Cong, H. J. Shipley, A. Kan, M. Tomson, D. Natelson, and V. L. Colvin. Low-field magnetic separation of monodisperse Fe_3O_4 nanocrystals. *Science*, 314(5801):964–967, 2006.

[38] J. K. Lim, D. C. J. Chieh, S. A. Jalak, P. Y. Toh, N. H. M. Yasin, B. W. Ng, and A. L. Ahmad. Rapid magnetophoretic separation of microalgae. *Small*, 8(11):1683–1692, 2012.

[39] C. T. Yavuz, A. Prakash, J. T. Mayo, and V. L. Colvin. Magnetic separations: From steel plants to biotechnology. *Chemical Engineering Science*, 64(10):2510–2521, 2009.

[40] G. Friedman and B. Yellen. Magnetic separation, manipulation and assembly of solid phase in fluids. *Current Opinion in Colloid & Interface Science*, 10(3-4):158–166, 2005.

[41] I. Safarik and M. Safarikova. Magnetic techniques for the isolation and purification of proteins and peptides. *BioMagnetic Research and Technology*, 2(1):7–23, 2004.

[42] J. R. Stephens, J. S. Beveridge, and M. E. Williams. Analytical methods for separating and isolating magnetic nanoparticles. *Physical Chemistry Chemical Physics*, 14(10):3280–3289, 2012.

[43] D. X. Chen, E. Taboada, and A. Roig. Experimental study on T_2 relaxation time of protons in water suspensions of iron-oxide nanoparticles: Cases of composite nanospheres. *Journal of Magnetism and Magnetic Materials*, 323(20):2487–2492, 2011.

[44] D. X. Chen, G. Via, F. J. Xu, C. Navau, A. Sanchez, H. C. Gu, J. S. Andreu, C. Calero, J. Camacho, and J. Faraudo. Waiting time dependence of T_2 of protons in water suspensions of iron-oxide nanoparticles: Measurements and simulations. *Journal of Applied Physics*, 110(7):073917–9, 2011.

[45] M. R. J. Carroll, P. P. Huffstetler, W. C. Miles, J. D. Goff, R. M. Davis, J. S. Ri e, M. J. House, R. C. Woodward, and T. G. St Pierre. The effect of polymer coatings on proton transverse relaxivities of aqueous suspensions of magnetic nanoparticles. *Nanotechnology*, 22(32):325702–7, 2011.

[46] D. H. Everett. *Basic Principles of Colloid Science*. Number 978-0-85186-443-3 in RSC Paperbacks. The Royal Society of Chemistry, London, 1st edition, 1988.

[47] P. G. De Gennes and P. A. Pincus. Pair correlations in s ferromagnetic colloid. *Phys. Kondens. Materie*, 11(3):189–198, 1970.

[48] P. C. Jordan. Association phenomena in a ferromagnetic colloid. *Molecular Physics*, 25(4):961–973, 1973.

[49] R. E. Rosensweig. *Ferrohydrodynamics*. Cambridge University Press, New York, 1st edition, 1985.

[50] J. H. E. Promislow, A. P. Gast, and M. Fermigier. Aggregation kinetics of paramagnetic colloidal particles. *The Journal of Chemical Physics*, 102(13):5492–5498, 1995.

[51] J. Faraudo and J. Camacho. Cooperative magnetophoresis of superparamagnetic colloids: theoretical aspects. *Colloid & Polymer Science*, 288(2):207–215, 2010.

[52] G. De Las Cuevas, J. Faraudo, and J. Camacho. Low-gradient magnetophoresis through field-induced reversible aggregation. *The Journal of Physical Chemistry C*, 112(4):945–950, 2008.

[53] F. Martínez-Pedrero, M. Tirado-Miranda, A. Schmitt, and J. Callejas-Fernández. Formation of magnetic filaments: A kinetic study. *Physical Review E*, 76(1):011405–9, 2007.

[54] G. P. Gajula, M. T. Neves-Petersen, and S. B. Petersen. Visualization and quantification of four steps in magnetic field induced two-dimensional ordering of superparamagnetic submicron particles. *Applied Physics Letters*, 97(10):103103–3, 2010.

[55] D. Heinrich, A. R. Goñi, and C. Thomsen. Dynamics of magnetic-field-induced clustering in ionic ferrofluids from raman scattering. *The Journal of Chemical Physics*, 126(12):124701–7, 2007.

[56] V. Schaller, U. Kraling, C. Rusu, K. Petersson, J. Wipenmyr, A. Krozer, G. Wahnstrom, A. Sanz-Velasco, P. Enoksson, and C. Johansson. Motion of nanometer sized magnetic particles in a magnetic field gradient. *Journal of Applied Physics*, 104(9):093918–14, 2008.

[57] F. Martínez-Pedrero, M. Tirado-Miranda, A. Schmitt, and J. Callejas-Fernández. Aggregation of magnetic polystyrene particles: A light scattering study. *Colloids and Surfaces A: Physicochemical and Engineering Aspects*, 270-271:317–322, 2005.

[58] F. Martínez-Pedrero, M. Tirado-Miranda, A. Schmitt, and J. Callejas-Fernández. Controlling the magnetic filaments length by tuning the particle interactions. *Journal of Colloid and Interface Science*, 318(1):23–28, 2008.

[59] F. Martínez-Pedrero, A. El-Harrak, J. C. Fernández-Toledano, M. Tirado-Miranda, J. Baudry, A. Schmitt, J. Bibette, and J. Callejas-Fernández. Kinetic study of coupled field-induced aggregation and sedimentation processes arising in magnetic fluids. *Physical Review E*, 78(1):011403–9, 2008.

[60] F. Martínez-Pedrero, M. Tirado-Miranda, A. Schmitt, and J. Callejas-Fernández. Primary and secondary bonds in field induced aggregation of electric double layered magnetic particles. *Langmuir*, 25(12):6658–6664, 2009.

[61] J. B. Hayter and R. Pynn. Structure factor of a magnetically saturated ferrofluid. *Physical Review Letters*, 49(15):1103–1106, 1982.

[62] M. Fermigier and A. P. Gast. Structure evolution in a paramagnetic latex suspension. *Journal of Colloid and Interface Science*, 154(2):522–539, 1992.

[63] J. H. E. Promislow and A. P. Gast. Low-energy suspension structure of a magnetorheological fluid. *Physical Review E*, 56(1):642–651, 1997.

[64] R. M. Erb, H. S. Son, B. Samanta, V. M. Rotello, and B. B. Yellen. Magnetic assembly of colloidal superstructures with multipole symmetry. *Nature*, 457(7232):999–1002, 2009.

[65] A. T. Skjeltorp. One- and two-dimensional crystallization of magnetic holes. *Physical Review Letters*, 51(25):2306–2309, 1983.

[66] K. H. Li and B. B. Yellen. Magnetically tunable self-assembly of colloidal rings. *Applied Physics Letters*, 97(8):083105–3, 2010.

[67] L. Gonzalez, S. Fateen, K. Smith, and T. A. Hatton. Magnetophoresis of non-magnetic, submicrometer particles in magnetic fluids. *Molecular Engineering of Biological and Chemical Systems (DSpace@MIT)*, http://hdl.handle.net/1721.1/3931:7, 2004.

[68] R. M. Erb and B. B. Yellen. Concentration gradients in mixed magnetic and nonmagnetic colloidal suspensions. *J. Appl. Phys.*, 103(7):07A312–3, 2008.

[69] R. M. Erb, D. S. Sebba, A. A. Lazarides, and B. B. Yellen. Magnetic field induced concentration gradients in magnetic nanoparticle suspensions: Theory and experiment. *Journal of Applied Physics*, 103(6):063916–5, 2008.

[70] M. D. Krebs, R. M. Erb, B. B. Yellen, B. Samanta, A. Bajaj, V. M. Rotello, and E. Alsberg. Formation of ordered cellular structures in suspension via label-free negative magnetophoresis. *Nano Letters*, 9(5):1812–1817, 2009.

[71] P. Domínguez-García, S. Melle, J. M. Pastor, and M. A. Rubio. Scaling in the aggregation dynamics of a magnetorheological fluid. *Physical Review E*, 76(5):051403–13, 2007.

[72] C. Rablau, P. Vaishnava, C. Sudakar, R. Tackett, G. Lawes, and R. Naik. Magnetic-field-induced optical anisotropy in ferrofluids: A time-dependent light-scattering investigation. *Physical Review E*, 78(5):051502–9, 2008.

[73] D. Heinrich, A. R. Goñi, A. Smessaert, S. H. L. Klapp, L. M. C. Cerioni, T. M. Osán, D. J. Pusiol, and C. Thomsen. Dynamics of the field-induced formation of hexagonal zipped-chain superstructures in magnetic colloids. *Physical Review Letters*, 106(20):208301–4, 2011.

[74] O. Pascu, J. M. Caicedo, J. Fontcuberta, G. Herranz, and A. Roig. Magneto-optical characterization of colloidal dispersions. application to nickel nanoparticles. *Langmuir*, 26(15):12548–12552, 2010.

[75] M. Takayasu, R. Gerber, and F. Friedlaender. Magnetic separation of submicron particles. *Magnetics, IEEE Transactions on*, 19(5):2112–2114, 1983.

[76] A. Senyei, K. Widder, and G. Czerlinski. Magnetic guidance of drug-carrying microspheres. *Journal of Applied Physics*, 49(6):3578–3583, 1978.

[77] B. B. Yellen, O. Hovorka, and G. Friedman. Arranging matter by magnetic nanoparticle assemblers. *Proceedings of the National Academy of Sciences of the United States of America*, 102(25):8860–8864, 2005.

[78] G. D. Moeser, K. A. Roach, W. H. Green, T. Alan Hatton, and P. E. Laibinis. High-gradient magnetic separation of coated magnetic nanoparticles. *AIChE Journal*, 50(11):2835–2848, 2004.

[79] L. Langguth. Elektromagnetische aufbereitung. von F. Langguth. Aus dem Handbuch der Elektrochemie verlag von wilhelm knapp halle. *Zeitschrift für Elektrochemie*, 9(12):248–250, 1903.

[80] D. Korda. *La séparation électromagnétique et électrostatique des minerais*. L'Éclairage Électrique, 1905.

[81] C. G. Gunther. *Electro-magnetic ore separation*. Hill publishing company, New York, 1st edition, 1909.

[82] H. Holm, E. Maxwell, J. Oberteuffer, D. Kelland, C. De Latour, and P. Martson. High intensity magnetic filtration. In *Magnetism and magnetic materials*, volume 5, pages 949–949. AIP, 1971.

[83] J. Oberteuffer. High gradient magnetic separation. *Magnetics, IEEE Transactions on*, 9(3):303–306, 1973.

[84] D. Kelland. High gradient magnetic separation applied to mineral beneficiation. *Magnetics, IEEE Transactions on*, 9(3):307–310, 1973.

[85] S. Trindade and H. Kolm. Magnetic desulfurization of coal. *Magnetics, IEEE Transactions on*, 9(3):310–313, 1973.

[86] C. De Latour. Magnetic separation in water pollution control. *Magnetics, IEEE Transactions on*, 9(3):314–316, 1973.

[87] C. De Latour and H. Kolm. Magnetic separation in water pollution control II. *Magnetics, IEEE Transactions on*, 11(5):1570–1572, 1975.

[88] J. Watson and D. Hocking. The beneficiation of clay using a superconducting magnetic separator. *Magnetics, IEEE Transactions on*, 11(5):1588–1590, 1975.

[89] D. Melville, F. Paul, and S. Roath. High gradient magnetic separation of red cells from whole blood. *Magnetics, IEEE Transactions on*, 11(6):1701–1704, 1975.

[90] SEPMAG technologies, http://www.sepmag.eu (2012).

[91] http://www.youtube.com/watch?v=BVipEdKoMh8 (2012).

[92] M. A. M. Gijs. Magnetic bead handling on-chip: new opportunities for analytical applications. *Micro uidics and Nano uidics*, 1(1):22–40, 2004.

[93] N. Pamme. Magnetism and microfluidics. *Lab on a Chip*, 6(1):24–38, 2006.

[94] N. Pamme, J. C. T. Eijkel, and A. Manz. On-chip free-flow magnetophoresis: Separation and detection of mixtures of magnetic particles in continuous flow. *Journal of Magnetism and Magnetic Materials*, 307(2):237–244, 2006.

[95] N. Pamme and A. Manz. On-chip free-flow magnetophoresis: Continuous flow separation of magnetic particles and agglomerates. *Analytical Chemistry*, 76(24):7250–7256, 2004.

[96] L. Gao, M. A. Tahir, L. N. Virgin, and B. B. Yellen. Multiplexing superparamagnetic beads driven by multi-frequency ratchets. *Lab on a Chip*, 11(24):4214–4220, 2011.

[97] J. T. Mayo, S. S. Lee, C. T. Yavuz, W. W. Yu, A. Prakash, J. C. Falkner, and V. L. Colvin. A multiplexed separation of iron oxide nanocrystals using variable magnetic fields. *Nanoscale*, 3(11):4560–4563, 2011.

[98] J. S. Beveridge, J. R. Stephens, A. H. Latham, and M. E. Williams. Differential magnetic catch and release: Analysis and separation of magnetic nanoparticles. *Analytical Chemistry*, 81(23):9618–9624, 2009.

[99] T. Zhu, F. Marrero, and L. Mao. Continuous separation of non-magnetic particles inside ferrofluids. *Micro uidics and Nano uidics*, 9(4):1003–1009, 2010.

[100] T. Zhu, D. Lichlyter, M. Haidekker, and L. Mao. Analytical model of microfluidic transport of non-magnetic particles in ferrofluids under the influence of a permanent magnet. *Micro uidics and Nano uidics*, 10(6):1233–1245, 2011.

[101] T. Zhu, R. Cheng, and L. Mao. Focusing microparticles in a microfluidic channel with ferrofluids. *Micro uidics and Nano uidics*, 11(6):695–701, 2011.

[102] T. Zhu, R. Cheng, S. Lee, E. Rajaraman, M. Eiteman, T. Querec, E. Unger, and L. Mao. Continuous-flow ferrohydrodynamic sorting of particles and cells in microfluidic devices. *Micro uidics and Nano uidics*, 13(4):645–654, 2012.

[103] H. J. C. Berendsen, D. van der Spoel, and R. van Drunen. Gromacs: A message-passing parallel molecular dynamics implementation. *Computer Physics Communications*, 91(1–3):43–56, 1995.

[104] S. Plimpton. Fast parallel algorithms for short-range molecular dynamics. *Journal of Computational Physics*, 117(1):1–19, 1995.

[105] N. G. van Kampen. *Stochastic Processes in Physics and Chemistry*. North-Holland, Amsterdam, 3rd edition, 1981.

[106] D. Ermak and J. McCammon. Brownian dynamics with hydrodynamic interactions. *J. Chem. Phys.*, 69(4):1352–1360, 1978.

[107] E. Kim, K. Stratford, P. J. Camp, and M. E. Cates. Hydrodynamic interactions in colloidal ferrofluids: A lattice boltzmann study. *The Journal of Physical Chemistry B*, 113(12):3681–3693, 2008.

[108] J. J. Monaghan. Particle methods for hydrodynamics. *Computer Physics Reports*, 3(2):71–124, 1985.

[109] D. Eberbeck, F. Wiekhorst, U. Steinhoff, and L. Trahms. Aggregation behaviour of magnetic nanoparticle suspensions investigated by magnetorelaxometry. *Journal of Physics: Condensed Matter*, 18(38):S2829–S2846, 2006.

[110] J. M. Caicedo, E. Taboada, D. Hrabovský, M. López-García, G. Herranz, A. Roig, A. Blanco, C. López, and J. Fontcuberta. Facile route to magnetophotonic crystals by infiltration of 3d inverse opals with magnetic nanoparticles. *Journal of Magnetism and Magnetic Materials*, 322(9–12):1494–1496, 2010.

[111] J. N. Israelachvili. *Intermolecular and surface forces*. Academic Press, Amsterdam, 3rd edition, 2011.

[112] A. O. Ivanov, Z. Wang, and C. Holm. Applying the chain formation model to magnetic properties of aggregated ferrofluids. *Physical Review E*, 69(3):031206–6, 2004.

[113] M. Barrett, A. Deschner, J. P. Embs, and M. C. Rheinstadter. Chain formation in a magnetic fluid under the influence of strong external magnetic fields studied by small angle neutron scattering. *Soft Matter*, 7(14):6678–6683, 2011.

[114] S. Miyazima, P. Meakin, and F. Family. Aggregation of oriented anisotropic particles. *Physical Review A*, 36(3):1421–1427, 1987.

[115] M. Carmen-Miguel and R. Pastor-Satorras. Kinetic growth of field-oriented chains in dipolar colloidal solutions. *Physical Review E*, 59(1):826–834, 1999.

[116] J. Happel and H. Brenner. *Low Reynolds number hydrodynamics*. Martinus Nijhoff Publishers, The Hague, 1st edition, 1983.

[117] J. S. Andreu, J. Camacho, and J. Faraudo. Aggregation of superparamagnetic colloids in magnetic fields: the quest for the equilibrium state. *Soft Matter*, 7(6):2336–2339, 2011.

[118] M. Tirado and J. de la Torre. Translational friction coefficients of rigid, symmetric top macromolecules. application to circular cylinders. *J. Chem. Phys.*, 71(6):2581–2587, 1979.

[119] MagChain Simulation software, http://www.icmab.es/softmattertheory (2012).

[120] http://www.youtube.com/watch?v=LJf2MYTedEU (2012).

[121] Karl Mandel and Frank Hutter. The magnetic nanoparticle separation problem. *Nano Today*, 7(6):485–487, 12 2012.

[122] M. Popovici, M. Gich, D. Ni anský, A. Roig, C. Savii, Ll. Casas, E. Molins, K. Zaveta, C. Enache, J. Sort, S. De Brion, G. Chouteau, and J. Nogués. Optimized synthesis of the elusive -Fe_2O_3 phase via sol-gel chemistry. *Chemistry of Materials*, 16(25):5542–5548, 2004.